Muon counter simulation studies for the AMIGA enhancement of the Pierre Auger Observatory

Masterarbeit
zur Erlangung des akademischen Grades
Master of Science (M.Sc.)

dem Department Physik der
Naturwissenschaftlich-Technischen Fakultät
der Universität Siegen

vorgelegt von
B.Sc. Marcus Niechciol

April 2011

Contents

1. Introduction

Astroparticle physics is a relatively young branch of physics, situated at the intersection of particle physics, astronomy and cosmology. In this field, methods and techniques from particle physics are used to study particles of astronomical origin in order to establish a new approach to fundamental cosmological problems, such as the structure of the universe or the nature of dark matter.

The beginnings of astroparticle physics date back to the onset of the 20th century, when Victor Franz Hess (1883 - 1964) performed a series of balloon flights to examine an effect that had been observed since the late 18th century: a simple electroscope loses its charge even when well insulated. This had later been generally ascribed to ionizing radiation from naturally occuring radioactive elements in the ground. But during his balloon flights, Hess discovered that even though the ionizing radiation does indeed diminish at first, as it is expected from ground radiation, it increases again when higher altitudes are reached. This led to the assumption of an extraterrestic, cosmic origin of this ionizing radiation, which could be confirmed by later experiments.

After Hess, many physicists began working on this new kind of radiation. Among them was Pierre Auger (1899 - 1993), who, during his studies atop the Alps, observed time-coincident signals in spatially separated particle detectors. Auger postulated a common origin of these coincidentally detected particles: primary cosmic rays interact with nuclei of the earth's atmosphere and produce cascades of secondary particles, now commonly referred to as extensive air showers.

(a) (b)

Figure 1.1: (a) Victor Franz Hess (1883 - 1964) in one of his balloons; (b) Pierre Auger (1899 - 1993); [1].

Since the measurement of these air showers is the only feasible way to determine the properties of high-energy primary cosmic rays, a number of different experiments have been carried out since. The focus of this thesis lies on the Pierre Auger Observatory, an international cosmic ray observatory specifically designed to study ultra-high-energy cosmic rays combining two different detection techniques, using an array of water Cherenkov based surface detectors and fluorescence telescopes. The southern site of the observatory, situated near Malargüe, Argentina, is taking data since 2004. Already, some modifications and enhancements to the existing detector systems are underway. In this thesis, the AMIGA (Auger Muons and Infill for the Ground Array) enhancement will be discussed primarily. The purpose of AMIGA is twofold: On the one hand, an infill array of additional surface detectors will lower the energy threshold of the experiment. On the other hand, buried muon counters will allow for the measurement of the number of muons inside an air shower and thus give the opportunity to study the composition of primary cosmic rays. Since 2009, two prototype muon counters have been deployed. To support the analysis of the data these prototypes are taking, simulation studies have been performed. In the thesis at hand, the results of these simulations will be presented and compared to the prototype data.

2. Cosmic rays

Each second, the earth is hit by billions of particles of cosmic origin, from light neutrinos produced in the centre of our sun to heavy iron nuclei originating from active galactic nuclei (AGN) many light-years away. For historical reasons, the term "cosmic rays" only refers to a fraction of these particles, namely charged particles like nuclei or electrons. In the following chapter, two important properties of cosmic rays will be discussed: their composition and their energy spectrum. In addition, extensive air showers that occur when primary cosmic particles hit the top of the atmosphere and produce cascades of secondary particles, will be covered. Since the Pierre Auger Observatory is specifically designed to study ultra-high-energy cosmic rays (UHECR) in the EeV range, special emphasis will be placed on this energy range.

2.1. Composition

Determining the composition of primary cosmic rays is no easy task. Up to an energy of about 100 TeV direct measurements using balloon-borne or satellite experiments are possible, but for higher energies, indirect measurements of extensive air showers are the only feasible option due to the rapidly decreasing flux (see Section 2.2). To ascertain the type of primary particle, its properties have to be reconstructed from the recorded shower data. However, this reconstruction is highly dependent on the interaction model used and the available models become less precise at high energies. Nevertheless, composition studies can help revealing the origin of cosmic rays and their acceleration mechanisms.

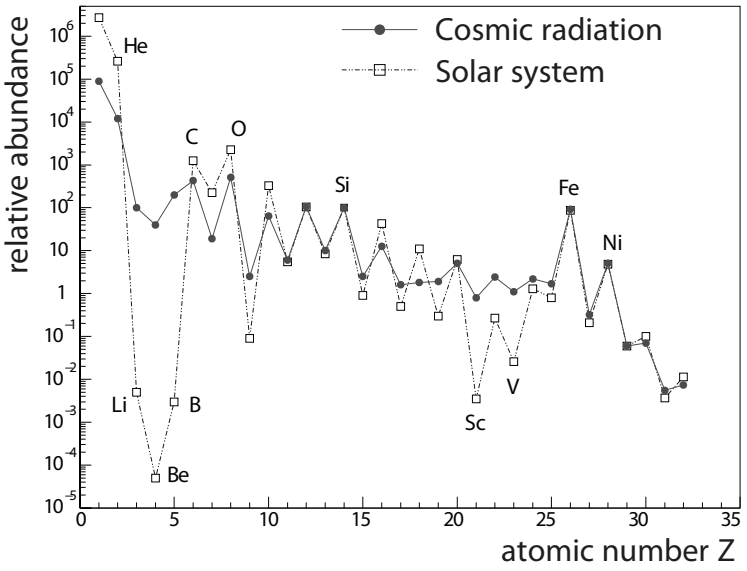

Figure 2.1: Elemental composition of primary cosmic rays compared to the elemental abundance in the solar system [2, 3]; all values have been normalized so that the elemental abundance of Si is 10^2.

The major part of primary cosmic rays are protons and nuclei with about 98 %, whilst about 2 % are electrons [4]. Of the protons and nuclei, about 87 % are protons, 12 % are helium nuclei and the remaining 1 % are heavier nuclei. In Fig. 2.1, the elemental composition of cosmic rays is shown compared to the elemental abundance in the solar system. In general, the abundances in cosmic rays and in the solar system are in good agreement. This leads to the assumption that the sources of cosmic radiation are stellar objects like the sun, which produce the particles via nucleosythesis. However, there are a few major differences. Firstly, hydrogen and helium are less abundant in cosmic rays than in the solar system. The ionization energies of these two elements are relatively high, therefore it is likely that a fraction of the hydrogen and helium atoms produced in the sources is not ionized. However, the predominant acceleration mechanisms work only for charged particles, so that this fraction of the hydrogen and helium atoms is not undergoing any acceleration and therefore doesn't show up in cosmic rays. Secondly, two groups of heavier elements (Li, Be, B and Sc, Ti, V) are much more abundant in cosmic rays than in the solar system. These elements can be considered spallation products of the collision of heavier elements from the CNO (carbon, nitrogen, oxygen) group (for Li, Be, B) or the iron group (for Sc, Ti, V) with interstellar matter, which are then accelerated further and thus increase the abundance of these elements in cosmic rays [5].

2.2. Energy spectrum

The energy range of the cosmic ray particles impinging on the earth covers about eleven orders of magnitude, whereas the flux decreases by about three orders of magnitude per energy decade, thus even spanning thirty orders of magnitude in total, as shown in Fig. 2.2. The differential flux of primary cosmic particles can be approximated by a broken power law:

$$\frac{\mathrm{d}\phi}{\mathrm{d}E} \propto E^{-\gamma}. \tag{2.1}$$

The spectral index γ is piecewise approximately constant [6]. The regions where the spectral index changes are called the knee and the ankle. The knee is situated at an energy of about 4×10^{15} eV. Until then, the spectral index has a value of 2.7 which changes to 3.1 at the knee, thus steepening the spectrum. The origin of the knee is still an important topic of research. Recent results of air shower experiments suggest that the knee is caused by a reduced abundance of light nuclei in cosmic rays [7], but there are other theories which imply that the knee is erroneously induced during the detection process as result of a yet unknown interaction in the shower development [8].

The existence of a second knee at about 4×10^{17} eV is suggested by some measurements [9]. However, since there are contradictory measurements where this feature is not observed [10], the existence of the second knee is rather controversial.

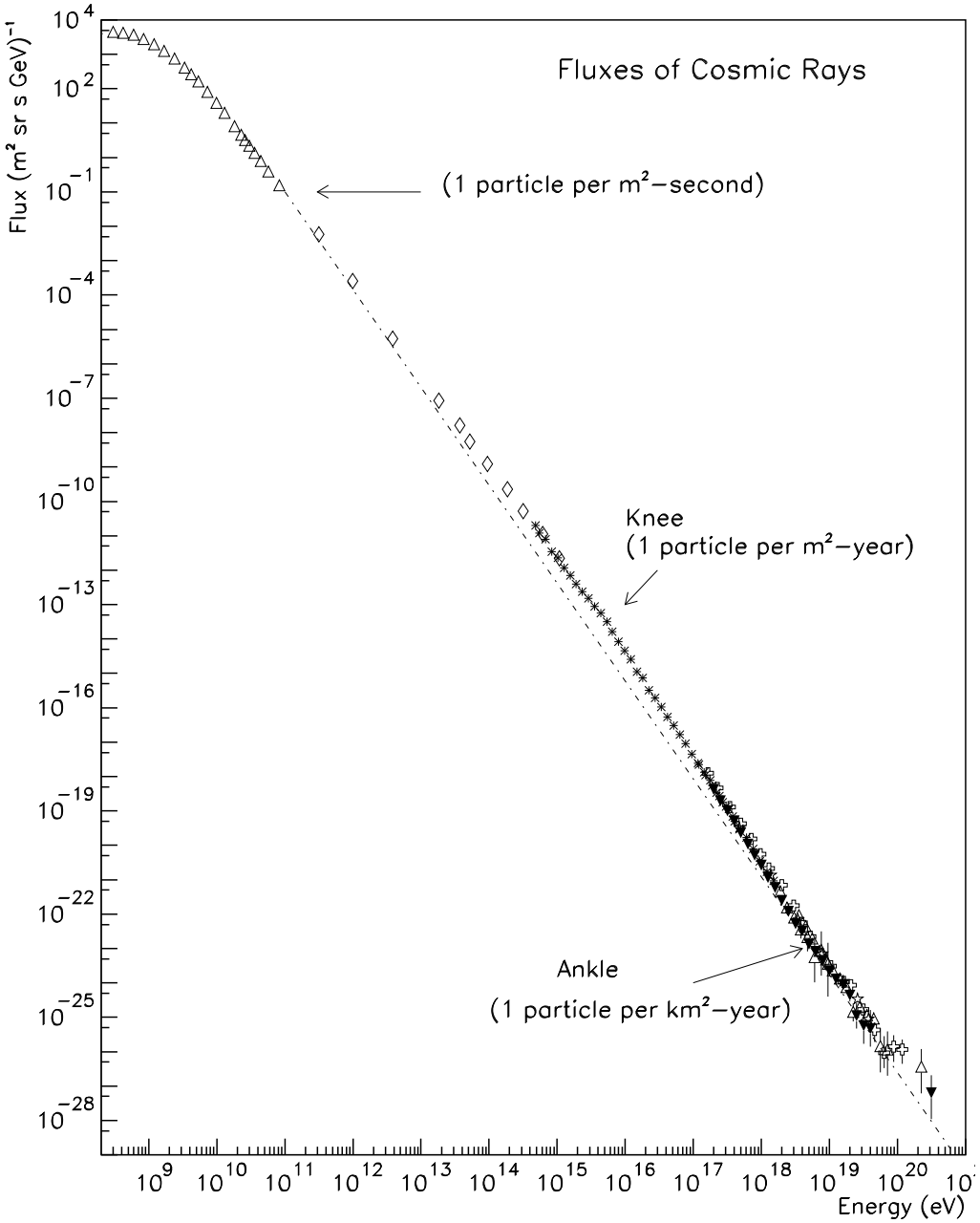

Figure 2.2: Measured energy spectrum of primary cosmic rays [11].

The ankle is located at an energy of about 4×10^{18} eV. Here, the spectral index changes back to about 2.7, thus flattening the spectrum again. This flattening is often taken as a transition from galactic sources situated within the Milky Way to extragalactic sources with different composition [12]. However, the exact origin of the ankle is not yet fully understood and thus it is still a subject of research.

In Fig. 2.3, the energy spectrum of primary cosmic rays above the knee as measured by different experiments is shown. In order to emphasize the structures con-

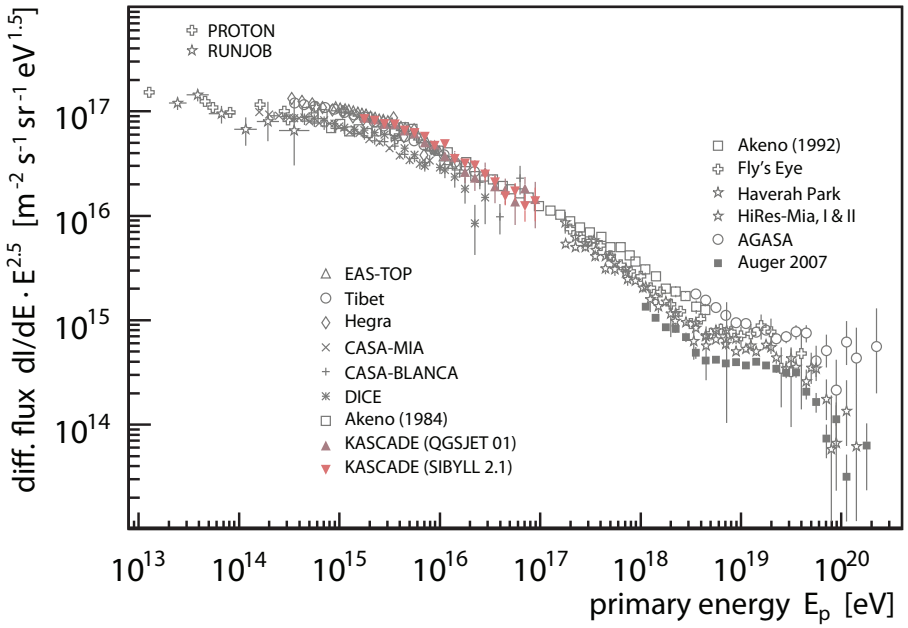

Figure 2.3: Energy spectrum of primary cosmic rays above the knee, measured by different experiments; the differential particle flux is multiplied by a factor of $E^{2.5}$ to emphasize structures; data points measured by the Pierre Auger Observatory are marked by grey quadrates; see [3] for a complete list of references.

tained within the spectrum, the differential flux is multiplied by a factor of $E^{2.5}$. Thus, the knee and the ankle are cleary visible. In addition, another feature can be seen at the end of the spectrum: the GZK cutoff. This suppression of the particle flux at ultra-high energies ($\gtrsim 6 \times 10^{19}\,\mathrm{eV}$) was predicted by Greisen, Zatsepin and Kuzmin in 1966 [13, 14]. Protons (or heavier nuclei) from cosmic rays interact with photons of the cosmic microwave background (CMB) to produce pions in processes like

$$\begin{aligned} p + \gamma_{CMB} &\longrightarrow \Delta(1232)^+ \longrightarrow p + \pi^0, \\ p + \gamma_{CMB} &\longrightarrow \Delta(1232)^+ \longrightarrow n + \pi^+. \end{aligned}$$

Hence, there is an energy loss for ultra-high-energy particles due to these processes as long as the energy is above the threshold energy. Since it is assumed that the sources of UHECR are extragalactic ($> 100\,\mathrm{MPc}$ away), a cutoff in the energy spectrum should be seen. With only the data shown in Fig. 2.3, it is not clear whether the GZK cutoff is present in the energy spectrum. For example, measurements by the High Resolution Fly's Eye (HiRes) experiment [15] are compatible with the prediction while in the data taken with the Akeno Giant Air Shower Array (AGASA) [10], no suppression is visible. However, more recent results from the Pierre Auger Observatory show a suppression of the flux at highest energies with a significance of more than 20σ [16].

2.3. Extensive air showers

When primary cosmic rays penetrate the earth's atmosphere, they may interact with an atmospheric constituent, in most cases a nitrogen nucleus. In this first interaction, a multitude of secondary particles is produced, which themselves interact with nuclei of the atmosphere, thus initiating a cascade. In each generation of the development of this extensive air shower, the secondary particles carry less energy per particle than in the generation before. The total number of particles increases until the shower maximum is reached at an atmospheric depth of X_{max}, where the energy of the secondary particles is too small to produce new particles. From then on, the number of particles decreases. X_{max} depends on the type of the primary particle as well as on the primary energy. In detail, the first few interactions taking place during the startup phase of the shower are crucial for the further development of the shower, including the position of X_{max}. A simplified depiction of the longitudinal shower development is shown in Fig. 2.4. A more detailed illustration of the development of an extensive air shower and the main processes taking place during the shower development can be seen in Fig. 2.5(a).

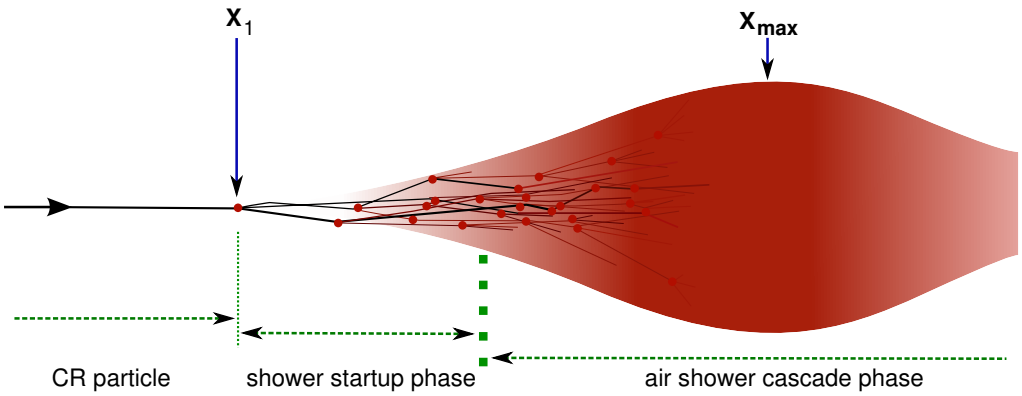

Figure 2.4: Simplified depiction of the longitudinal development of an extensive air shower [17].

In Fig. 2.5(b), the lateral view of a typical air shower is depicted. The secondary particles produced during the shower development form a curved disk with a thickness in the order of magnitude of meter and a surface area in the order of magnitude of square-kilometer, propagating nearly with the speed of light. In the center of the disk, i.e. close to the shower axis defined by the incoming direction of the primary particle, the particle density is higher than at the edges. In addition, the thickness of the disk increases toward the edges. In total, a typical proton shower with a primary energy of 10^{15} eV contains about 10^6 secondary particles [18]. Most of these particles can be subsumed in one of the three categories described in the following sections.

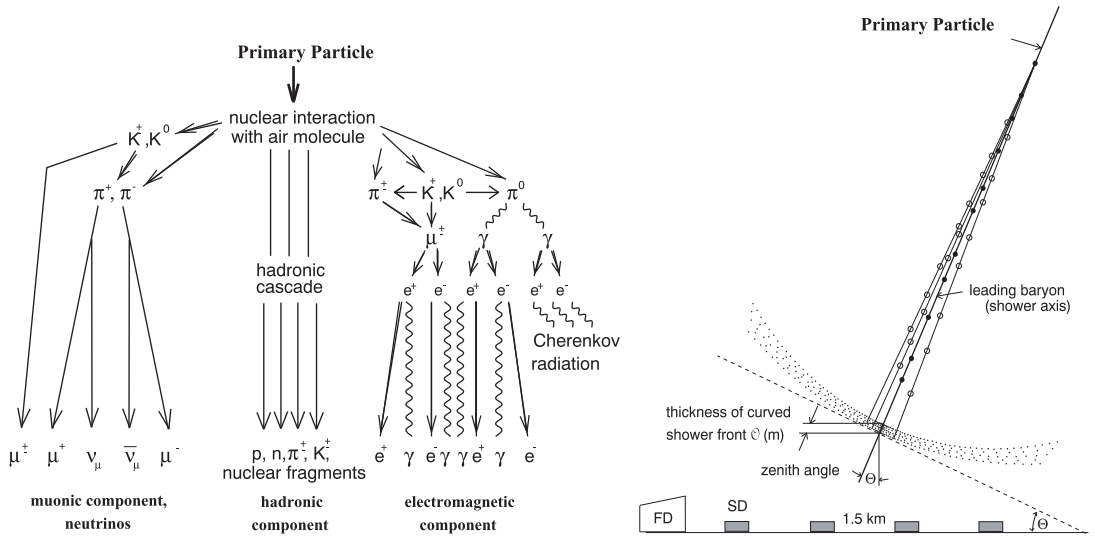

(a) (b)

Figure 2.5: Schematic development of an extensive air shower [19]; (a) main processes taking place during the shower development; (b) lateral view of a typical air shower.

2.3.1. Hadronic component

Hadrons only account for about 1 % of the particles of an extensive air shower [20]. Nevertheless, the hadronic component is very important for the shower development, since it feeds the other components. The first interaction of a primary cosmic ray nucleus with an atmospheric nucleus initiates a hadronic cascade of secondary particles, mostly pions, although kaon production is also possible. Charged pions in turn interact with atmospheric nuclei to produce further secondary particles, while neutral pions most likely decay via

$$\pi^0 \longrightarrow \gamma + \gamma,$$

since their interaction length is very long compared to their decay length [18]. Further secondary hadrons are produced until the energy per particle drops below the pion production threshold. From then on, the remaining secondary hadrons lose their energy by ionization until they decay and the hadronic cascade dies out. Since the transverse momenta of the secondary hadrons are small compared to their total momenta, the hadronic component forms a narrow cone with a spread of the order of magnitude of 10 m around the shower axis defined by the trajectory of the primary particle [20].

2.3.2. Electromagnetic component

When a photon from the decay of a neutral pion interacts with an atmospheric nucleus, it may produce an electron-positron pair:

$$\gamma + \text{nucleus} \longrightarrow e^+ + e^- + \text{nucleus}.$$

The electrons and positrons may in turn emit photons in bremsstrahlung processes:

$$e^\pm + \text{nucleus} \longrightarrow e^\pm + \gamma + \text{nucleus}.$$

These processes take place alternatingly, thus forming an electromagnetic cascade. Other processes like photoelectric and Compton effect for photons or ionization for electrons can be neglected with respect to the high energies of the particles in the cascade [20]. Since many neutral pions are produced in the hadronic cascade along the primary particles trajectory, the electromagnetic component of an extensive air shower is in fact a superposition of all the electromagnetic cascades initiated by the decay of the single pions. In addition, the short radiation lengths of electrons and photons lead to a rapid absorption of these particles. Nevertheless, the electromagnetic component comprises about 89 % of the total number of particles in an extensive air shower [20].

Depending on the energy of the primary particle, the lateral spread of the electromagnetic component can reach values of up to several kilometers due to multiple Coulomb scattering. The lateral spread can be described by the Nishimura-Kamata-Greisen function (NKG function, [21, 22]). The area density of electrons ρ_e, as a function of the distance r from the shower axis, is given by

$$\rho_e(r) = \frac{N_e}{2\pi r_M^2} \frac{\Gamma(4.5-s)}{\Gamma(s)\,\Gamma(4.5-2s)} \left(\frac{r}{r_M}\right)^{s-2} \left(1+\frac{r}{r_M}\right)^{s-4.5}, \tag{2.2}$$

where N_e is the total number of electrons in the shower and r_M is the Moliére radius ($r_M = 100\,\text{m}$ at an atmospheric depth of $820\,\text{g}\,\text{cm}^{-2}$ [20]). s parameterizes the age of the shower. It is defined as 0 at the point of shower initiation, 1 at the shower maximum and 2 at the point where the shower dies out.

An electromagnetic cascade can also be initiated by a primary electron or photon. In this case, the forming of a hadronic component is improbable and the extensive air shower is purely electromagnetic.

2.3.3. Muonic component

The muonic component of an extensive air shower is fed by the hadronic component much in the same way the electromagnetic component is fed, only in this case muons

are produced in the decay of charged mesons, for example through the following decay channels:

$$\begin{aligned} \pi^{\pm} &\longrightarrow \mu^{\pm} + \nu_{\mu}(\bar{\nu}_{\mu}), \\ K^{\pm} &\longrightarrow \mu^{\pm} + \nu_{\mu}(\bar{\nu}_{\mu}), \\ K^{\pm} &\longrightarrow \pi^{0} + \mu^{\pm} + \nu_{\mu}(\bar{\nu}_{\mu}). \end{aligned}$$

Most of the muons are generated in the early stages of an extensive air shower, because at high altitudes the density of the air is low, and therefore, the hadronic interaction length is large compared to the decay length of the charged mesons [18]. Thus, most charged mesons produced as secondary particles in the early stages of the hadronic cascade decay, thereby feeding the muonic component. Muons lose their energy mainly in ionization processes and are not affected by the strong interaction. Therefore, they pass the atmosphere nearly undisturbed. For low energy muons, a decay via

$$\mu^{\pm} \longrightarrow e^{\pm} + \nu_{e}(\bar{\nu}_{e}) + \bar{\nu}_{\mu}(\nu_{\mu})$$

is probable since, in this case, the muon lifetime is scarcely affected by relativistic time dilatation. Hence, decaying low energy muons might also end up feeding the electromagnetic component. The lateral spread of the muonic component is mainly caused by the transverse momenta of the decaying charged mesons, since the muons are preferentially emitted along the line of flight of the decaying mesons. The contributions of multiple scattering and bremsstrahlung are suppressed by a factor of $(m_e/m_\mu)^2$ compared to electrons, thus, these processes have only a small effect on the lateral distribution.

In total, the muonic component comprises about 10 % of the particles in an extensive air shower [20]. Nevertheless, they account for about 80 % of the secondary particles from extensive air showers measured at sea level [18], since they pass the atmosphere nearly undisturbed and can thus reach sea level even when the hadronic and the electromagnetic component have been fully absorbed.

Neutrinos are closely connected to the muonic component of an air shower. With each muon, a neutrino is produced in turn, and in the decay of a muon, even two neutrinos are produced. However, the interaction cross section for neutrinos is very small. Therefore, they play an inferior role in air shower measurements and will not be discussed here any further.

3. The Pierre Auger Observatory

One of the major challenges for cosmic ray experiments is the rapid decrease of the flux of primary cosmic radiation from about one particle per square meter and second in the TeV regime to one particle per square kilometer and year and less at the ankle (see Fig. 2.2). Beyond 100 TeV, only indirect measurements with air shower experiments at ground level are an option. For measurements in the energy region of the ankle and beyond, however, a very large area has to be covered by the experiment in order to acquire a considerable amount of data in an acceptable period of time.

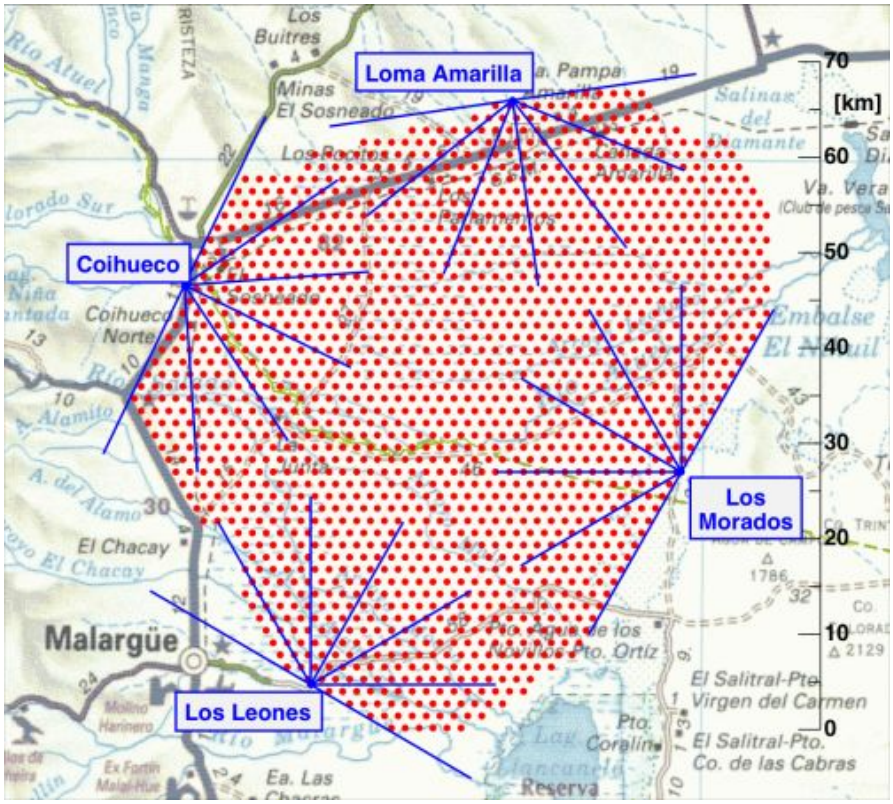

Figure 3.1: The layout of the southern site of the Pierre Auger Observatory near Malargüe, Argentina [23]; the 1660 surface detector stations are represented by dots; the field of view of 30° of each of the 24 fluorescence telescopes, arranged in four sites, is indicated by lines.

The Pierre Auger Observatory is an international air shower experiment specifically designed to study ultra-high-energy cosmic rays (UHECR) in the EeV range [24]. The measurements taken in this energy region will enable the astroparticle physics community to tackle fundamental issues like the energy spectrum or the origin of UHECR and the underlying acceleration mechanisms. Furthermore, the measurements taken by the Pierre Auger Observatory can be used to determine anisotropies in the distribution of arrival directions of primary cosmic rays and thus help to re-

veal possible sources of cosmic rays in the universe [25].

To perform these measurements, the Pierre Auger Collaboration employs a two-fold approach, using a surface detector (SD) array overlooked by fluorescence detectors (FD). The surface detector array, comprised of water Cherenkov detectors, records particles from extensive air showers at ground level, while the fluorescence telescopes observe the ultraviolet fluorescence light produced by the same air showers in the atmosphere above the array. The combination of these two complementary techniques into a hybrid approach allows for measurements with unprecedented accuracy due to the possibility of cross-calibration between the single detector components.

To achieve full sky coverage, the Pierre Auger Observatory is designed as a cosmic ray observatory with two sites, one in the southern and the northern hemisphere respectively. However, at the time of this thesis, only the southern site has been completed, while the northern site is still in the planning stage [26].

The southern site of the Pierre Auger Observatory is located in the Pampa Amarilla near the town of Malargüe in the province of Mendoza, Argentina (35° S, 69° W). The layout of the site is depicted in Fig. 3.1. The SD array consists of about 1600 water Cherenkov detectors, arranged in a hexagonal pattern with a spacing of 1.5 km, thus covering an area of about 3000 km^2. The array is overlooked by 24 fluorescence telescopes located in four buildings at the perimeter of the SD array. The Pampa Amarilla has been chosen as a site because of several almost unique conditions. The detector array is located on an elevated plateau at the base of the Andes, at an average altitude of 1400 m above sea-level, corresponding to an average atmospheric depth of 875 g cm^{-2}. The proximity to the Andes forwards almost perfect weather conditions with little precipitation and mostly clear sky during the entire year. In addition, there are no major settlements in the vicinity. Thus, there is almost no light pollution in the night sky resulting from a multitude of artificial lights on the ground, which is a major criterion for the efficient operation of fluorescence detectors.

In the following sections, the surface and fluorescence detectors will be described in detail. Furthermore, a brief summary of the enhancements that are currently being planned and developed for the southern site of the Pierre Auger Observatory will be given.

3.1. Surface detectors (SD)

The SD array is designed to observe the lateral shower profile at ground level. With its duty cycle of almost 100 %, it provides the bulk of the data recorded by the Pierre Auger Observatory [27]. Each of the 1660 SD stations (Fig. 3.2) consists of a cylindrical polyethylene tank with a diameter of 3.6 m, filled with 12 m^3 of purified water, corresponding to a water level of 1.2 m inside the tank. Three photomultiplier

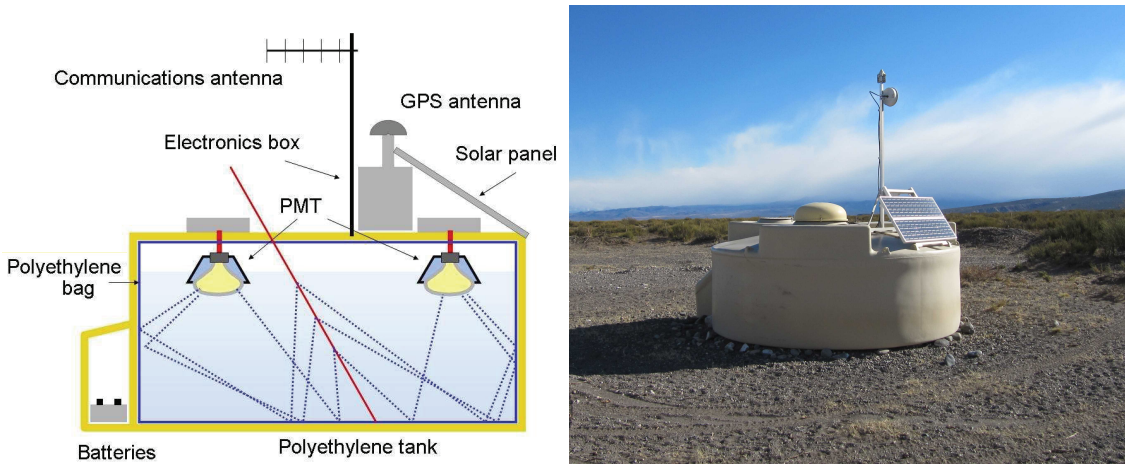

(a) (b)

Figure 3.2: (a) Schematic depiction of a surface detector station [28]; (b) a surface detector station deployed in the field.

tubes (PMTs) are optically coupled to the water and symmetrically positioned on top of the tank with a distance of 1.2 m between each other. Each detector is devised to work completely stand-alone, thus, every tank is equipped with a battery box and a solar power system providing the 10 W average power required for the tank electronics [29]. A GPS (Global Positioning System) unit is installed at each tank as a basis for time synchronization between the detector and the Central Data Acquisition System (CDAS) as well as for providing precise information about the tank's position. The communication between the detector and the CDAS is achieved wirelessly via one of the four communication beacons located near the FD sites at the perimeter of the array.

To detect charged particles from extensive air showers, the Cherenkov effect is exploited [30]. When the velocity of a charged particle traversing a medium is greater than the speed of light in this medium, Cherenkov light is emitted by this particle in a cone along its trajectory. The Cherenkov light produced in the tank by secondary particles from extensive air showers, mostly muons and electrons, is detected by the PMTs mounted on top of the tank and converted into a current pulse. To increase the amount of Cherenkov light collected, a reflective layer of high-density polyethylene fabric covers the inside of the tank. The signals from the PMTs are read out and digitized by Flash Analog-to-Digital Converters (FADCs) at a rate of 40 million samples per second. The PMT signal traces recorded by the FADCs are stored for 10 s so they can be sent to the CDAS on demand [29].

Since the detector stations are designed to work completely independent of each other, they are able to calibrate themselves using muon signals [29]. To perform the calibration, the measured spectrum is compared to the known energy distribution of

muons. The signals are measured in units of vertical equivalent muons (VEM), where 1 VEM corresponds to the amount of Cherenkov light produced by a single muon traversing the tank vertically. The corresponding current pulse from each PMT is denoted by I_{VEM}^{peak}. To perform additional calibration studies, twins and triplets have been installed, where a pair or a triple of detector stations is placed with a distance of 11 m between the single tanks, which therefore see the same part of the shower and provide comparable data.

3.1.1. SD trigger system

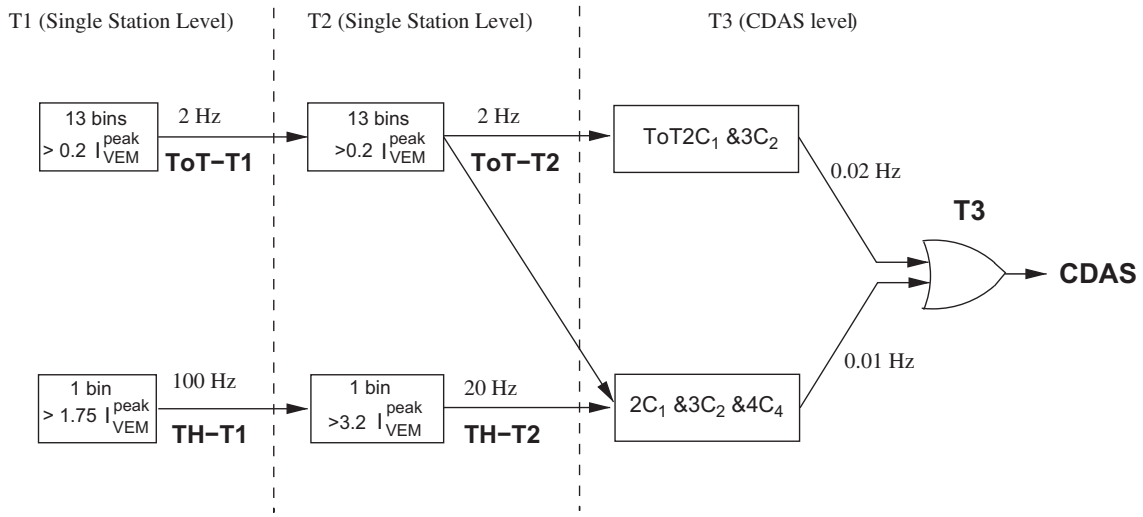

Figure 3.3: Schematics of the hierarchy of the SD trigger system [27].

The SD trigger system is designed to operate in a wide range of primary energies from 10^{17} eV to 10^{21} eV, reaching full efficiency at 3×10^{18} eV independent of the zenith angle and the type of the primary particle [27]. The SD trigger system is hierarchical, consisting of two local trigger levels (T1, T2) and a coincidence level (T3) formed at the CDAS. Two additional offline triggers (T4, T5) have to be fulfilled for the recorded shower data to be taken into account for analysis. The hierarchy of the SD triggers at single station and CDAS level is schematically depicted in Fig. 3.3.

The T1 trigger level consists of two different trigger modes: a pure threshold trigger requiring a coincidence of all three PMTs (TH-T1) to detect showers with very large zenith angles, and a Time-over-Threshold trigger (ToT-T1) requiring a coincidence in two out of three PMTs in at least 13 FADC time bins (i.e. 325 ns) in a sliding window of 120 time bins (i.e. 3 μs) [27]. The ToT-T1 is employed to detect less inclined showers with the respective shower core closer to an SD station. The T1 triggers to be reported to the CDAS have to pass T2 level as well. The ToT-T1 is always promoted to T2 level, while the TH-T1 signals have to pass another, higher, threshold to be promoted. The latter is required to further reduce the transmission load on the wireless communication system.

The third trigger level (T3) initiates the data acquisition from the single detector stations. It is formed by the CDAS, which selects stations whose T2 triggers are compatible with an air shower event, with respect to both time and space. If one of the two T3 conditions, differing only in the spatial configuration of the triggered stations, is fulfilled, the CDAS requests the corresponding FADC traces from the single stations. All data obtained from events that meet the T3 requirements are stored. An additional physics trigger (T4) performs real shower selection on the stored data offline. Finally, the T5 trigger, which can be considered a quality cut, ensures that the reconstruction of the arrival direction and the energy estimation from the shower data is not subject to large deviations, for example by rejecting events close to the border of the SD array.

3.2. Fluorescence detectors (FD)

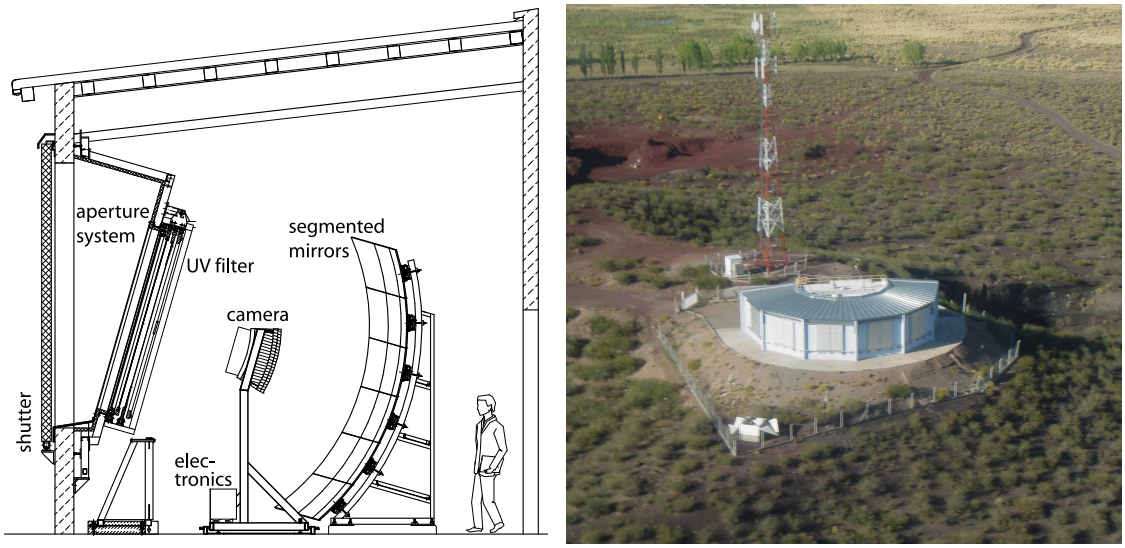

(a) (b)

Figure 3.4: (a) Schematic depiction of a fluorenscence telescope [31]; (b) aerial view of the fluorescence detector site Los Leones [1].

The FD system of the Pierre Auger Observatory complements the SD measurements of the lateral shower profile on ground level by recording the longitudinal shower development in the atmosphere above the SD array. The FD consists of 24 fluorescence telescopes arranged in four sites at the perimeter of the SD array. The field of view of a single telescope is $30° \times 30°$ with the observation direction of its respective center inclined to 16°. Thus, each FD site provides a field of view of $180° \times 30°$ toward the center of the SD array, observing the sky above between 1° and 31° elevation [31].

In Fig. 3.4(a), the design of a fluorescence telescope is shown. The telescope is a modified Schmidt camera: fluorescence light from the air shower enters the telescope through a UV-passing filter window and an aperture system. It is then focused by a segmented mirror onto a pixel camera, consisting of 440 PMTs, which are read out electronically [31].

The measurement of the longitudinal shower profile is based on the excitation of nitrogen molecules in the atmosphere by secondary particles of extensive air showers. When the excited molecules fall back to their ground states, they emit light in the ultraviolet range of the wavelength spectrum. This light can be detected by the fluorescence detectors as a calorimetric measure for the longitudinal shower profile from which the energy of the primary cosmic ray can be reconstructed. To correctly reconstruct the primary energy, it is crucial to record all and only the fluorescence light from the shower. Thus, the FD can only operate in moonless, cloudless nights, which leads to a duty cycle of about 13 % [31]. The detected fluorescence light also depends on the atmospheric conditions, for instance the pressure, the temperature, or the amount of aerosols in the atmosphere. Therefore, the atmosphere is constantly monitored, for example with a LIDAR (Light Detection and Ranging) system [32].

3.3. Enhancements of the southern site

At the moment, three major enhancements of the southern site are projected. AMIGA (Auger Muons and Infill for the Ground Array) and HEAT (High Elevation Auger Telescopes) will lower the energy threshold of the experiment to 10^{17} eV, while AERA (Auger Engineering Radio Array) will complement the existing detection techniques by introducing additional radio detectors into the Auger array. The AMIGA enhancement will be covered in detail in Chapter 4, while the other two enhancements will be discussed briefly in the following paragraphs.

The HEAT enhancement consists of three additional fluorescence telescopes near the FD site Coihueco (Fig. 3.5(a)). These additional telescopes are similar to the existing fluorescence telescopes, however, it is possible to tilt the HEAT telescopes upward by 29° to extend the field of view above the range of the regular telescopes [33]. Through the combination of measurements of the regular FD telescopes and HEAT, it is possible to record showers initiated by primary cosmic rays with an energy below the current threshold, since they are known to develop higher in the atmosphere. In addition, the tiltable construction of the HEAT telescopes offers the opportunity to measure in coincidence with the regular FD telescopes in the same field of view and thus allows for a cross-calibration between the two systems.

Within the scope of the AERA enhancement, it is planned to set up an independent radio detector array with a size of 20 km^2 to explore the potential of the radio detection technique for cosmic ray induced extensive air showers. The radio detector array will consist of 161 autonomous, self-triggered detector stations (Fig. 3.5(b)),

(a) (b)

Figure 3.5: (a) The three HEAT telescopes tilted upward [33]; (b) a radio detector station installed at the AERA site [34].

which are sensitive to frequencies from 30 to 80 MHz [34]. The AERA detector stations will record the pulse-shaped electromagnetic signals that charged particles from an extensive air shower emit in the magnetic field of the earth. From these signals, the longitudinal shower development can be reconstructed. Therefore, AERA measurements are comparable to fluorescence measurements, but with a much higher duty cycle. Furthermore, since AERA is collocated with the HEAT and AMIGA enhancements, the observation of air showers in coincidence with these systemshehe will allow for a detailed study of the radio emission processes taking place within an extensive air shower for primary energies below 10^{19} eV [34].

4. The AMIGA enhancement

The AMIGA enhancement of the southern site of the Pierre Auger Observatory consists of two components: on the one hand, additional surface detectors will be placed in between the existing detectors in a 23.5 km^2 infill array located 6 km away from the FD site Coihueco. On the other hand, each of the detector stations of the infill array will be equipped with additional underground muon counters [35]. In the following chapter, the AMIGA enhancement, its scientific motivation as well as the two components mentioned before, will be described in detail.

4.1. Scientific motivation

The Pierre Auger Observatory was originally designed to detect cosmic rays at highest energies. Therefore, the SD trigger system reaches full efficiency at 3×10^{18} eV (see Section 3.1.1). One of the main objectives of the AMIGA enhancement is to lower the energy threshold for full trigger efficiency to 10^{17} eV, so that the regions around the proposed second knee and the ankle in the energy spectrum of primary cosmic rays are fully covered by the Pierre Auger Observatory (Fig. 4.1).

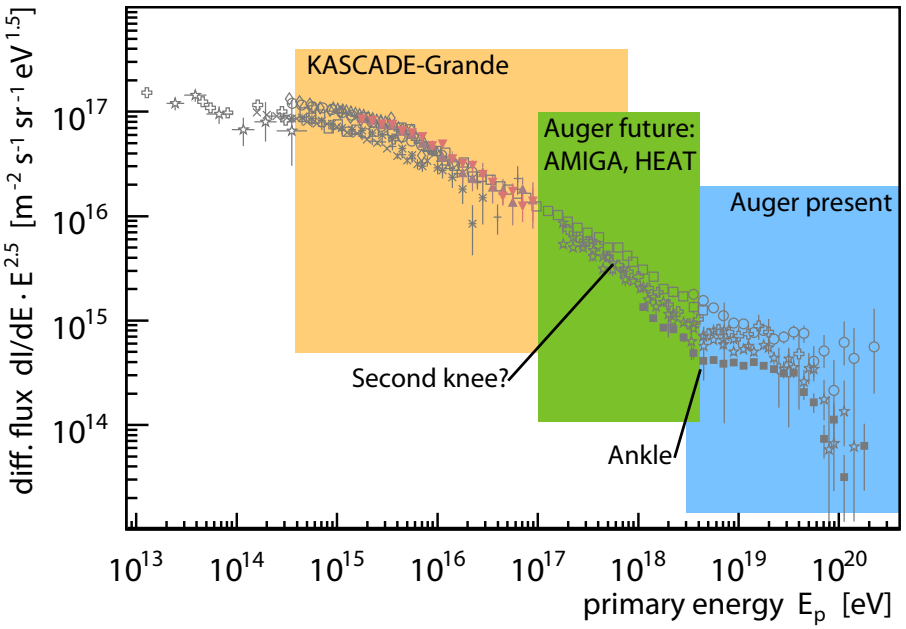

Figure 4.1: Comparison of the energy ranges of the spectrum of primary cosmic rays covered by KASCADE-Grande, the present Auger detector systems and the future Auger enhancements AMIGA and HEAT [3].

The targeted energy range of the Auger enhancements is of high astrophysical significance. In this energy range, a transition from galactic to extragalactic origin of primary cosmic rays is generally expected. However, the exact energy, where this transition occurs, is not yet clear. The validation of the existence of a second

knee could help to further distinguish between the prevailing astrophysical models describing the production and propagation of primary cosmic rays in the Milky Way [36]. The interpretation of a second knee also affects the interpretation of the ankle. If the transition from galactic to extragalactic components already occurs at lower energies, the ankle could be understood as the result of pair creation by protons in the CMB, or as the result of diffusive propagation of extragalactic nuclei through cosmic magnetic fields [36].

An additional advantage of lowering the energy threshold down to 10^{17} eV is the resulting overlap of the energy ranges covered by the Pierre Auger Observatory and KASCADE-Grande (Karlsruhe Shower Core and Array Detector Grande, [37]) which may be of fundamental importance in order to validate results.

4.1.1. Composition studies

To properly distinguish between astrophysical models, it is not sufficient to take only the shape of the energy spectrum of primary cosmic rays into account. The variation of the composition as a function of the primary energy provides an additional way to differentiate between the galactic and extragalactic components [35]. It is therefore of great importance to correctly ascertain the type of primary particle from the recorded shower data. For this purpose, a variety of parameters can be employed, for example the position of the shower maximum X_{max}, which is used by most analyses so far, or the interpolated signal strength measured by the surface detectors at 600 m distance from the shower core S_{600}. However, reconstructing the type of the primary particle from different parameters leads to partly conflicting results. The AMIGA enhancement will provide an additional possibility to determine the type

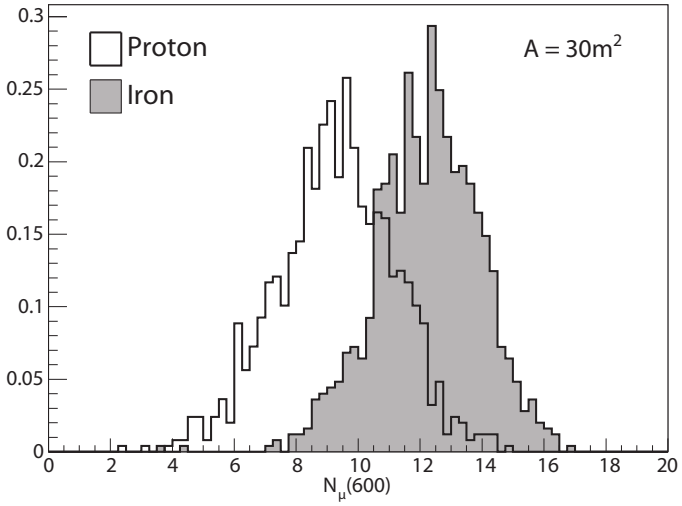

Figure 4.2: Distribution of the simulated and reconstructed number of muons at a distance of 600 m from the shower core for proton and iron primaries and a 30 m^2 muon detector [35].

of the primary particle by measuring the number of muons inside an extensive air shower. From these measurements, the number of muons on ground at a distance of 600 m from the shower core $N_\mu(600)$ can be reconstructed. The simulation results for $N_\mu(600)$ shown in Fig. 4.2 suggest that a differentiation between proton and iron primaries is possible. In order to quantify how reliable this differentiation is for a given parameter q, the discrimination power η is introduced:

$$\eta(q) = \frac{|\langle q_{proton}\rangle - \langle q_{Fe}\rangle|}{\sqrt{\sigma\left(q_{proton}\right)^2 + \sigma\left(q_{Fe}\right)^2}}, \tag{4.1}$$

where $\langle q_{proton}\rangle$ and $\langle q_{Fe}\rangle$ are the mean values of the parameter q for proton and iron primaries and $\sigma\left(q_{proton}\right)$ and $\sigma\left(q_{Fe}\right)$ are the standard deviations of these parameters [38]. The higher $\eta(q)$, the better q is suited to distinguish between proton and iron primaries.

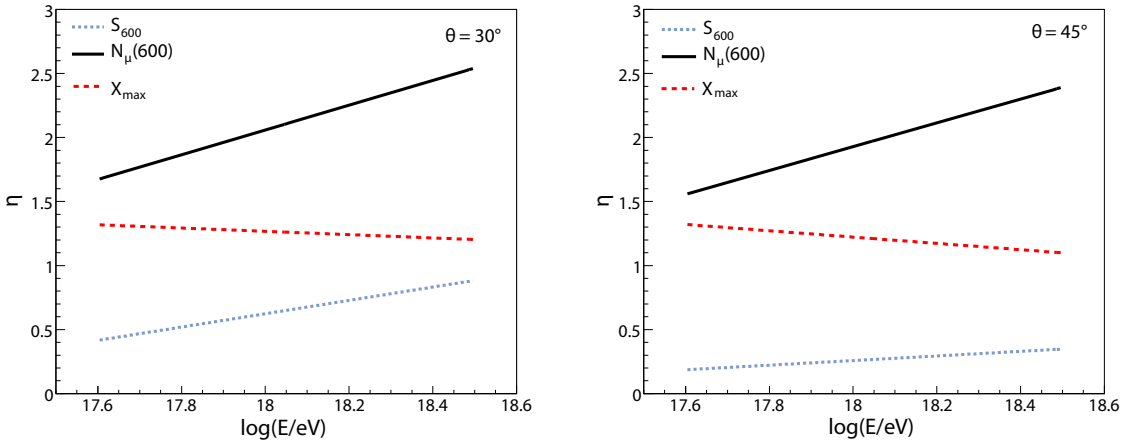

Figure 4.3: Comparison of the discrimination power η as a function of the primary energy for different parameters and showers with zenith angles of 30° and 45° [38]; the position of the shower maximum X_{max}, the interpolated signal strength at 600 m distance from the shower core S_{600} and the number of muons at the same distance $N_\mu(600)$ are shown.

In Fig. 4.3, the discrimination powers for X_{max}, S_{600} and $N_\mu(600)$ as a function of the primary energy for two different zenith angles are shown. In both cases, $N_\mu(600)$ proves to be the best parameter to differentiate between proton and iron primaries. However, the number of muons inside an extensive air shower is directly proportional to the primary energy and thus its reconstruction is stronger affected by uncertainties in the determination of the primary energy than the other parameters [38]. In addition, the hadronic interaction model, on which the reconstruction is based, has to be taken into account. Therefore, even with the combination of several parameters, it is not possible to obtain a reliable classification into proton and iron primaries on an event-by-event basis. However, to distinguish between different astrophysical models, only the composition of a larger sample is needed, which can be estimated with reasonable accuracy using these parameters [39].

4.2. Infill array

The layout of the AMIGA infill array is shown in Fig. 4.4. The 66 additional detector stations are placed in between the existing detector stations of the regular SD array in the same hexagonal pattern, although with smaller spacing. The total area covered by the 42 stations of the 750 m infill array is 23.5 km^2. With the 750 m infill array, the energy threshold for 100 % trigger efficiency can be lowered to 4×10^{17} eV [35]. To further decrease the threshold to the desired 10^{17} eV, an additional graded infill array is installed with an even smaller spacing of 433 m. The graded infill array consists of 24 detector stations on a total area of 5.9 km^2. The comparatively small areas covered by the infill array and the graded infill array are sufficient to acquire reasonable statistics since the flux of primary cosmic rays rapidly increases with decreasing primary energy (see Section 2.2).

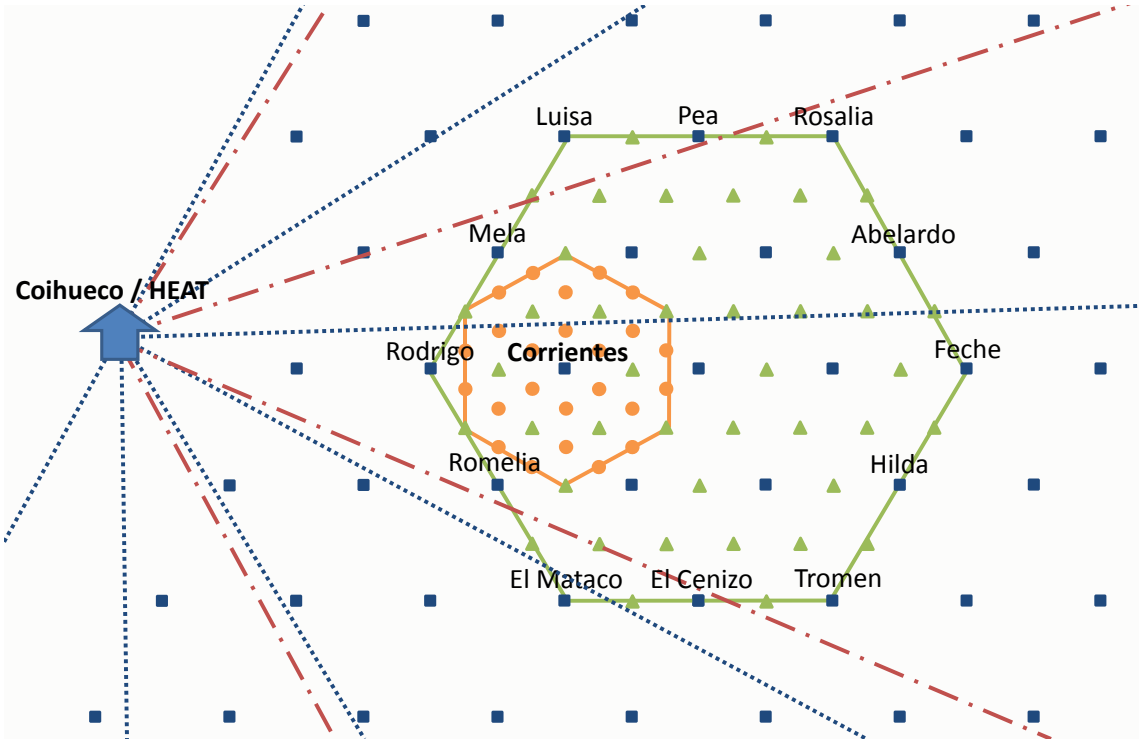

Figure 4.4: The layout of the AMIGA infill array; detector stations of the regular SD array are represented by quadrates and partly denoted with their names; SD stations of the 750 m and the 433 m infill array are marked with triangles and dots; the fields of view of the FD site Coihueco and the HEAT telescopes are indicated by dotted and dotdashed lines, respectively.

The location of the AMIGA infill array near the FD site Coihueco is overlooked by the HEAT telescopes (Fig. 4.4). Thus, through the combination of data taken by HEAT and the AMIGA infill array, hybrid measurements are possible even below the regular Auger energy range.

4.3. Muon counters

To measure the number of muons inside an extensive air shower, each of the 85 detector stations of the infill array (19 stations from the regular SD array plus 66 additional stations) will be equipped with an underground muon counter consisting of three independent modules (Fig. 4.5). The modules will be placed at a distance of about 5 m from the tank in a depth of 2.25 m, corresponding to a slant depth of 540 g cm^{-2} assuming standard rock with a density of 2.4 g cm^{-3}. The average power of 20 W needed to operate the muon counter modules is provided by additional solar panels and batteries, similar to the ones already used for the regular SD stations [35].

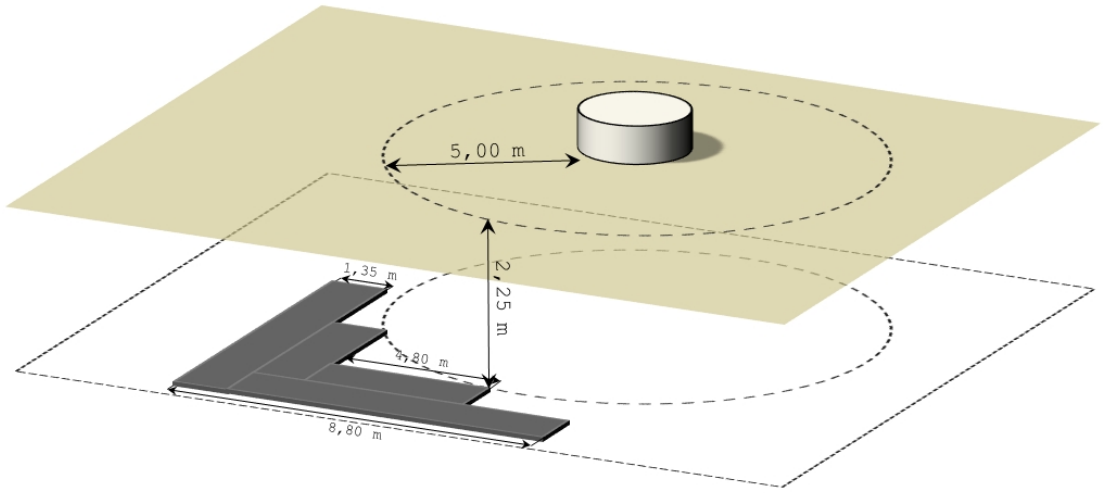

Figure 4.5: Possible layout of an AMIGA detector pair with the muon counter (bottom) buried alongside a regular SD station (top) [40]; in the layout shown here, one muon counter module is replaced by two smaller modules with half the size so that the muon counter consists of four independent modules instead of three.

Each muon counter module consists of 64 scintillator strips with a length of 400 cm, a width of 4.1 cm and a height of 1.0 cm, thus each muon counter covers a total area of about 30 m^2 [41]. The scintillator strips are similar to the ones used in the MINOS experiment (Main Injector Neutrino Oscillation Search, [42]). The strips are made of extruded polystyrene doped with fluor and co-extruded with a TiO_2 reflective coating. Each strip has a groove on the top side, into which a wavelength shifting optical fiber is glued (Fig. 4.6(a)). The purpose of these fibers is to guide the light emitted by the scintillators to a 64 channel multi-anode PMT and to shift the wavelength of the signals into the optimal range of the spectrum for the PMT used in the setup.

The electronics of a single muon counter module is placed in the center of the module with 32 scintillator strips at each side. The electronics itself (Fig. 4.6(b)) consists of a series of printed circuit boards (PCBs), handling the acquisition and

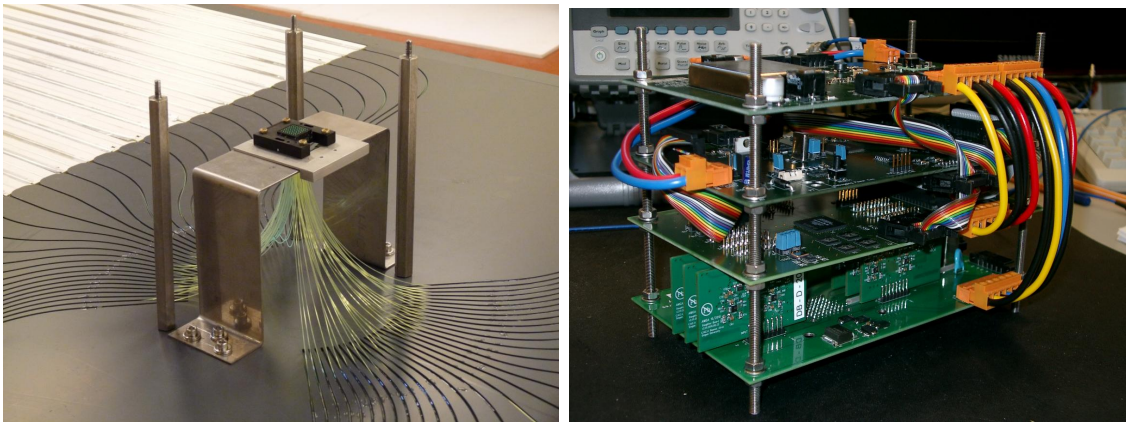

(a) (b)

Figure 4.6: (a) Detailed view of the optical fibers between the scintillator strips (background) and the optical connector for the 64 channel multi-anode PMT (center) [43]; (b) the electronics package for the muon counter modules.

the processing of the signals from the PMT as well as the communication with the surface detector and the power distribution for the operation of the module. Here, only a brief summary of the muon counter electronics will be given, a detailed description can be found in [40, 44].

The signals from the 64 PMT channels are transformed into digital data by discrimators, whose threshold levels can be controlled independently for each channel. The digitized pulses are read out by a field-programmable gate array (FPGA) at a sampling rate of 320 MHz and continuously stored in a circular buffer within the FPGA. Upon reception of a trigger signal, which can be provided either internally (occupancy trigger, requiring a pre-defined number of channels showing a signal in the same time bin) as well as externally by a T1 signal from the respective surface detector, the following pulses are stored in a second buffer within the FPGA. The contents of both buffers are then stored in a static random-access memory (RAM) and can be sent to a single board microcomputer at the surface detector, which then wirelessly transmits both the SD and the muon counter data to the CDAS upon request.

4.3.1. Unitary cell

To test the baseline design of the AMIGA muon counters, an engineering array, the unitary cell, is projected. Within the scope of this unitary cell, seven SD stations of the 750 m infill array will be equipped with muon counters, forming a hexagon around a central station. However, the design of the muon counters for the unitary cell will, at least in the first stage of construction, differ from the envisaged final design in two points: firstly, each muon counter will consist of only one module instead

of three. Secondly, the FPGA will sample the signals not at the envisaged 320 MHz rate but rather at a slower rate of 80 MHz.

Figure 4.7: Deployment of the $5\,m^2$ prototype at the SD station Corrientes in November 2009 [45]; in order to retain access to the electronics installed in the center of the module (inside the grey casing), the prototype is equipped with a manhole (white tube).

As first steps toward the unitary cell, two prototype modules, differing only in their size, have been installed at the SD station Corrientes (see Fig. 4.4). The first $5\,m^2$ prototype with 200 cm strips has been deployed in November 2009 (Fig. 4.7), the second, larger, $10\,m^2$ protoype with 400 cm strips followed in September 2010. The construction of the rest of the unitary cell is projected to begin by April 2011. The unitary cell will then be operating for at least a year to test and improve the baseline design. It is planned to equip the rest of the infill array with muon counters starting by the middle of 2012.

5. Description of the simulation program

The main part of this thesis is dedicated to the simulation studies that have been performed to support the analysis of the data both muon counter prototypes are taking reliably since their deployment in the field. These simulations are based on the Geant4 (Geometry and Tracking 4) toolkit, a platform for the simulation of the passage of particles through matter using Monte Carlo methods [46, 47]. Geant4 provides a complete set of modular tools for all areas of detector simulation, employing an object-oriented approach using the `C++` programming language. The code is distributed freely under an open software license. Today, Geant4 has become a widely accepted basis for simulation studies not only in particle and astroparticle physics, but also in medical and space science.

In the following chapter, the simulation program that has been developed in the scope of this thesis, will be presented in detail. In addition, preliminary data recorded by the $5\,\mathrm{m}^2$ prototype muon counter, which motivated these simulation studies, will be presented.

5.1. Motivation: prototype data

At the time of this thesis, over 14 GB of data in 59 datasets with different trigger and threshold settings have been accumulated with the $5\,\mathrm{m}^2$ and the $10\,\mathrm{m}^2$ muon counter prototypes. As an example, the data from the dataset `10-03-23-HV950V-OCC8-PRESCALE0-THR100mV` will be presented here as a motivation for the simulation studies. The dataset has been recorded by the $5\,\mathrm{m}^2$ prototype in March 2010 with an eightfold occupancy trigger. Therefore, the dataset contains only events with at least eight scintillator strips simultaneously showing a signal in one time bin (12.5 ns). The discriminators were set to a threshold of 100 mV for each channel, corresponding to about 30 % of the average pulse-height of a single photo-electron in the electronics [45]. The high voltage for the PMT was set to 950 V. The prescaler was disabled, so that every event that triggered the electronics has been written to memory. In total, the dataset contains 183 863 events recorded during about 15 days. The average event rate for this measurement is 0.14 Hz.

In Fig. 5.1, four example events, which have been chosen arbitrarily from the dataset, are shown with the time plotted on the abscissa and the scintillator strip number shown on the ordinate. The scintillator strips are numbered consecutively, with strips 1 to 32 on one side of the module and strips 33 to 64 on the other side. On the time axis, an event can be divided into three regions: the noise region, the central trigger region and the signal region. In the case of an internal occupancy trigger, the trigger region is fixed around time bin 256, whereas in the case of an external T1 trigger, the trigger region is shifted due to signal delays in the cables from the surface detector to the muon counter module and in the detector itself. Before the trigger, only noise (e.g. thermal noise) is expected, while in the region

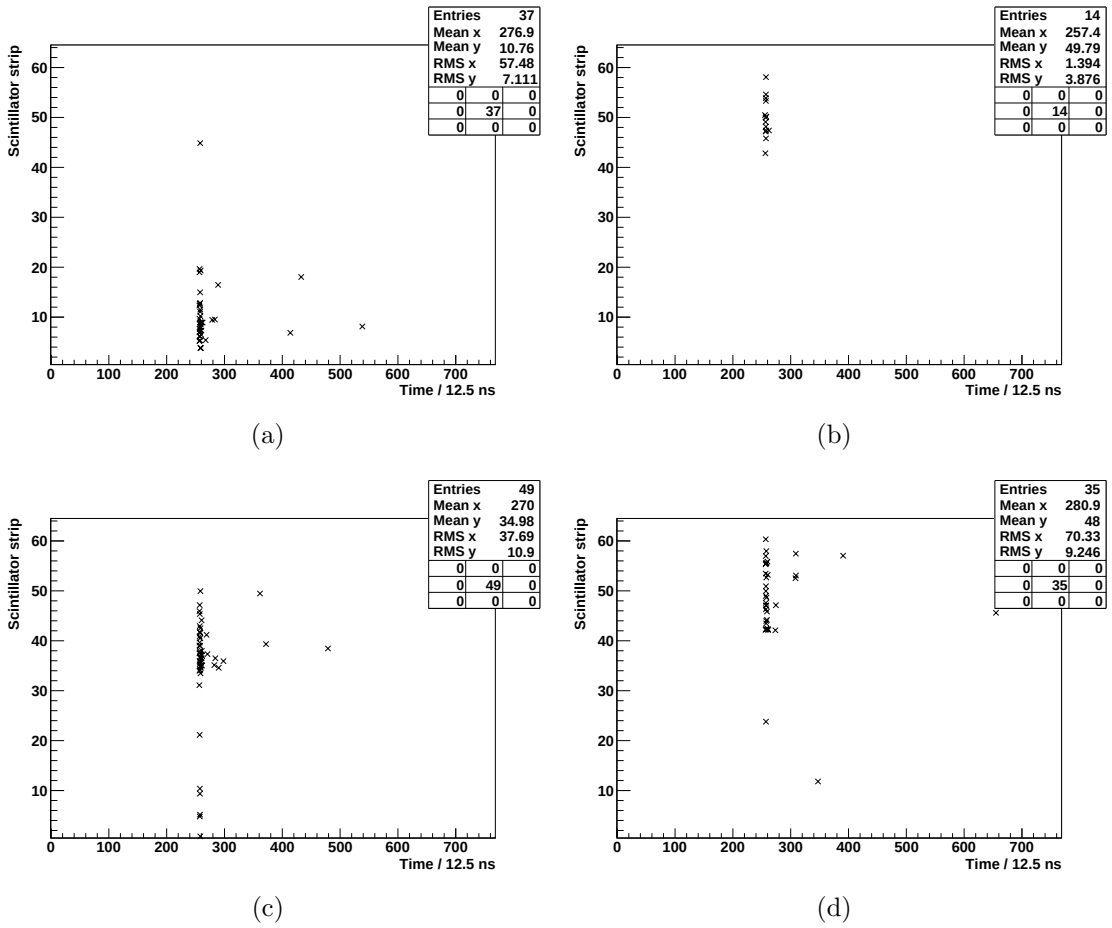

Figure 5.1: Four example events with occupancy trigger, recorded by the 5 m^2 prototype (dataset `10-03-23-HV950V-OCC8-PRESCALE0-THR100mV`, run 1070) [48].

after the trigger, signals from real muons and other particles show up as well. The time structure of the events becomes clearer when looking at the projection onto the time axis of the superposition of all events in the dataset (Fig. 5.2 (a)). Here, a narrow peak can be seen in the trigger region, with few activity in the noise region and more activity in the signal region. In addition, the time distribution shows two distinct features: firstly, the activity in the signal region is larger by at least a factor of 10 than in the noise region. This effect could be due to after-pulsing in the PMT, where a real signal pulse is followed by an after-pulse at a later time due to ionization of the residual rest gases inside the PMT [49]. Secondly, there is another peak in the time distribution right after the trigger peak. However, this peak is only apparent for certain channels of the PMT, all along one edge of the PMT. Thus, it can be assumed that the second peak in the time distribution is again related to the PMT. Nevertheless, the exact source of both features is not yet understood.

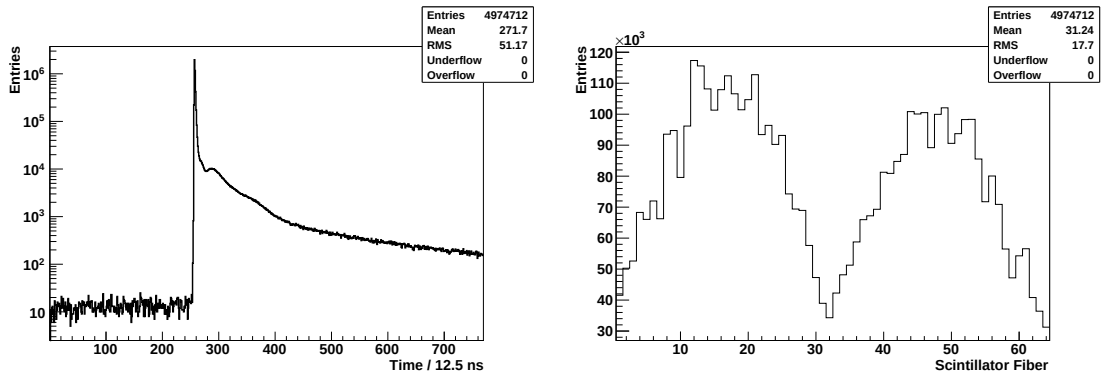

(a) (b)

Figure 5.2: Superposition of all events in the dataset `10-03-23-HV950V-OCC8-PRESCALE0-THR100mV` [48]; (a) time distribution; (b) distribution of hits on the scintillator strips.

When overlaying all events, the distribution of hits on the scintillator strips can be considered as well (Fig. 5.2(b)). Again, a certain structure is visible: at the edges of each half of the module (strips 1 to 32 and strips 33 to 64, respectively), the activity on the single strips decreases. Under the simplest assumption that each hit on the scintillator strips is due to one muon from an extensive air shower, the hits are expected to be uniformly distributed over the detector, since the detector area is very small compared to the average spread of an extensive air shower on ground level. However, as apparent from Fig. 5.1, the single hits are not uniformly distributed, but preferentially form clusters, where a number of strips, located near each other, is hit simultaneously. Since these clusters are uniformly distributed, a common origin for the single hits in one cluster, for example a muon producing secondary particles in the soil above the muon counter module, can be assumed. The shape of Fig. 5.2(b) can then be understood as an effect of the clustering and the occupancy trigger employed in this measurement. Scintillator strips close to the edges of the modules are less likely to be part of a cluster when a certain number of strips simultaneously showing signals is required. However, as for the time distribution, these are assumptions, which do not fully explain the observed features yet.

One major aim of the simulation studies performed for this thesis is to further investigate these clusters and their possible origin by simulating the passage of muons through the soil above the muon counters. Comparing the simulation results to the data obtained by the muon counter prototypes shows whether at least part of this data can be explained by local showers in the soil. Another important topic of the simulation studies is to determine the energy thresholds for different particle types to reach the detector and produce signals in the scintillator. These energy thresholds then serve as a basis for further simulation studies: for example, they can be used to optimize simulations with CORSIKA (Cosmic Ray Simulations for KASCADE, [50]), a program for the detailed simulation of extensive air showers.

5.2. Program structure

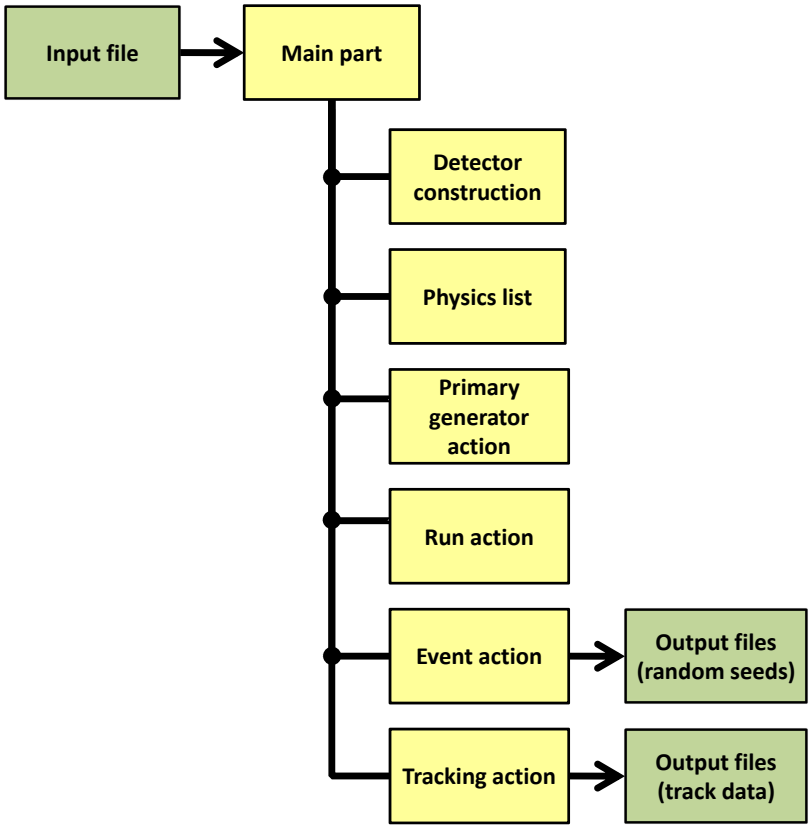

Figure 5.3: Schematic illustration of the simulation program; paths, where information and data only flow in one direction, are denoted by arrows.

The general structure of the Geant4 based simulation program that has been developed is shown in Fig. 5.3. It follows largely the standard structure suggested in [52], consisting of a main part, which reads an input file with the settings for a particular simulation run and calls the other parts of the simulation program when needed, three mandatory parts (detector construction, physics list and primary generator action), which are required for every Geant4 based program, and three optional parts (run action, event action, tracking action), whose purpose is to allow the execution of specific actions like saving data to output files at pre-defined points in the program flow. In the following sections, each part of the simulation program will be described in detail.

5.2.1. Main part

In the main part of the program, an instance of the `G4RunManager` class is created at first. This class controls the flow of the program and manages the event loops within a run. It is also responsible for the initialization of the simulation run, thus `G4RunManager` provides methods to access the parts of the program which specify

the detector geometry and physics processes (detector construction and physics list). After the run has been initialized, the user action parts are accessed. The first one, primary generator action, is mandatory and describes the initial state of the primary particle. The other three (run action, event action, tracking action) are accessed at the beginning and at the end of the processing of each run, of each event within a run and each track within an event.

In addition to the run manager, an instance of the `G4UImanager` class is created in the main part. This class provides the user interface, which is needed to specify or change the details of the run, either via an input file passed by a command-line argument or in an interactive session, during which the user types in every command by hand. In the case of an input file, the commands contained within the file are read line-by-line and processed accordingly by passing the commands to the respective program part.

5.2.2. Detector construction

The detector construction part of the program is derived from the `G4VUserDetector-Construction` base class. Its main purpose is to define the geometries and the materials used in the simulation. For the simulation studies described here, a simple

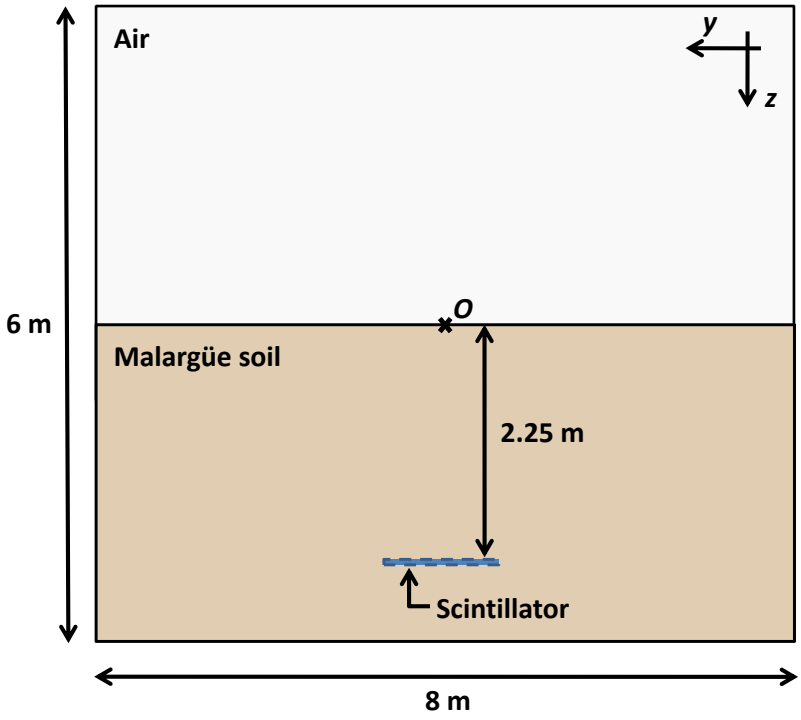

Figure 5.4: Simplified illustration of the geometry used in the simulation program; the origin of the coordinate system is denoted by O; the scintillator itself is not implemented in the program code, but it is shown in the illustration for completeness.

Mineral	Rel. abundance [%]
SiO_2	59.32
Al_2O_3	16.57
Fe_2O_3	7.08
CaO	6.56
Na_2O	4.00
MgO	3.35
K_2O	1.91
TiO_2	0.87
P_2O_5	0.21
MnO	0.13
total	100.00

Table 5.1: List of the mineral abundances in Malargüe soil as implemented in the simulation; listed are the averaged values derived from [51].

geometry has been chosen, consisting of two rectangular volumes (Fig. 5.4). The outer volume, or "world volume", defines the outer borders of the simulation. No track of a simulated particle can extend beyond this volume. Once a particle reaches these borders, the processing of its track is aborted. The dimensions of the world volume are $5\,\mathrm{m} \times 8\,\mathrm{m} \times 6\,\mathrm{m}$, centered around the origin of the rectangular coordinate system. The second volume, or "soil volume", has the dimensions $5\,\mathrm{m} \times 8\,\mathrm{m} \times 3\,\mathrm{m}$ and is placed 1.5 m below the origin. The muon counter module itself, placed at a depth of 2.25 m, is not implemented in the simulations. It is shown in Fig. 5.4 only for completeness. However, it is planned to implement the muon counter module at a later stage to expand the simulation program to a full detector simulation.

In the next step, the materials, of which the volumes consist, are defined. The world volume is filled with air, which, in a simplified model, consists of 79 % nitrogen (N_2) and 21 % oxygen (O_2) with a density of $1.29\,\mathrm{kg\ m^{-3}}$ [5]. The soil volume is filled with Malargüe soil, a mixture of several minerals. The minerals and their relative abundances are listed in Tab. 5.1. The values listed in this table are based on a geological characterization of the soil in the area where the AMIGA enhancement is located [51]. For simplicity reasons, the density of Malargüe soil has been fixed to a constant value of $2.38\,\mathrm{g\ cm^{-3}}$, not taking into account the different densities of the gravel and the sand [51], of which the real soil is comprised.

5.2.3. Physics list

In the physics list part, which is derived from the `G4VUserPhysicsList` base class, all particle types and physics processes that are to be included in the simulation are defined. For the simulation studies described in this thesis, it has, for simplicity reasons, been decided to employ a short and basic physics list, containing only basic leptons and hadrons, while omitting more exotic particles. For these particles, all

available electromagnetic processes have been enabled as well as particle decays. As an overview, the particles enabled in the simulation program and the associated physics processes are listed in Tab. 5.2. For a complete description of these processes and the their parameterizations in the Geant4 framework, see [53, 54]. Nevertheless, the physics list is modular and additional particles and processes can be easily added when needed for specific simulations. For example, for the simulations described in Section 6.2.2, hadronic interactions have been added, which are not needed for the other studies described in the thesis at hand. These additional interactions comprise elastic and inelastic processes based on different hadronic models for different energy ranges.

Particle	**Geant4 class**	**Associated process classes**
e^-	G4Electron	G4eMultipleScattering
		G4eIonisation
		G4eBremsstrahlung
e^+	G4Positron	G4eMultipleScattering
		G4eIonisation
		G4eBremsstrahlung
		G4eplusAnnihilation
μ^-	G4MuonMinus	G4MuMultipleScattering
		G4MuIonisation
		G4MuBremsstrahlung
		G4MuPairProduction
		G4Decay
μ^+	G4MuonPlus	G4MuMultipleScattering
		G4MuIonisation
		G4MuBremsstrahlung
		G4MuPairProduction
		G4Decay
ν_e	G4NeutrinoE	-
$\bar{\nu}_e$	G4AntiNeutrinoE	-
ν_μ	G4NeutrinoMu	-
$\bar{\nu}_\mu$	G4AntiNeutrinoMu	-
π^+	G4PionPlus	G4hMultipleScattering
		G4hIonisation
		G4hBremsstrahlung
		G4hPairProduction
		G4Decay
		[G4PionPlusInelasticProcess]
		[G4PionPlusElasticProcess]
π^-	G4PionMinus	G4hMultipleScattering
		G4hIonisation
		G4hBremsstrahlung

		G4hPairProduction
		G4Decay
		[G4PionMinusInelasticProcess]
		[G4PionMinusElasticProcess]
π^0	G4PionZero	G4Decay
p	G4Proton	G4hMultipleScattering
		G4hIonisation
		G4hBremsstrahlung
		G4hPairProduction
		[G4ProtonInelasticProcess]
		[G4ProtonElasticProcess]
n	G4Neutron	G4Decay
		[G4NeutronInelasticProcess]
		[G4NeutronElasticProcess]
γ	G4Gamma	G4PhotoElectricEffect
		G4ComptonScattering
		G4GammaConversion
Ions	G4GenericIon	G4hMultipleScattering
		G4ionIonisation
		[G4ionInelasticProcess]
		[G4ionElasticProcess]

Table 5.2: List of the particle types implemented in the simulation program, the according Geant4 classes and the interaction process classes associated to these particle types; processes that have been enabled only for the studies described in Section 6.2.2 are denoted by brackets; for a detailed description of the classes, see [53]; for a detailed description of the parametrization of the physics processes provided by the Geant4 toolkit, see [54].

5.2.4. Primary generator action

In the primary generator action part of the simulation, the properties of the primary particles are defined. This part is derived from the `G4VUserPrimaryGeneratorAction` base class. The properties of the primary particle can either be hard-coded in the program code or set via an input file when executing the program. The necessary subroutines are automatically initialized and registered at the run manager, so that the run manager can pass the corresponding commands from the input file to the primary generator part, where the properties of the primary particle are then set accordingly.

The properties set in this way are the particle type, the kinetic energy (in eV), the direction of the momentum vector and the emission point, where the primary

particle is created in the simulation. The particle type is, in the scope of the Geant4 toolkit, determined by an integer number that corresponds to the encoding used by the Particle Data Group (PDG) [5]. The PDG encodings of several common particles are listed in Tab. 5.3.

Particle	**PDG encoding**
e^-	11
ν_e	12
μ^-	13
ν_μ	14
γ	22
p	2112
n	2112
π^+	211

Table 5.3: List of the PDG encoding of several particles [5]; antiparticles are denoted by the correspoding negative integer number;.

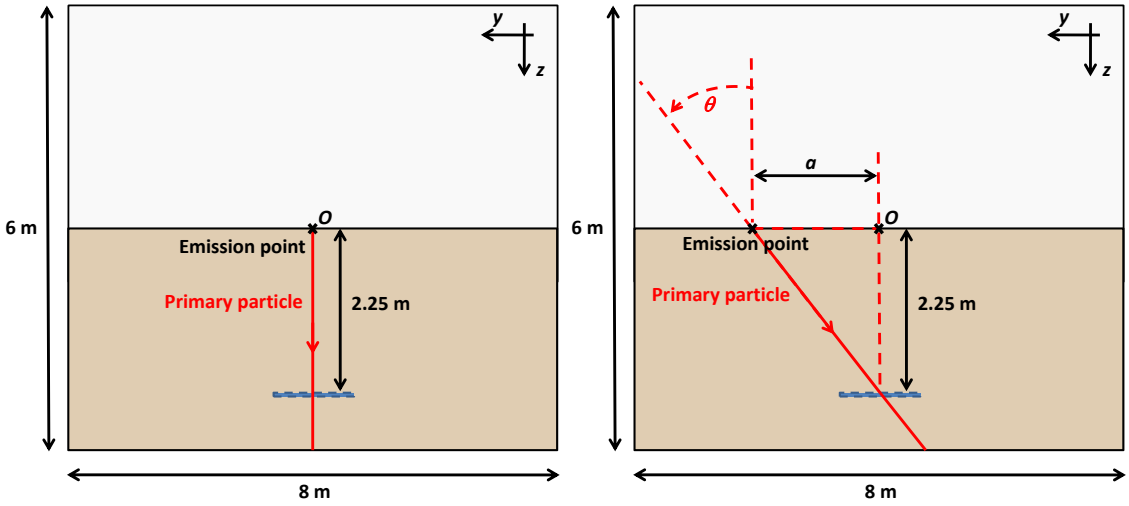

Figure 5.5: Schematic depiction of the relation between the incoming direction of the primary particle and the location of the emission point for (a) vertical and (b) inclined primary particles; for inclined primary particles ($\theta > 0°$), the emission point of the primary particle is shifted in y-direction to ensure that the particle traverses the scintillator plane at a depth of 2.25 m always in the center.

The direction of the momentum vector of the primary particle and the location of the emission point are determined by the zenith angle θ set in the input file. The corresponding azimuth angle is fixed to 90°, so that the incoming direction of the primary particle is always perpendicular to the scintillator strips. In Fig. 5.5, the relation between the incoming direction of the primary particle, the location of the emission point and the zenith angle θ is shown. For vertical particles ($\theta = 0°$), the emission point coincides with the origin of the coordinate system (see Fig. 5.5(a)). For inclined particles , the emission point is shifted from the origin of the coordinate system along the y-axis by

$$a = 2.25\,\mathrm{m} \times \tan(\theta), \tag{5.1}$$

so that the primary particle always traverses the center of the scintillator plane at a depth of 2.25 m (see Fig. 5.5(b)). This shift has been introduced to ensure that all particles that could be produced along the primary particles track are contained within the world volume and are not subject to the border effects described previously. The dimensions of the world volume (see Section 5.2.2) have been chosen such that this is the case for zenith angles up to 60°.

5.2.5. User action parts

In this section, the three optional user action parts (run action, event action and tracking action) will be described briefly. These parts are derived from the `G4UserRunAction`, `G4UserEventAction` and `G4UserTrackingAction` base classes and provide the possibility to execute customized actions that are not part of the standard Geant4 program flow. For the simulations described in this thesis, these customized actions include the setting of additional parameters for a given simulation run and writing the simulation results to output files. The additional parameters encompass the internal number of the first event simulated, so that a large simulation run can be divided into several smaller runs while, at the same time, retaining the consecutive numbering of events and the setting of the random seed for the simulation run. This seed is also written to an output file for each event to allow a re-run of a specific event in the case a data file is corrupted or a further analysis of this event is needed.

For each event in a simulation run, an output file is generated, where the simulation results are stored as binary data. In particular, for each particle (or track) that is simulated during an event, its type (in PDG encoding), the internal track number, the track number of the parent particle (for secondary particles) as well as the kinetic energy and the x, y and z coordinates at the beginning and at the end of the track are stored in the output file.

6. Determination of energy thresholds

In the following chapter, energy thresholds for several particle types will be determined with the help of the simulation program described in the previous chapter. These thresholds can be understood as the minimum kinetic energy a particle originating from an extensive air shower needs in order to pass the 2.25 m of Malargüe soil and produce a signal in the AMIGA detector. The knowledge of these energy thresholds is important for a basic understanding of the detector with respect to the data analysis, but it is also useful from at least two other points of view: on the one hand, the thresholds can be used to optimize AMIGA specific simulation studies, for example with CORSIKA. On the other hand, the energy thresholds can serve as a cross check to test the simulation program itself, since they are, at least in the muon case, well calculable via the Bethe-Bloch formula. Large deviations from the theoretical expectation would point to, for example, missing processes in the physics list part or other problems within the simulation program.

The energy thresholds have been determined for muons, electrons, photons, protons, neutrons and negatively charged pions, since these are the most common particles from extensive air showers at ground level (see Section 2.3). However, the simulation and analysis programs have been designed in a modular way so that the energy thresholds for other particles can be easily determined when needed.

The simulated data has been analyzed using the ROOT toolkit, an object-oriented, `C++` based framework for data analysis [55]. All fits shown in the following chapters have been performed using the Minuit function minimization program as implemented in the ROOT framework [56]. In the following, the function parameters that are to be fitted are denoted by p_0, p_1, p_2 etc.

6.1. Muons

To determine the energy threshold for muons, 50 000 events with vertical muons have been simulated each for 34 kinetic energies between 10 MeV and 1300 MeV. For each event, the penetration depth of the primary muon has been calculated using the z-coordinates of the endpoints of the respective muon track. It has to be noted that this may introduce a bias when dealing with non-linear (curved) tracks, because this calculation may underestimate the real penetration depth in this case. However, since the tracks of the particles studied in the present thesis can always be approximated by a straight line, this bias can be neglected.

In Fig. 6.1, the histograms of the penetration depths of the primary muons are depicted for two energies (100 MeV and 1000 MeV). Both histograms show the expected shape, with an asymmetry toward lower penetration depths, due to the Landau distribution of the energy loss. To determine the energy threshold from these

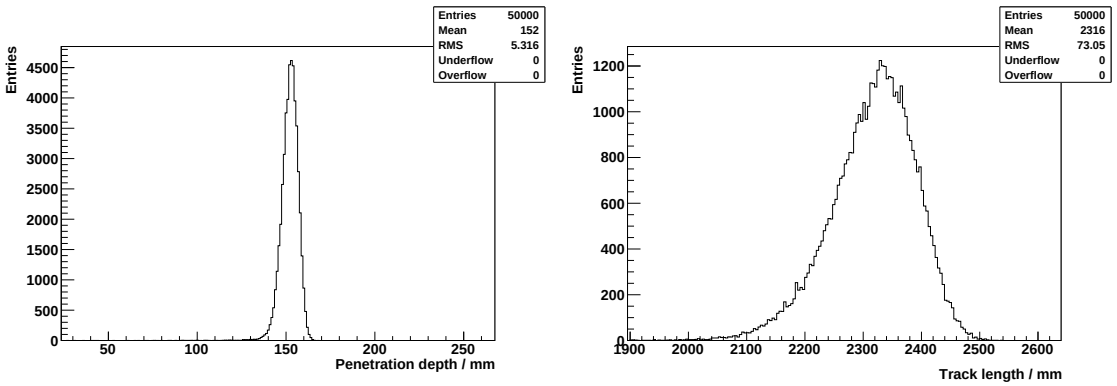

(a) (b)

Figure 6.1: Histogram of the penetration depths for muons with (a) 100 MeV and (b) 1000 MeV kinetic energy; each histogram is based on the analysis of 50 000 events.

histograms, two different methods have been employed: for the first method, a Gaussian bell curve of the form

$$y(x) = p_0 \; e^{-\frac{(x-p_1)^2}{2p_2^2}} \tag{6.1}$$

has been fitted to the peak of the distribution of the penetration depths to obtain the most probable value. For the second method, the 0.95-quantile of the distribution has been calculated, which is the value of the penetration depth for which 95 % of all events exhibit a smaller value. In Fig. 6.2, both parameters have been plotted against the kinetic energy of the primary muon. In the case of the most probable penetration depth, the uncertainty plotted is the uncertainty of the fit result. In the case of the 0.95-quantile, the uncertainty is based on the statistical uncertainties of the histogram bins that were used to calculate the 0.95-quantile. Both parameters show a linear dependance on the kinetic energy of the primary muon in the energy region above 100 MeV, while in the region below 100 MeV the dependance is rather quadratic. For the purpose of understanding the AMIGA muon counter, only the depth region around 2.25 m is relevant, thus, a linear function of the form

$$y(x) = p_0 \; + \; p_1 \; x \tag{6.2}$$

has been fitted to both sets of data points in the energy region from 500 MeV to 1250 MeV. The detailed results of these fits are listed in App. A.1. From the inverse functions of the fitted curves, the energy thresholds for both methods have been obtained:

$$E_{\mathrm{thr},1} \;=\; (965.6 \pm 0.3)\ \mathrm{MeV}, \tag{6.3}$$

$$E_{\mathrm{thr},2} \;=\; (932.4 \pm 0.6)\ \mathrm{MeV}, \tag{6.4}$$

where the threshold corresponds to a depth of 2.25 m in both cases. The exact functions that have been used to calculate the thresholds and the uncertainties are

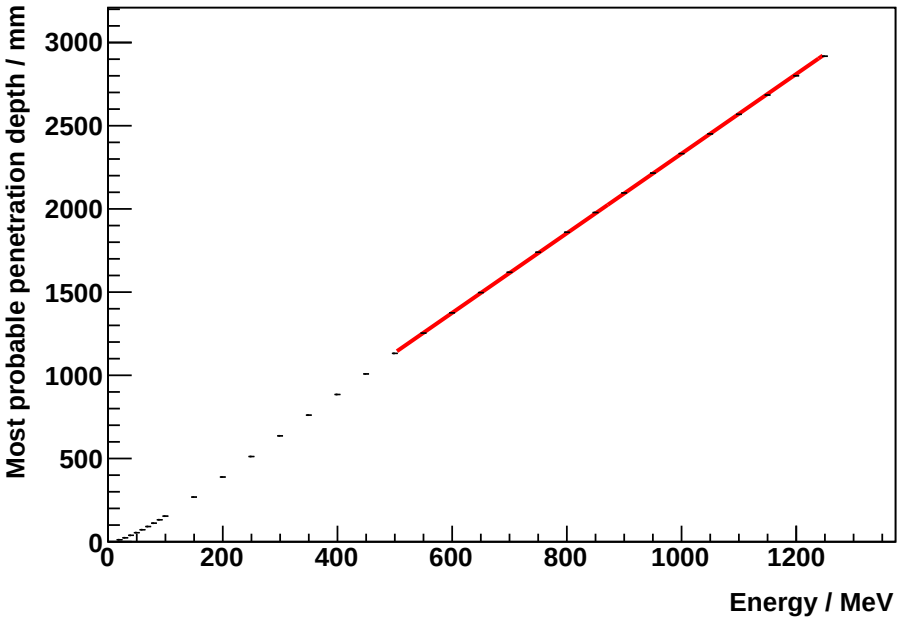

(a)

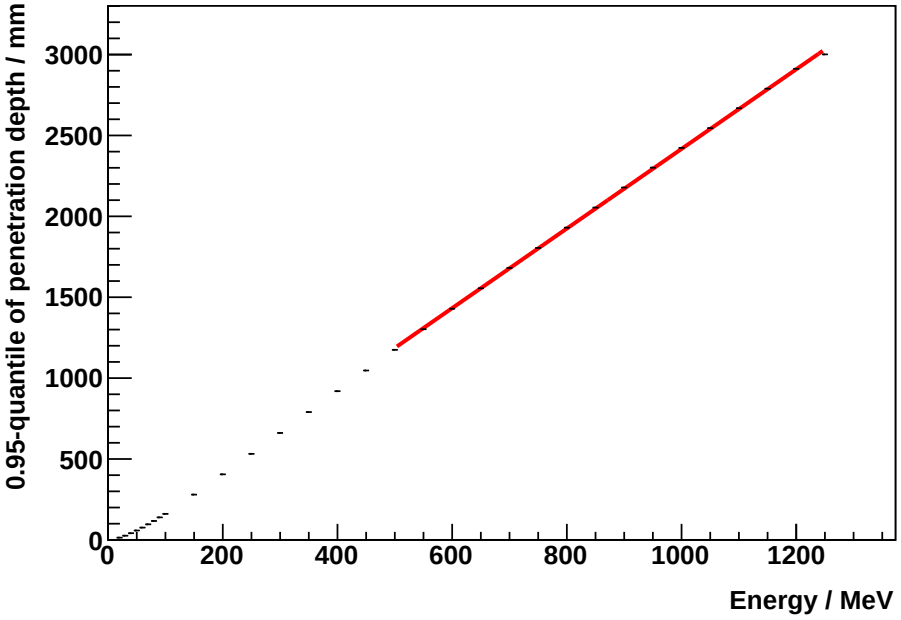

(b)

Figure 6.2: (a) Most probable penetration depth vs. the kinetic energy of the primary muon; (b) 0.95-quantile of the penetration depth vs. the kinetic energy of the primary muon.

listed in App. A.1 to allow for a direct determination of the thresholds for other depths from the fit results, if needed. As expected, the energy threshold determined through the second method is lower than the one obtained by the first method, since the 0.95-quantile is always larger than the most probable penetration depth. The slightly larger uncertainty is expected as well. The uncertainties of the fit, from which the most probable penetration depth is determined, are comparatively small because of the high statistics, whereas the 0.95-quantile is calculated from a region of the histogram with less statistics, leading to larger uncertainties.

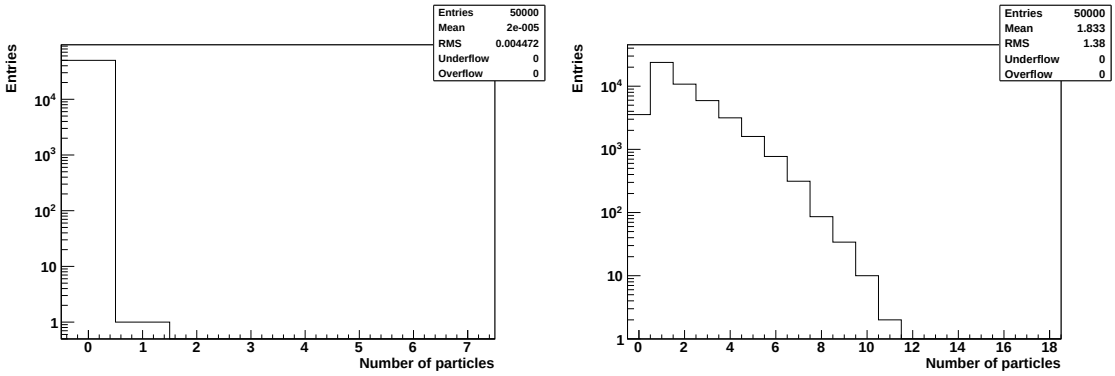

(a) (b)

Figure 6.3: Histogram of the number of particles in a depth of 2.25 m for muons with (a) 100 MeV and (b) 1000 MeV kinetic energy; each histogram is based on the analysis of 50 000 events.

However, both methods described in the previous paragraphs are only taking the primary muon into account. Since this muon may produce secondary particles in the soil above the detector, the possibility that these particles may likewise produce a signal in the detector has to be considered as well when determining energy thresholds. In Fig. 6.3, the histograms of the number of particles (primary and secondary) in a depth of 2.25 m are shown again for two primary energies (100 MeV and 1000 MeV). To avoid overcounting of particles, only particles which can produce a signal in the detector (i.e. muons, electrons and photons, but not e.g. neutrinos) above a certain energy threshold are considered. This threshold has been set to 100 keV, which is approximately the minimum energy needed to produce a single photo-electron in the cathode of the PMT [57]. From the histograms, the fraction of events with no particles at all in a depth of 2.25 m is calculated. In the 100 MeV case (Fig. 6.3(a)), this fraction is almost 100 %, since the primary muon is generally absorbed in the soil above the detector and the neutrinos from the muon decay are discarded by the particle cut. In the 1000 MeV case (Fig. 6.3(b)), this fraction decreases considerably. This energy is above the threshold obtained previously. Thus, in most events, the primary muon will reach the detector, reducing the fraction of events with no particles at all in this depth.

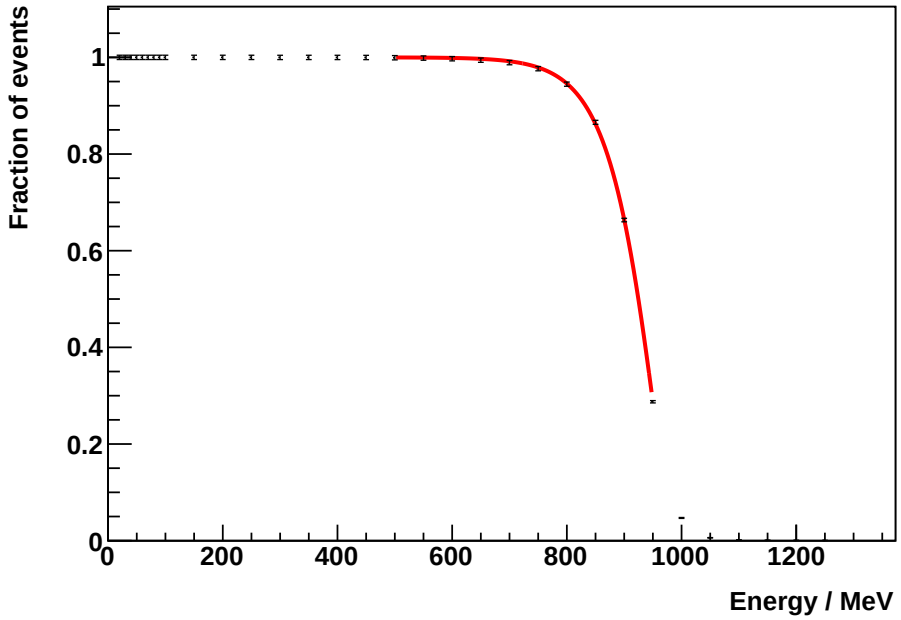

Figure 6.4: Fraction of events with no particles at all in a depth of 2.25 m vs. the kinetic energy of the primary muon.

In Fig. 6.4, the fraction of events with no particles in a depth of 2.25 m is plotted against the kinetic energy of the primary muon. The uncertainties of each datapoint have been determined from the statistical fluctuations of the bin contents in the underlying histograms. To obtain the energy threshold from Fig. 6.4, a sigmoid function of the form

$$y(x) = \frac{1}{\left(1 \ + \ p_0 \ e^{p_1(x+p_2)}\right)^{1/p_3}} \tag{6.5}$$

has been fitted to the data points in the energy region from 500 MeV to 950 MeV. This function is not motivated by any physical law, but has been chosen because it describes the data in the interesting region around a fraction of 1 down to 0.9 very well. Furthermore, this function is invertible. The fitting range has been chosen such that the fitted curve represents the datapoints best without obvious deviations. From the inverse function of the fitted curve, the energy threshold for the third method has been calculated:

$$E_{\mathrm{thr},3} \quad = \quad (800 \pm 20) \ \mathrm{MeV}, \tag{6.6}$$

where the threshold corresponds to a fraction of 95 %. Again, the detailed description of the calculation of the threshold can be found in App. A.1. The energy threshold obtained in this way is considerably smaller than the thresholds determined by the other two methods. This is expected, since all secondary particles produced in the soil above the detector are taken into account and not only the primary muon, which implies a stricter criterion for an energy threshold.

6.1.1. Comparison with the theoretical expectation

In the following section, the calculated energy thresholds shall be validated by comparing the simulation results described previously with the theoretical expectation. For muons, the prevailing sources of energy loss, when traversing a medium, are ionization and excitation, which are approximately described by the Bethe-Bloch formula [58, 18]:

$$-\frac{\mathrm{d}E}{\mathrm{d}x} = \frac{4\pi n z}{m_e c^2 \beta^2}\left(\frac{e^2}{4\pi\epsilon_0}\right)^2\left[\ln\left(\frac{2m_e c^2\beta^2}{I\cdot(1-\beta^2)}\right)-\beta^2\right], \tag{6.7}$$

where

- $\beta = \frac{v}{c}$ ratio of the velocity v of the ionizing particle (in this case the muon) and the speed of light c,
- n electron density of the traversed medium, described by $n = \frac{N_A Z \varrho}{A}$ with N_A: Avogadro constant; ϱ: density of the medium; Z and A: atomic and mass number of the medium,
- z charge number of the ionizing particle,
- m_e rest mass of the electron,
- I mean excitation potential of the medium, for $Z > 1$ approximately described by $I = Z^{0,9} \times (16\ \mathrm{eV})$.

From the Bethe-Bloch formula, the expected penetration depth R can be approximated by using

$$R(T_0) = \int_{T_0}^{0} \frac{1}{dE/dx}\, dT, \tag{6.8}$$

where T_0 denotes the kinetic energy of the ionizing particle before entering the medium. With the parameters of Malargüe soil from Tab. 5.1, Eqs. (6.7) and (6.8) yield

$$R(100\,\mathrm{MeV}) \approx 160\,\mathrm{mm}, \tag{6.9}$$
$$R(1000\,\mathrm{MeV}) \approx 2240\,\mathrm{mm}. \tag{6.10}$$

These values are within the same order of magnitude as the simulation results (Fig. 6.1). However, a more detailed comparison is not possible, since the Bethe-Bloch formula is, especially at very low energies and in the form given by Eq. (6.7), only an approximation without any correction factors. Nevertheless, this is sufficient to confirm that the simulation program is working as intended. Missing processes in the physics list would affect the simulation results by at least one order of magnitude [52]. Hence, it can be concluded that the short physics list is sufficient for the simulation studies.

6.1.2. Comparison with antimuons

The energy thresholds for antimuons have been determined in the same way as the energy thresholds for muons, described in the previous sections. The results for antimuons can serve as a further test of the simulation program, since these results should be in agreement with the thresholds obtained for their negatively charged counterparts. Minor deviations are only expected when calculating the energy threshold from the number of particles in a depth of 2.25 m, since antimuons decay into positrons. These positrons may annihilate in the soil and thus produce photons with an energy in the order of magnitude of 100 keV, which is larger than the average energy of photons produced by electrons traversing the soil. This may lead to a slighty lower threshold for antimuons.

In Fig. 6.5, the most probable penetration depth, the 0.95-quantile of the penetration depth and the fraction of events with no particles at all in a depth of 2.25 m are plotted against the kinetic energy of the primary antimuons. As in the muon case, 50 000 events with vertical antimuons have been simulated each for 34 energies between 10 MeV and 1300 MeV. From these plots, the following energy thresholds have been determined (see App. A.2):

$$E_{\mathrm{thr},1} = (965.6 \pm 0.3)\ \mathrm{MeV}, \tag{6.11}$$

$$E_{\mathrm{thr},2} = (932.2 \pm 0.6)\ \mathrm{MeV}, \tag{6.12}$$

$$E_{\mathrm{thr},3} = (800 \pm 10)\ \mathrm{MeV}. \tag{6.13}$$

These thresholds are in good agreement with the thresholds calculated for muons. Thus, it can be safely concluded that the simulation program works as intended and the results obtained from these simulations are reliable.

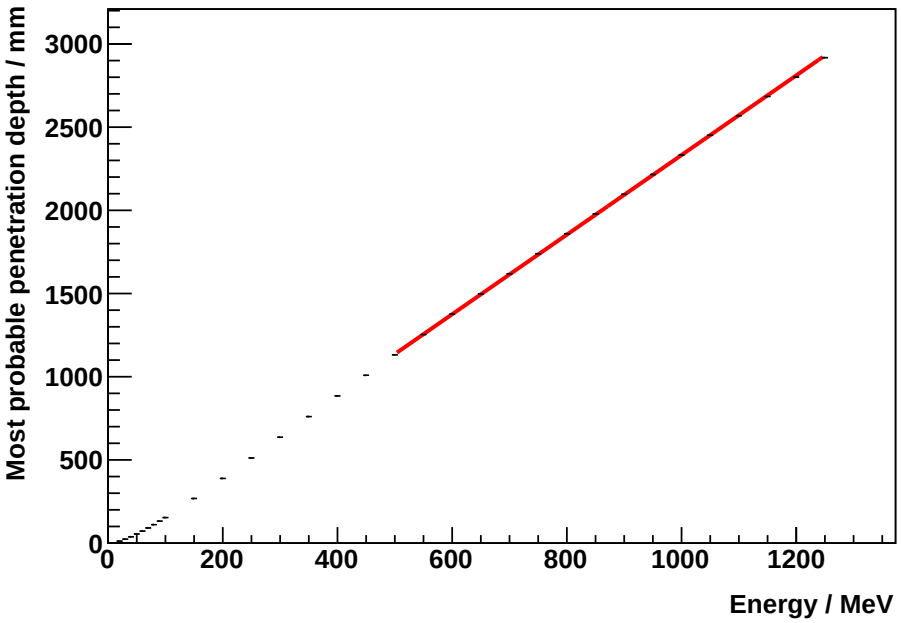

(a)

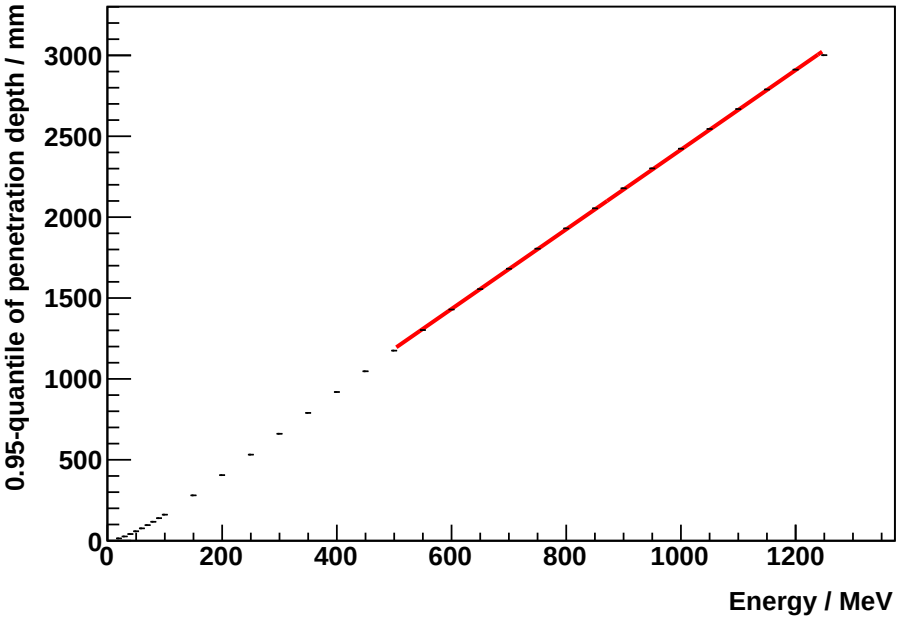

(b)

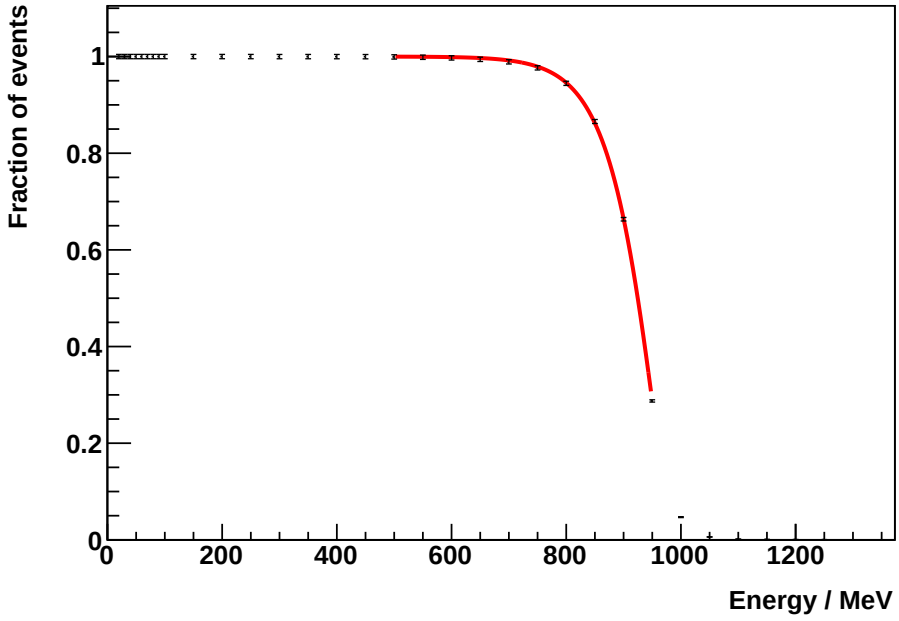

(c)

Figure 6.5: (a) Most probable penetration depth vs. the kinetic energy of the primary antimuon; (b) 0.95-quantile of the penetration depth vs. the kinetic energy of the primary antimuon; (c) fraction of events with no particles at all in a depth of 2.25 m vs. the kinetic energy of the primary antimuon.

6.2. Other particles

Muons only account for about 80 % of the particles from extensive air showers at ground level (see Chapter 2.3). The remaining 20 % encompass electrons and photons as well as hadrons, mostly protons, neutrons and pions. These particles may, just like muons, traverse the soil above the detector and produce a signal in the AMIGA detector. Thus, it is important to know the energy thresholds for these particles as well in order to interpret the recorded data and correctly reconstruct the number of muons from the data.

Generally, the energy thresholds presented in the following sections have been determined in the same way as described in the previous section for muons, although only the third method is used here. This method takes all secondary particles that are produced in the soil above the detector independent of the type of the primary particle into account and hence provides the most reliable estimation of the energy threshold. For each particle type, the histogram of the penetration depth will be quoted only for a reference energy of 1000 MeV to allow for a comparison with the respective histograms for muons shown before.

6.2.1. Electrons and photons

For electrons and photons, 21 kinetic energies, ranging from 1 MeV to 100 GeV have been simulated. For these particles, only 5 000 events have been accumulated for each energy because of limitations regarding disk space and computing time available on the local computing cluster that has been used for the simulation studies. Nevertheless, the level of precision reached with this number of events is sufficient for the purpose of this thesis.

In Fig. 6.6(a), the distribution of the penetration depth is shown for primary photons at an energy of 1000 MeV. The interaction processes that photons undergo when traversing matter are completely different from those of the other particles described in this chapter. Thus, the histogram exhibits an exponential shape without a clear peak. As for muons, the fraction of events with no particles at all in a depth of 2.25 m has been calculated and plotted versus the energy of the primary photon (Fig. 6.7(a)). Again, a sigmoid function following Eq. (6.5) has been fitted to the data in the energy region from 100 MeV to 10 GeV. The calculation of the energy threshold from the fit yields (see App. A.3):

$$E_{\mathrm{thr},\gamma} \;=\; (1600 \pm 200)\ \mathrm{MeV}. \tag{6.14}$$

The relative uncertainty is 12.5 % and thus larger than in the muon case (2.5 %),

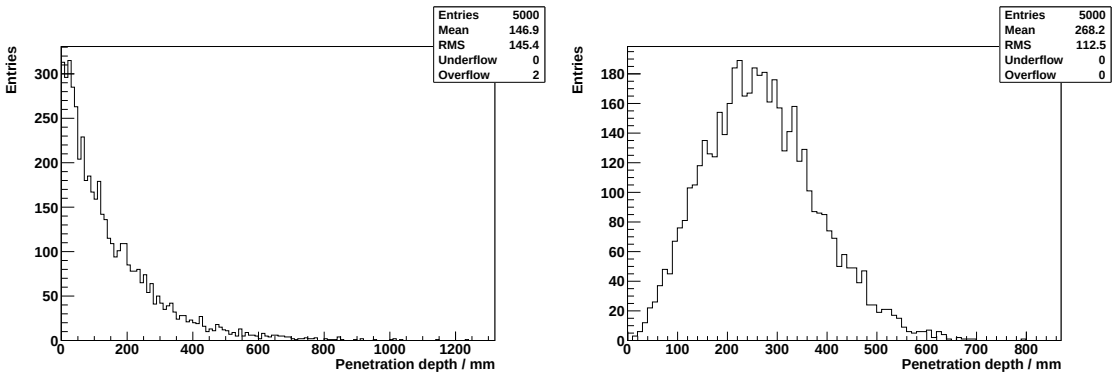

(a) (b)

Figure 6.6: Histogram of the penetration depths for (a) photons and (b) electrons, both at an energy of 1000 MeV; each histogram is based on the analysis of 5 000 events each.

due to the smaller number of simulated events.

In the electron case (Figs. 6.6(b) and 6.7(b)), the histogram of the penetration depths is more similar to the muon case than the histogram for photons. The differences between the electron and the muon histograms are due to the differences in the dominating source of energy loss for both particle types when traversing matter. In the electron case, the dominating source of energy loss is bremsstrahlung, which for muons becomes relevant for energies above some 100 GeV only.

The energy threshold for electrons has been determined from Fig. 6.7(b) in the same way as for photons. As before, the fit has been limited to the energy range from 100 MeV to 10 GeV. The calculation (see App. A.4) results in an energy threshold of

$$E_{\mathrm{thr},e} \quad = \quad (2100 \pm 300)\ \mathrm{MeV}. \tag{6.15}$$

Again, the relative uncertainty is above 10 %, due to the comparatively small dataset that has been used for the analysis. Still, this level of precision is sufficient for the purpose of a first understanding of the detector. It also suffices to provide rough estimates of the thresholds as a starting point for further simulations.

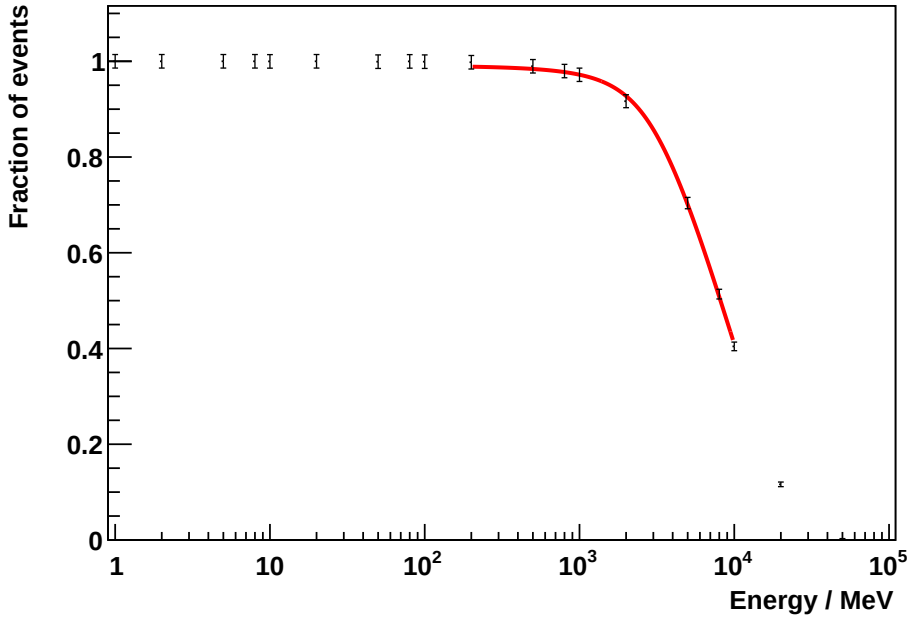

(a)

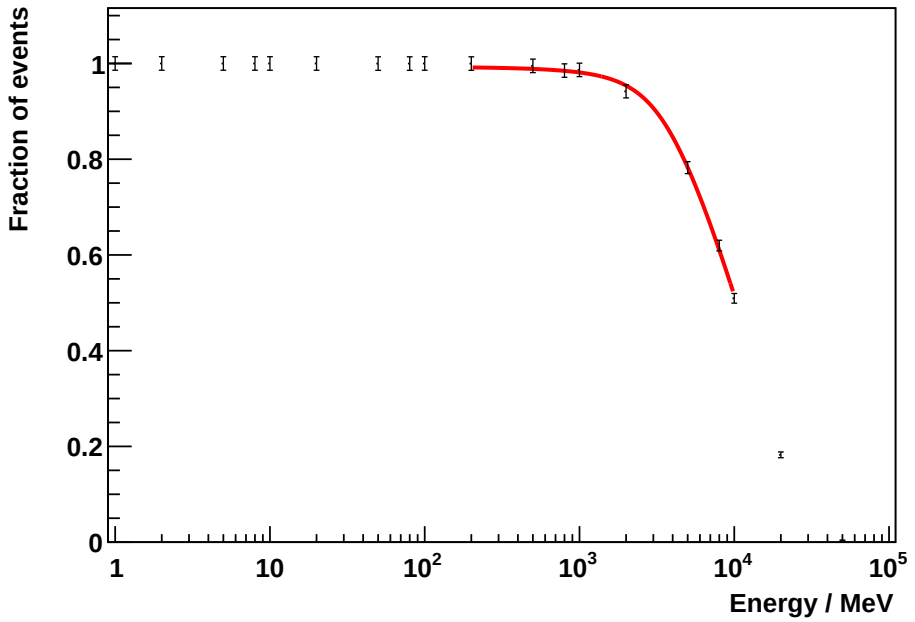

(b)

Figure 6.7: Fraction of events with no particles at all in a depth of 2.25 m vs. the energy of the primary particle for (a) photons and (b) electrons.

6.2.2. Hadrons

At ground level, the hadronic particles from extensive air showers comprise mostly protons, neutrons and pions. When these particles traverse the soil, they interact with the constituents of the soil not only via the electromagnetic force, ionizing and exciting the atoms in the soil, but also via the strong force, for example by initiating a hadronic cascade (see Section 2.3.1). Thus, an extended physics list is needed when determining the energy thresholds for hadronic particles in order to account for these interactions and to avoid a bias because of missing processes in the physics list (see Section 5.2.3).

With the extended physics list, 10 000 events have been simulated each for protons, neutrons and negatively charged pions and each for 19 energies between 100 MeV and 10 GeV, . The proton case is shown in Figs. 6.8(a) and 6.8(a). In the histogram of the penetration depths (Fig. 6.8(a)), the additional hadronic interactions lead to

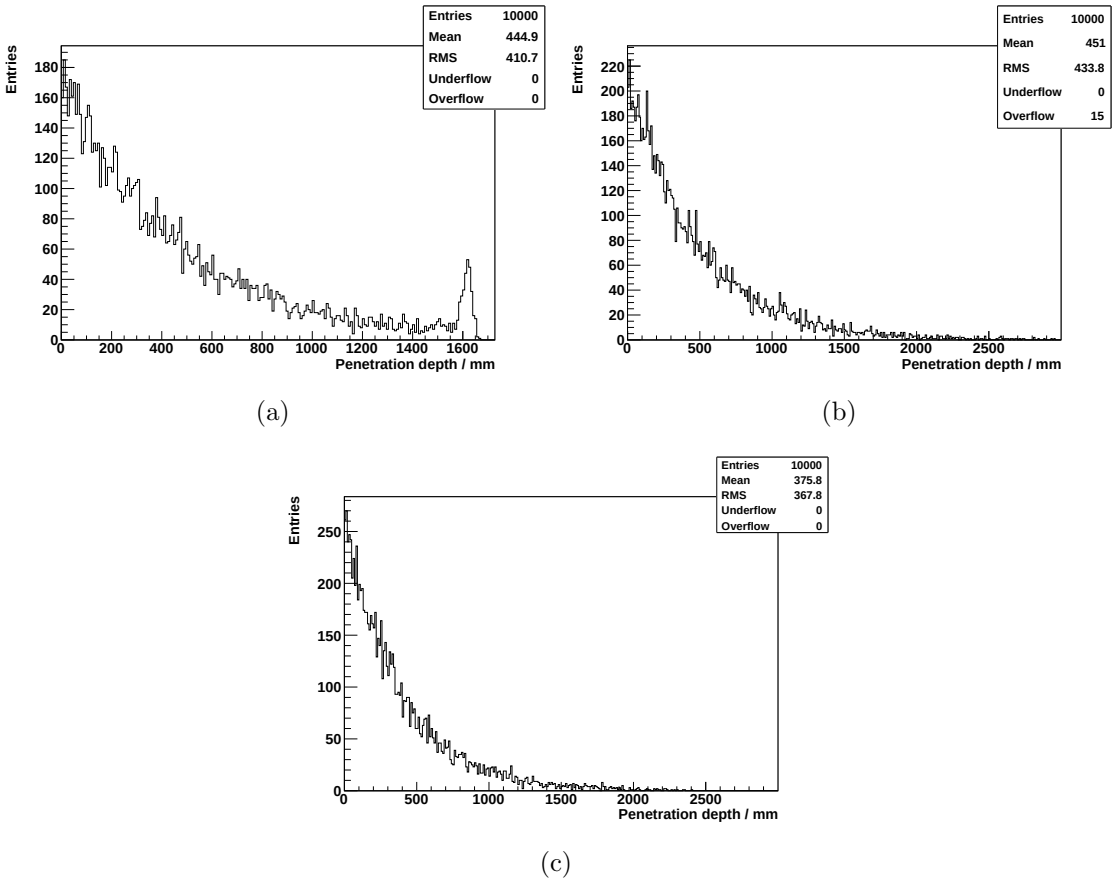

Figure 6.8: Histogram of the penetration depths for (a) protons, (b) neutrons and (c) negatively charged pions, each at a kinetic energy of 1000 MeV; each histogram is based on the analysis of 5 000 events.

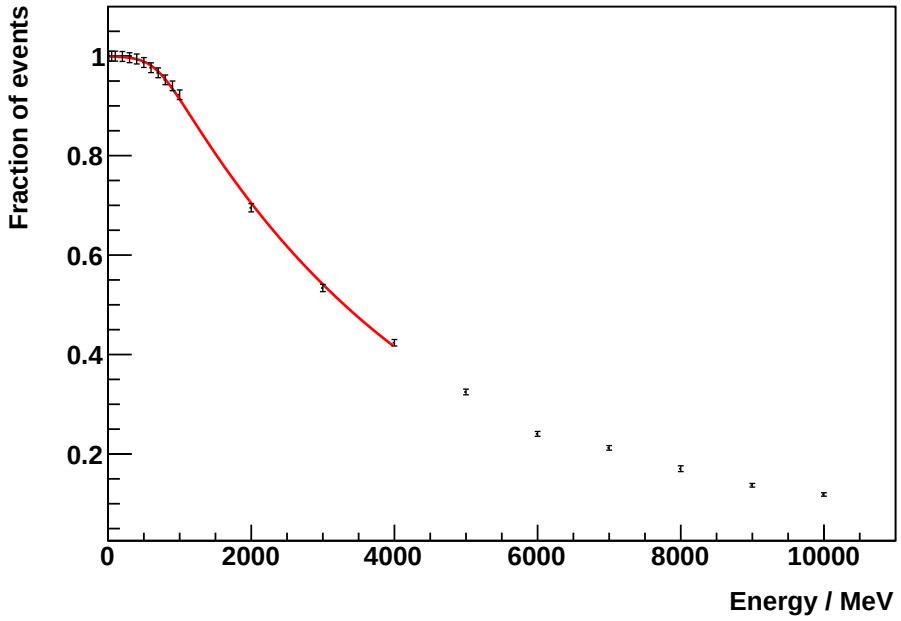
Fraction of events
1
0.8
0.6
0.4
0.2
0
2000
4000
6000
8000
10000
Energy / MeV

(a)

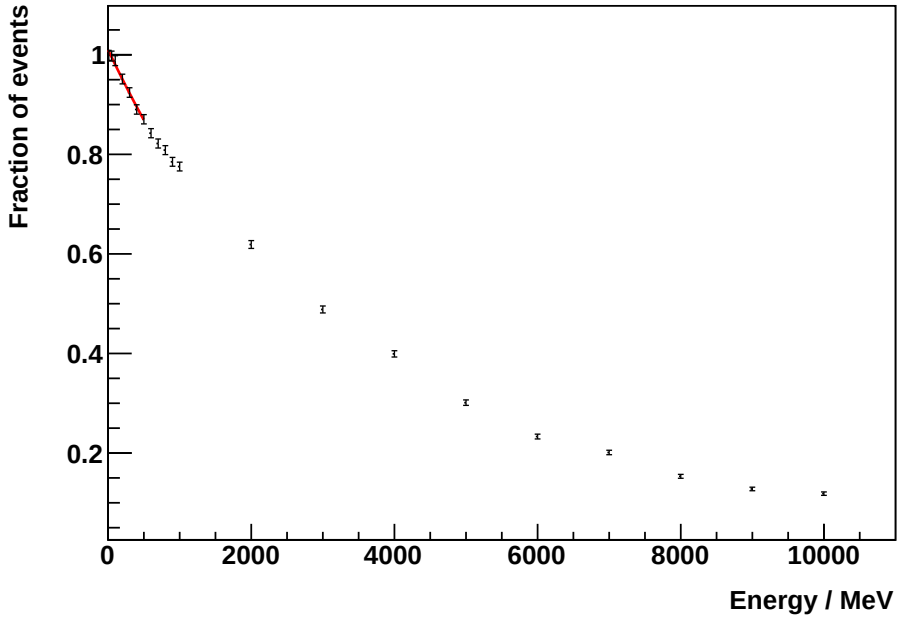
Fraction of events
1
0.8
0.6
0.4
0.2
0
2000
4000
6000
8000
10000
Energy / MeV

(b)

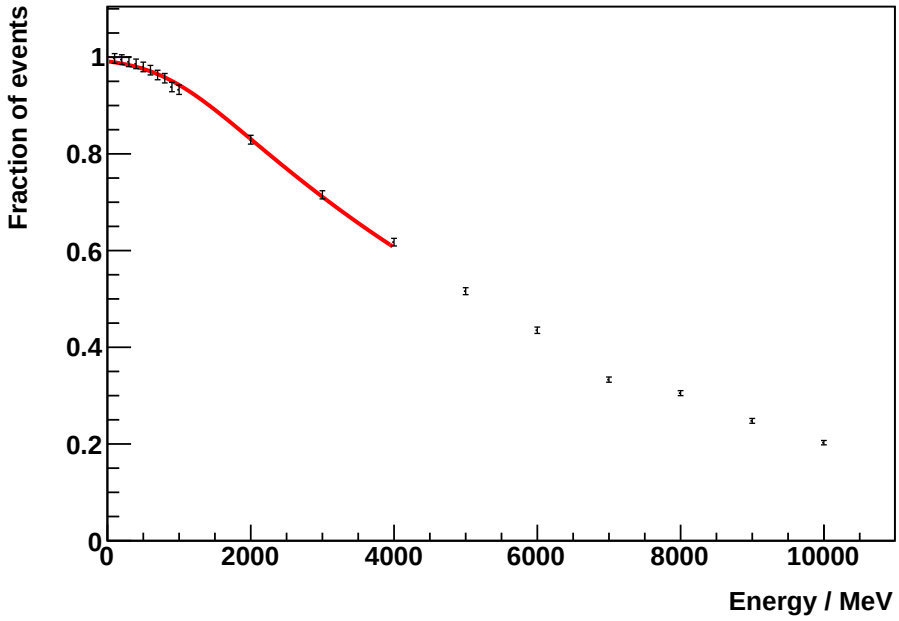

(c)

Figure 6.8: Fraction of events with no particles at all in a depth of 2.25 m vs. the energy of the primary particle for (a) protons, (b) neutrons and (c) negatively charged pions.

an exponential shape. The peak around 1600 mm is due to ionization and excitation, since protons are charged particles and thus undergo electromagnetic interactions with the constituents of the soil as well, although they are suppressed with regard to hadronic interactions [59]. The location of this peak is consistent with the expectation from the Bethe-Bloch formula.

The distribution of the fraction of events with no particles at all in 2.25 m depth versus the kinetic energy of the proton (Fig. 6.8(a)) has a much broader and asymmetric shape than in the muon case. In addition, the plateau at lower energies is much less pronounced. Nevertheless, the data points can still be described by Eq. (6.5) in the energy region from 100 MeV to 4 000 MeV. The calculation of the energy threshold from the fit (see App. A.5) yields

$$E_{\mathrm{thr},p} \quad = \quad (820 \pm 50)\ \mathrm{MeV}. \tag{6.16}$$

The simulation results for neutrons are depicted in Figs. 6.8(b) and 6.8(b). In comparison to the proton case, the peak due to ionization and excitation is missing in Fig. 6.8(b), since neutrons are uncharged particles. The exponential shape due to hadronic interactions, however, remains the same. For neutrons, the determination

of the energy threshold from the fraction of events with no particles at all in 2.25 m depth versus the kinetic energy of the primary neutrons (Fig. 6.8(b)) turns out to be more difficult: the fit of a sigmoid function fails in this case, since the shape is even more asymmetric than in the proton case and the plateau at lower energies completely vanishes. Thus, in the neutron case, an exponential function following

$$y(x) = p_0 \; e^{p_1 x} \tag{6.17}$$

has been fitted to the data. This function describes the datapoints better in the interesting region between 100 MeV to 1 000 MeV. From the inverse function of the fitted curve, the energy threshold for neutrons has been calculated (see App. A.6):

$$E_{\mathrm{thr},n} \;=\; (200 \pm 20) \text{ MeV}. \tag{6.18}$$

The simulation results for negatively charged pions are shown in Figs. 6.8(c) and 6.8(c). In the histogram of the penetration depths (Fig. 6.8(c)), the peak due to ionization and excitation, which would be expected around 2300 mm, is not visible due to the small statistics in this depth range. Regarding the fraction of events with no particles at all in 2.25 m depth versus the kinetic energy of the proton (Fig. 6.8(c)), a sigmoid function following Eq. (6.5) has, as in the proton case, been fitted to the data points in the energy region from 100 MeV to 4 000 MeV. The calculation of the energy threshold from the fit yields:

$$E_{\mathrm{thr},\pi} \;=\; (860 \pm 80) \text{ MeV}. \tag{6.19}$$

The detailed results of the fit as well as the functions used to obtain the threshold and its uncertainty are listed in App. A.7.

6.3. Interpretation of the results

In the following section, the chapter on the determination of energy thresholds from simulations will be concluded by summarizing the thresholds and comparing them to a typical extensive air shower. In Tab. 6.2, the results of the calculations of the energy thresholds for the different particle types are listed.

To put these values into perspective, a typical extensive air shower, induced by a proton at an energy of $10^{18.5}$ eV, has been simulated with CORSIKA [60]. In Fig. 6.9 the energy distributions of different particle types on ground level are shown. To save processing time and disk space, an energy cut has been applied, thus the distributions for muons (including antimuons) and hadrons begin at 100 MeV, while

Particle type	Energy threshold [MeV]
Muon	800 ± 20
Antimuon	800 ± 10
Photon	1600 ± 200
Electron	2100 ± 300
Proton	820 ± 50
Neutron	200 ± 20
Pion	860 ± 80

Table 6.2: Summary of the energy thresholds determined in the previous sections; for muons and antimuons, only the thresholds obtained by the third method are quoted.

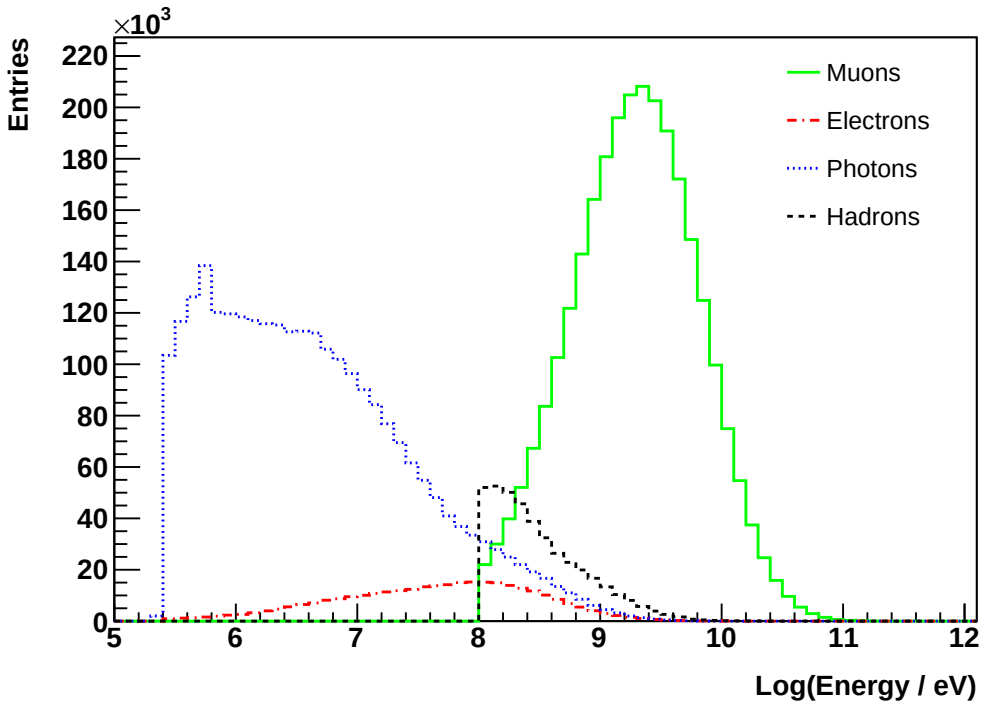

Figure 6.9: Energy distribution of different particle types on ground level from a single, proton-induced extensive air shower at $10^{18.5}$ eV [60]; the shower has been simulated with CORSIKA; an energy cut has been applied for muons and hadrons at 100 MeV and for electrons and photons at 0.25 MeV.

the distributions for electrons (including positrons) and photons begin at 0.25 MeV. Comparing the thresholds to the energy distributions, it can be seen that almost all electrons and photons have an energy below the respective threshold and are thus absorbed in the soil above the AMIGA detector. For hadrons, the situation is

slightly different: here, a significant part of the particles exhibits an energy above the threshold, especially when taking the very low threshold for neutrons into account. However, the actual contribution of hadrons to the recorded data is assumed to be negligible, since the hadronic component of an extensive air shower is limited to the area very close to the shower core (see Section 2.3.1). In this region, a very large number of muons is expected as well, thus, the data recorded from an air shower event with the shower core near the detector will still be dominated by muons.

Regarding muons, about one fourth of all muons (and antimuons) on ground level has an energy below the threshold and hence cannot be detected by the AMIGA muon counter. Still, the remaining number of muons with an energy above the threshold will allow for a reconstruction of the number of muons inside the recorded extensive air shower with sufficient precision to study the composition of primary cosmic rays (see Section 4.1.1).

The energy thresholds discussed in this chapter can be used as a starting point for further simulation studies with CORSIKA. These studies can be optimized with regard to the AMIGA muon detector by discarding all particles with energies below the threshold. Since this energy cut will remove nearly all electrons and photons, which account for about 89 % of the total number of particles in an extensive air shower, a significant improvement in efficiency regarding processing time and disk space needed to simulate a shower can be reached.

7. Cluster studies

The second major aim of the simulation studies described here is investigating the clusters that are observed in the prototype data (see Section 5.1). One possible explanation for these clusters is a single muon producing a local electromagnetic shower in the soil above the detector. In this case, a multitude of secondary particles can simultaneously hit a number of scintillator strips located close to each other, which will then result in clusters in the recorded data. With the help of the simulation program described previously, this assumption will be investigated in the following chapter. First, the analysis of the simulations with vertical as well as inclined muons will be presented in detail. Then, these simulations will be compared to the prototype data, taking into account the energy spectrum of muons originating from extensive air showers at ground level. The simulations will be compared to data triggered both internally by an occupancy trigger and externally by a T1 trigger signal from the SD station at which the prototypes have been installed.

7.1. Simulations with vertical muons

The simulation studies presented in the following section have been performed on the basis of 12 000 000 events that have been simulated with vertical muons at eight kinetic energies, ranging from 1 GeV to 200 GeV. For energies above the upper bound of 200 GeV, only very few muons are expected from extensive air showers (see Fig. 6.9), while the lower bound of 1 GeV is motivated by the energy threshold determined in the previous chapter. In total, 1 500 000 events have been accumulated for each of the eight energies.

In Fig. 7.1, four examples of events from these simulated datasets are shown. As in the previous chapter, a cut on the particle type and the energy has been applied, discarding all simulated particles that are unlikely to produce a signal in the scintillator. The majority of events in all datasets is similar to Figs. 7.1(a), (b) and (c), where the primary muon traverses the soil with only a few secondary particles, originating from ionization and excitation processes with the constituents of the soil. However, with increasing energy, more and more events look like the one shown in Fig. 7.1(d), where a large number of secondary particles is produced in the soil, resembling a muon-induced electromagnetic shower. It is known that such electromagnetic showers can be initiated through radiative processes (e.g. bremsstrahlung) of a single muon traversing matter at energies above some 100 GeV [5]. In the simulations described here, though, it has been found that such events with a very large number of secondary particles can also be observed at lower energies down to 10 GeV. A detailed characterization of these showers and the underlying processes is, however, beyond the scope of this thesis. Instead, the measurable effects of these

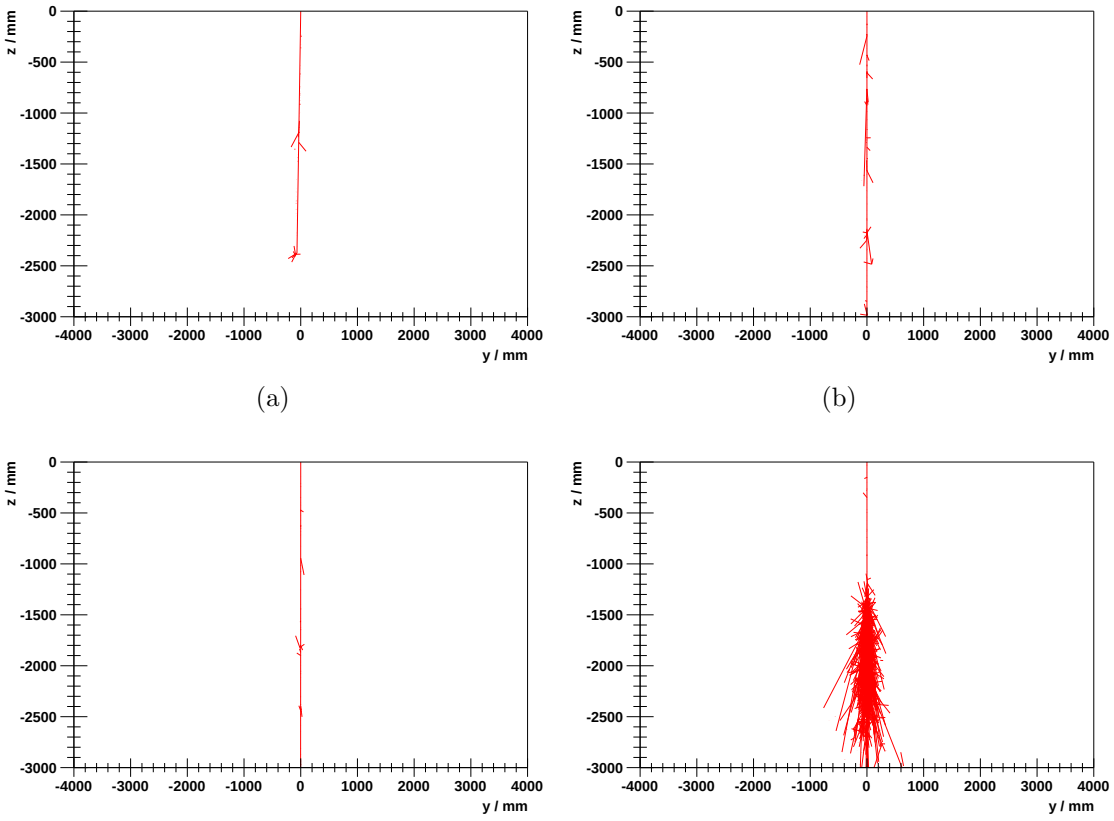

Figure 7.1: Four examples of events with vertical muons at kinetic energies of (a) 1 GeV, (b) 10 GeV, (c) and (d) 100 GeV; here, the projection of the tracks of the simulated particles onto the yz-plane is shown.

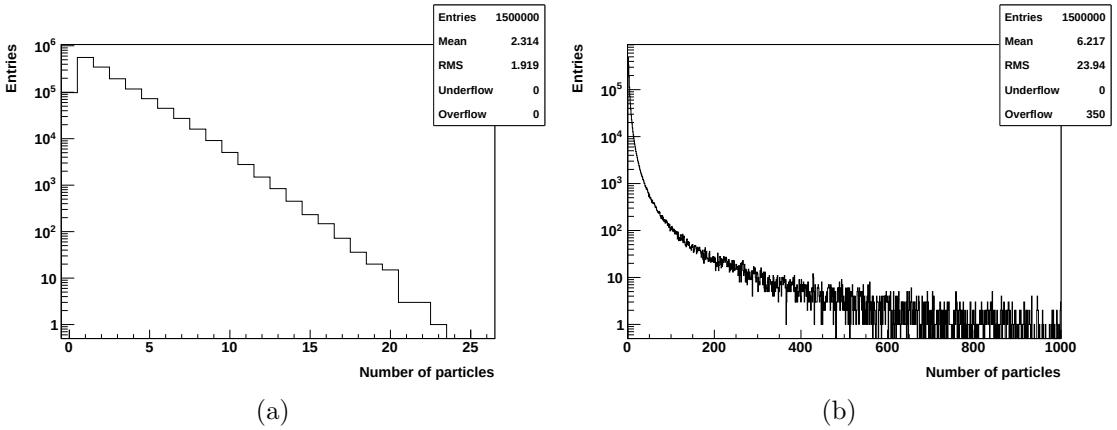

Figure 7.2: Histograms of the number of particles in a depth of 2.25 m for vertical muons at kinetic energies of (a) 1 GeV and (b) 100 GeV.

local showers shall be investigated and quantified using the simulations described above.

The first step in order to interpret and analyze the simulations is to determine the number of particles in a depth of 2.25 m for each event. This number has been obtained in the same way as described in the previous chapter. The resulting distributions are shown in Fig. 7.2 for muons at kinetic energies of 1 GeV and 100 GeV. In the 1 GeV case, the maximum number of particles at a depth of 2.25 m is 23, while in the 100 GeV case, more than 1000 particles are possible, although the majority of events still exhibits only a very small number of particles in the given depth. However, to compare the simulations to the data obtained with the prototype muon counter, the detector and its features have to be taken into account, especially the distribution of the particles over the detector area. In the following, only the 1 GeV case is discussed as an example in order to illustrate the analysis. The results of the analyses of the other energies are summarized in App. B.1.

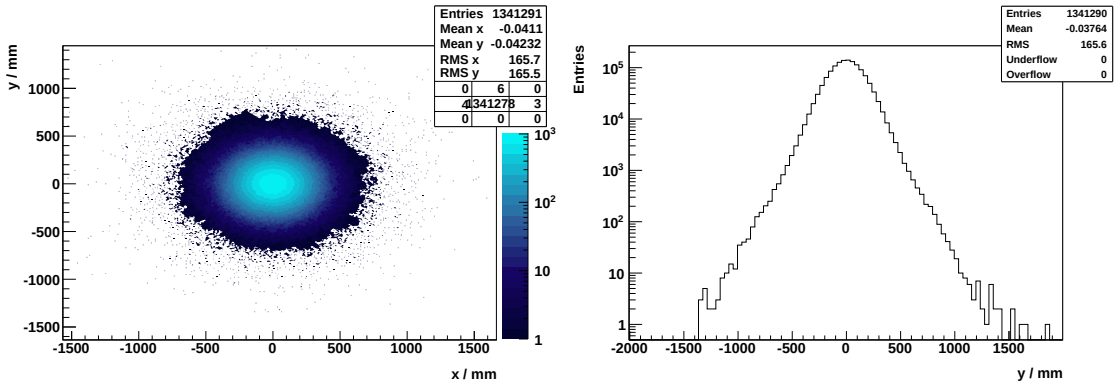

(a) (b)

Figure 7.3: (a) Distribution of particles in the xy-plane at a depth of 2.25 m; superposition of 1 500 000 events with vertical muons at a kinetic energy of 1 GeV; (b) is the projection of (a) onto the y-axis.

In Fig. 7.3(a), the distribution of particles in the xy-plane at a depth of 2.25 m is shown as a superposition of all events from the simulations with primary muons at a kinetic energy of 1 GeV. As expected, the distribution is symmetric in this plane, with the majority of particles localized around the incident direction of the primary muon in the center of the plane. In Fig. 7.3(b), the projection of Fig. 7.3(a) onto the y-axis is shown. In the next step of the analysis, the detector is introduced in a simplified form by dividing the center of the y-axis into 32 bins with a width of 4.1 cm each. Each bin represents one scintillator strip of one half of an AMIGA muon counter module (see Section 4.3). On an event-by-event basis, the particles impinging on these simplified scintillator strips are counted. It is assumed

that each particle hitting a scintillator strip can produce a signal that would show up in the data recorded by the real detector. For the further analysis, it is only relevant whether there was a hit on the respective scintillator strip or not. It will not be distinguished between hits with different x-coordinates, because this information is likewise not available from the prototype data (see Section 4.3). In addition, the time of the hits is not taken into account, since it is assumed that the particles traverse the soil nearly at the speed of light. The differences in the arrival times for each of the particles would be in the order of magnitude of some nanoseconds and could hence not be resolved with the sampling rate of 80 MHz that is currently used in the detector.

It is important to note, however, that the simulation program does not yet include a full detector simulation, where the responses of the scintillator strips, the fibers and the PMT are simulated in detail. The analysis presented here is rather based on a simple counting procedure, where particles that cannot produce a signal in the detector are rejected a priori. On the other hand, this may introduce a bias due to overcounting of particles. For example, a high-energy photon may pass the detector without producing a signal, if it does not interact with the scintillator material. Nevertheless, for the purpose of these simulation studies, this simplified procedure is deemed sufficient.

The histogram of the number of hits per event is shown in Fig. 7.4(a) for the simulations with vertical muons at a kinetic energy of 1 GeV. However, the interpretation of this histogram and especially the comparison to the prototype data may be difficult, because Fig. 7.4(a) contains events, where scintillator strips without hits are found between strips with hits. These "gaps" can be wider than 20 scintillator strips (Fig. 7.4(b)). Events with such large gap sizes can be found in the prototype data as well. However, in the case of real data, it cannot be determined whether the two hits are caused by the secondary particles from a single muon traversing the soil, by a number of different muons simultaneously hitting the detector or by a combination of both. Therefore, for the simulation studies presented in the thesis at hand, it has been decided to discard all events with gaps between the single hits to ensure maximum comparability between the simulated data and the prototype data. Thus, only events, where solely consecutive scintillator strips are hit, forming continuous "clusters", will be considered in the following, both for the simulated datasets as well as for the prototype data. The histogram of the cluster sizes of the 1 GeV dataset is shown in Fig. 7.4(c). From the 1 500 000 events that have been simulated in total with vertical muons at a kinetic energy of 1 GeV, 370 088 events (about 25 %) contain gaps and are thus excluded from further analysis.

The results of the analysis described previously, i.e. the histograms of the cluster

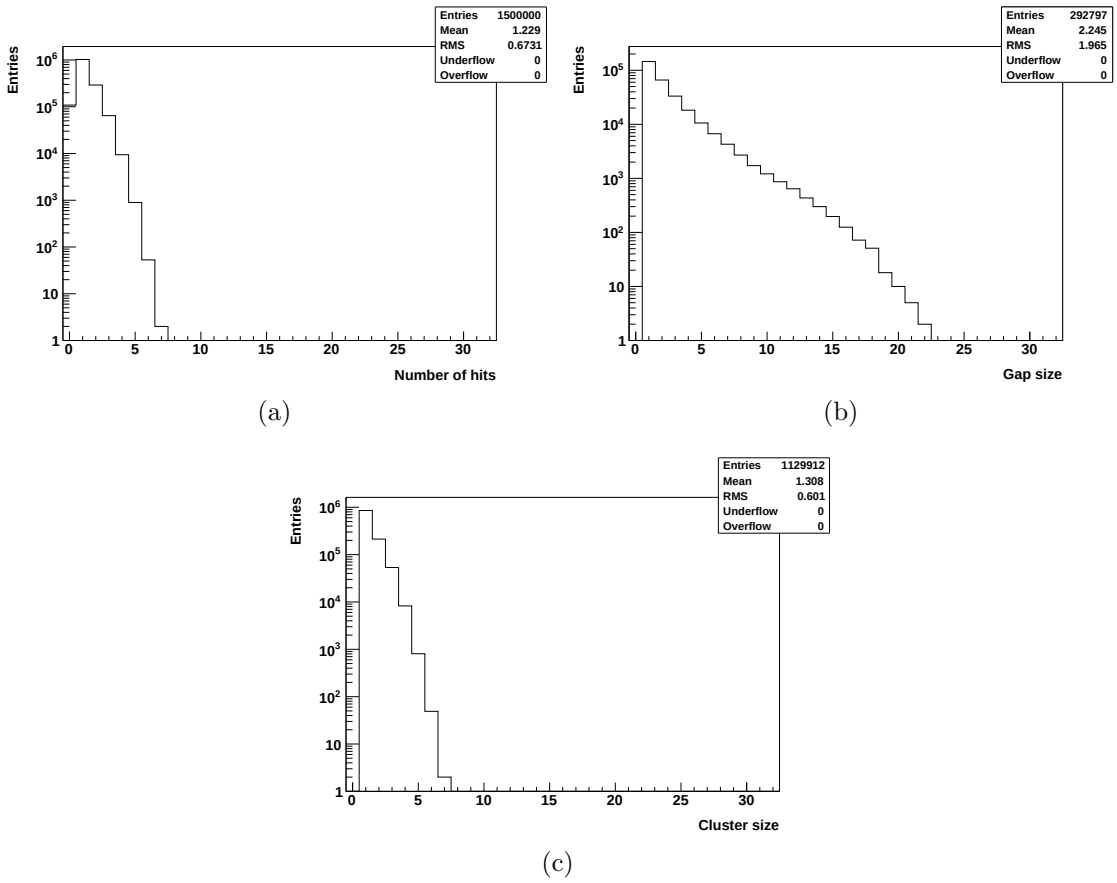

Figure 7.4: Cluster studies for vertical muons at a kinetic energy of 1 GeV; (a) total number of scintillator strips hit; (b) gap sizes between hits; (c) cluster sizes including only events with one continuous cluster without gaps; all histograms are based on the analysis of 1 500 000 events.

sizes, taking into account only events with hits on consecutive scintillator strips, are summarized in App. B.1, Fig. B.1, for all simulated kinetic energies. Comparing the histograms for the different energies, it is found that the width of the distributions is highly dependant on the kinetic energy of the primary muon: the maximum cluster size ranges from 7 at 1 GeV to 26 at 200 GeV. However, for all energies, the majority of events exhibits a cluster size of 1, which means that only the primary muon traverses the detector. From the histograms shown in App. B, it is also apparent that the probability for events with gaps between the single hits increases with the primary energy: at a kinetic energy of 2 GeV, 156 402 events (about 10 %) contain gaps, which increases to 401 784 events (about 27 %) at an energy of 200 GeV. In the 1 GeV case described above, 370 088 events (about 25 %) contain gaps, since, at this energy, the muon may be stopped in the soil before reaching the detector (see Section 6.1), which increases the probability for fragmented clusters due to the secondary particles from the muon decay.

7.2. Simulations with inclined muons

Only a small fraction of the muons originating from extensive air showers impinges vertically on the ground. To account for this, simulations have been performed for inclined muons as well. In the scope of this thesis, zenith angles of 35°, which is the zenith angle for which most of the muons are expected (see Section 7.3.1), and 60°, following the standard zenith angle cut that is most commonly used in data analysis, are considered. For both zenith angles, 1 500 000 events have been simulated for each of the eight energies already used in the vertical muon case. Thus, for each zenith angle, 12 000 000 events have been accumulated in total.

In Fig. 7.5, six examples of events with inclined muons are shown, three for each of the two simulated zenith angles. The main difference between the events for inclined and for vertical muons (Fig. 7.1) is that at low energies, the majority of muons is stopped in the soil before reaching the detector due to the larger amount of soil traversed. Nevertheless, the secondary particles produced by the muon in the soil, especially the electrons from the muon decay, may still reach the detector plane in a depth of 2.25 m. Therefore, the analysis described in the previous section has been modified by correcting the shift of the injection point (see Section 5.2.4) such that the endpoint of the primary muon's track is always above the center of the simplified detector. The effects of the zenith angle on the cluster sizes are already indicated by Figs. 7.5(a) to (d): Still, most muons will only impinge on one or two single scintillator strips. For events with large numbers of secondary particles, however, the footprint of the muon-induced shower on the scintillator will be enlarged by a factor depending on the zenith angle. Therefore, larger cluster sizes will appear in the datasets for inclined muons than in the datasets for vertical muons.

The results of the analysis for inclined muons are summarized in App. B.2, Figs. B.2 and B.3. The histograms of the cluster sizes have been obtained in the same way as described in Section 7.1 for vertical muons, albeit the modification of the analysis at very low energies mentioned before. As expected, the maximum cluster size increases with the zenith angle: at energies of 100 GeV and above, one single muon can even lead to hits in 31 out of 32 scintillator strips (Fig. B.3(g)), thus covering nearly the whole width of the detector. The probability for gaps between hits also varies with the zenith angle: at each energy, the number of events with gaps between hits is larger for inclined muons than for vertical muons. The maximum is again reached at an energy of 200 GeV and a zenith angle of 60° with 825 748 events showing gaps between hits. Therefore, the dataset available for further analysis is reduced by about 55 % for this kinetic energy.

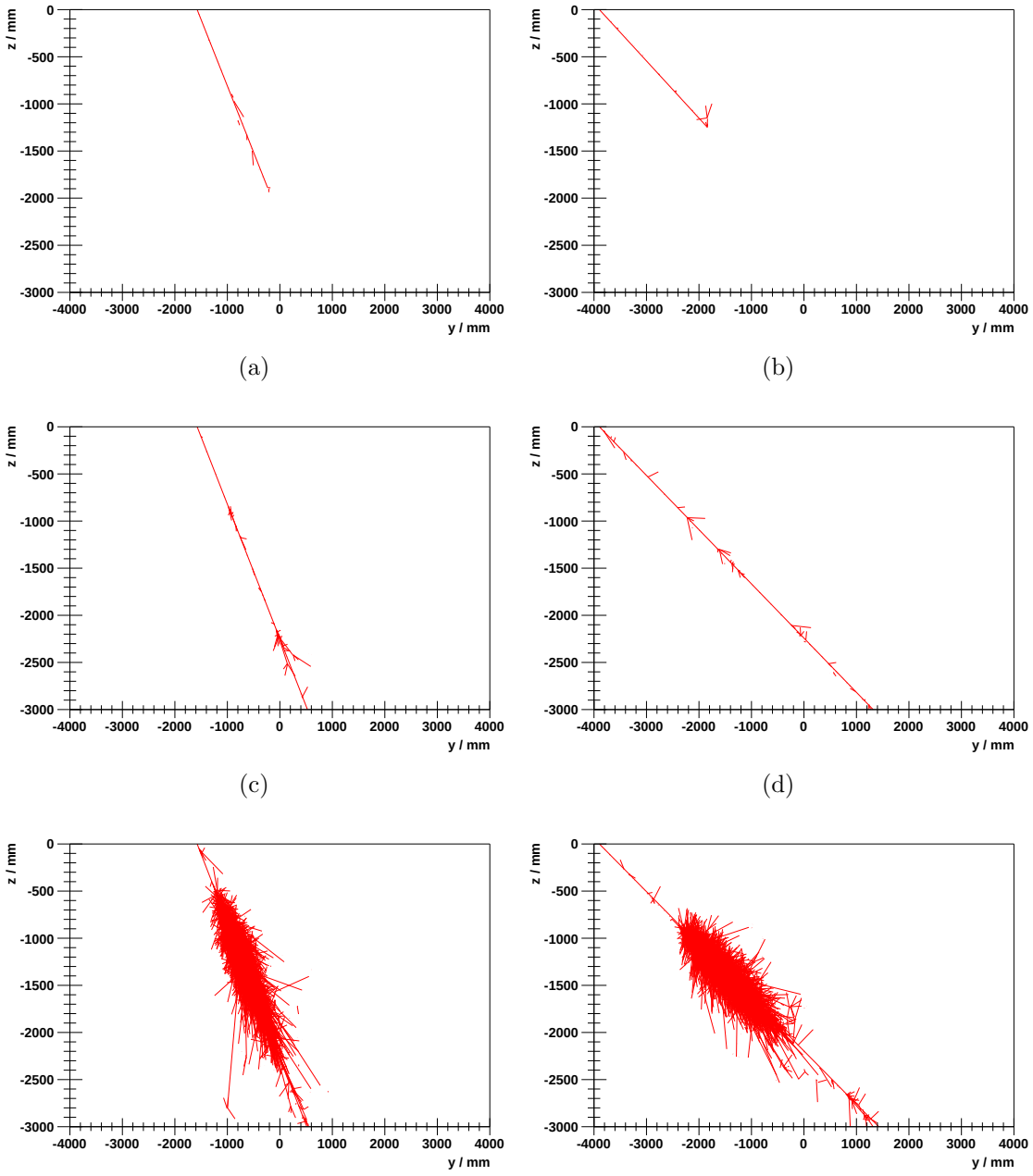

Figure 7.5: Six examples of events with inclined muons at different kinetic energies and zenith angles: (a) 1 GeV, 35°; (b) 1 GeV, 60°; (c) and (e) 100 GeV, 35°; (d) and (f) 100 GeV, 60°; here, the projection of the tracks of the simulated particles onto the yz-plane is shown.

7.3. Comparison with prototype data

The simulations described so far only relate to single muons at fixed energies and zenith angles. Regarding the prototype muon counter deployed in the field, however, muons from a wide range of energies and zenith angles impinge on the ground above the detector. Hence, the energy and zenith angle distributions of muons have to be taken into account to compare the simulations to the prototype data. The energy spectrum will be discussed in the following, before it is utilized to weight the single simulations. In this way, the prototype data can be constructed from the simulations.

The baseline assumption of the following comparison is that all signals apparent in the data are caused by muons, either directly or indirectly through secondary particles produced in the soil. A possible contribution of other particles originating from extensive air showers, for example electrons or photons, is neglected because of two reasons: firstly, the number of particles originating from extensive air showers other than muons that are able to traverse the 2.25 m of soil is expected to be very small (see Section 6.3). Secondly, the observed event rate is, in the case of the internal occupancy trigger, at least by one order of magnitude too high compared to the expectation: the average event rate using an eightfold occupancy trigger is about 0.1 Hz (see Section 5.1), while an estimate from the energy spectrum of primary cosmic rays and the lateral distribution functions of the particles originating from an extensive air shower yields an expected rate of 0.01 Hz [57]. Thus, it can be concluded that all particles other than muons can be neglected in the scope of the following comparison.

7.3.1. Muon spectrum

In this thesis, the muon spectrum described in [61] is used, which is based on a compilation of several experimental results for the flux of vertical muons at sea level, both from extensive air showers that reach the ground as well as from those showers that die out in the atmosphere. This spectrum will be briefly discussed in the following section.

Parameter	Fit result
p_0	0.86 ± 0.06
p_1	0.133 ± 0.002
p_2	-2.521 ± 0.004
p_3	-5.78 ± 0.03
p_4	-2.11 ± 0.03

Table 7.1: Parameters of the differential muon spectrum described by Eq. (7.1) [61].

The differential muon flux φ as a function of the muon momentum p can be parameterized by

$$\begin{aligned}
\varphi(y) &= p_0 \times 10^{H(y)}\,\mathrm{m}^{-2}\,\mathrm{sr}^{-1}\,\mathrm{s}^{-1}\,\mathrm{GeV}^{-1}, \\
H(y) &= p_1\left(y^3/2 - 5y^2/2 + 3y\right) \\
&\quad + p_2\left(-2y^3/3 + 3y^2 - 10y/3 + 1\right) \\
&\quad + p_3\left(y^3/6 - y^2/2 + y/3\right) \\
&\quad + p_4\left(y^3/3 - 2y^2 + 11y/3 - 2\right), \\
y &= \log_{10}\left(p \;/\; \mathrm{GeV}\right),
\end{aligned} \tag{7.1}$$

where the individual terms are motivated empirically [61]. The parameters p_0 to p_4 have been obtained by a fit to several experimental results, the fit results are listed in Tab. 7.1. For a complete list of the experimental results that were considered for this fit, see [61]. Using these parameters, the differential muon spectrum has been plotted with the kinetic energy of the muon on the abscissa for energies from 1 GeV to 1000 GeV (Fig. 7.6). In this plot, the differential muon flux φ has been multiplied by a factor of E^3, as in [61], to emphasize the structures contained within the spectrum.

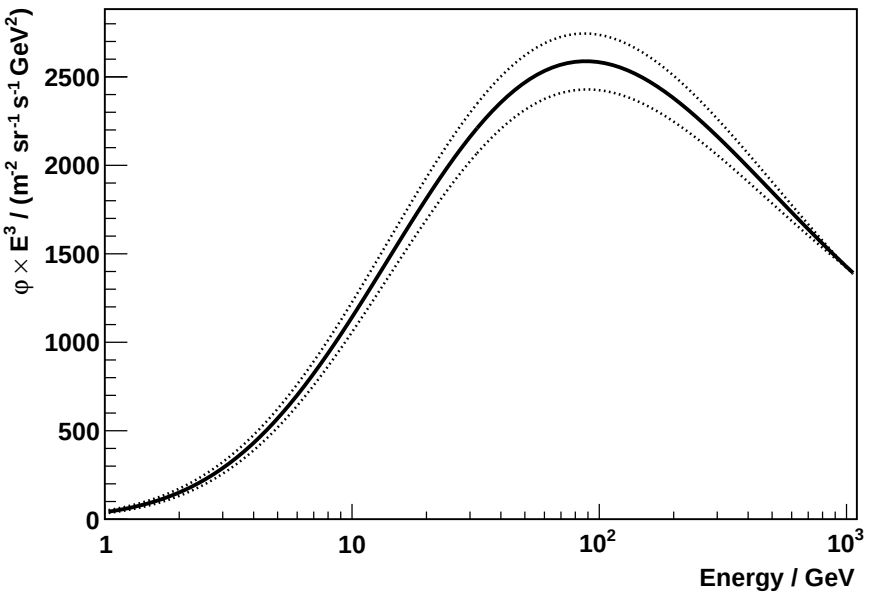

Figure 7.6: The differential flux of vertical muons at sea level according to [61] in dependance on the kinetic energy of the muon; the differential muon flux is multiplied by a factor of E^3 to emphasize structures; the dotted lines indicate the 1σ uncertainty band.

Eq. 7.1 only describes the vertical muon flux at sea level. Thus, the dependancies of the flux on the altitude and the zenith angle need to be known. The altitude dependance can be parameterized empirically by

$$\frac{\varphi(h)}{\varphi(h = 0\,\mathrm{m})} = e^{h/L}, \tag{7.2}$$

where h is the altitude, $L = 4900\,\mathrm{m} + 750\,\mathrm{m} \times p/\mathrm{GeV}$ and p is the muon momentum [61]. The overall uncertainty on this parametrization is ± 0.003. Regarding the zenith angle dependance, the usual parameterization

$$\frac{\varphi(\theta)}{\varphi(\theta = 0^\circ)} = \cos^2(\theta) \tag{7.3}$$

is used [18]. The integrated muon flux is also modified by the zenith angle dependance of the solid angle differential. Thus, the muon flux is expected to be largest in the zenith angle region around 35°.

It has to be noted that the parametrization given by Eq. 7.1 is, strictly speaking, only valid for muon momenta above $10\,\mathrm{GeV}/c$ since at lower momenta, the muon spectrum is affected by the geomagnetic field. However, in the scope of the thesis at hand, these effects will be neglected and the muon spectrum given by Eq. 7.1 will be extrapolated down to about $1\,\mathrm{GeV}/c$. In order to estimate the reliability of this extrapolation, the extrapolated muon flux at $1\,\mathrm{GeV}/c$ has been compared to direct measurements taken by the balloon-borne CAPRICE94 apparatus (Cosmic Antiparticle Ring Imaging Cherenkov Experiment 1994, [62]):

$$\varphi(1\,\mathrm{GeV}/c)_{\mathrm{extr.}} = (50 \pm 9)\ \mathrm{m}^{-2}\ \mathrm{sr}^{-1}\ \mathrm{s}^{-1}\ \mathrm{GeV}^{-1}, \tag{7.4}$$

$$\varphi(1\,\mathrm{GeV}/c)_{\mathrm{meas.}} = (40 \pm 1)\ \mathrm{m}^{-2}\ \mathrm{sr}^{-1}\ \mathrm{s}^{-1}\ \mathrm{GeV}^{-1}. \tag{7.5}$$

Both values are in agreement within the quoted uncertainties. Thus, the extrapolation is sufficiently reliable for the purpose of the first studies presented in this thesis.

From the spectrum described by Eq. 7.1 in conjunction with Eqs. (7.2) and (7.3), it is now possible to calculate the expected muon rates, with which the simulation results can be weighted. Since vertical muons (0° zenith angle) as well as inclined muons (35° and 60° zenith angle) have been simulated, the muon rates have been calculated for three zenith angle intervals (0° to 25°, 25° to 45° and 45° to 60°). The energy intervals, over which the differential flux has been integrated, have been chosen such that the simulated energy is always in the center of the interval. The lower bound of the first energy interval is set to 0.8 GeV, which corresponds to the energy threshold for muons obtained in Section 6.1. Since the highest simulated energy is 200 GeV, the upper bound of the last energy interval is at 278.8 GeV. Because of the rapidly decreasing differential flux, this energy range is sufficient

to obtain a reliable estimate of the muon rates. Increasing the upper bound would affect the muon rates by less than one promille. In Tab. 7.2, the integrated muon fluxes are listed for each of the zenith angle and energy intervals. The total expected muon rate, i.e. the sum of all intervals, is found to be

$$\Phi_\mu = (190 \pm 30)\ \mathrm{m}^{-2}\ \mathrm{s}^{-1}, \tag{7.6}$$

where the order of magnitude is in agreement with the expected muon flux through an SD station [27].

Energy interval / GeV	**Int. muon flux / $\mathbf{m^{-2}\ s^{-1}}$**
$0.8 - 1.2$	10 ± 2
$1.2 - 2.8$	21 ± 3
$2.8 - 7.2$	15 ± 2
$7.2 - 12.8$	4.2 ± 0.3
$12.8 - 27.2$	2.3 ± 0.2
$27.2 - 72.8$	0.75 ± 0.05
$72.8 - 127.2$	0.089 ± 0.006
$127.2 - 278.8$	0.032 ± 0.002

(a)

Energy interval / GeV	**Int. muon flux / $\mathbf{m^{-2}\ s^{-1}}$**
$0.8 - 1.2$	17 ± 3
$1.2 - 2.8$	33 ± 5
$2.8 - 7.2$	23 ± 2
$7.2 - 12.8$	6.4 ± 0.5
$12.8 - 27.2$	3.5 ± 0.2
$27.2 - 72.8$	1.14 ± 0.08
$72.8 - 127.2$	0.136 ± 0.009
$127.2 - 278.8$	0.049 ± 0.003

(b)

Energy interval / GeV	**Int. muon flux / $\mathbf{m^{-2}\ s^{-1}}$**
$0.8 - 1.2$	10 ± 2
$1.2 - 2.8$	19 ± 3
$2.8 - 7.2$	13 ± 1
$7.2 - 12.8$	3.8 ± 0.3
$12.8 - 27.2$	2.0 ± 0.1
$27.2 - 72.8$	0.67 ± 0.04
$72.8 - 127.2$	0.080 ± 0.005
$127.2 - 278.8$	0.029 ± 0.002

(c)

Table 7.2: Integrated muon fluxes calculated from Eq. 7.1 for several energy intervals for an altitude of 1400 m and zenith angle intervals of (a) 0 - 25°, (b) 25 - 45° and (c) 45 - 60°.

7.3.2. Occupancy data

With the muon spectrum known, the simulations can now be weighted accordingly and compared to the data recorded by the $5\,\mathrm{m}^2$ prototype. A comparison to the data from the $10\,\mathrm{m}^2$ prototype is not possible in the scope of this thesis, due to a difference in the design of the scintillator modules used for the prototypes. Five scintillator strips of the $10\,\mathrm{m}^2$ prototype have not been coupled to the PMT to study different aspects of the scintillator in detail. Therefore, a comparison with the data obtained with this prototype is difficult, especially under the condition of continuous clusters.

As reference dataset, the dataset `10-03-23-HV950V-OCC8-PRESCALE0-THR100mV`, already described in Section 5.1, has been chosen because it is the dataset with the highest statistics available. On this dataset, the same selection criteria have been applied as for the simulations described previously. Hence, only events with continuous clusters in the trigger time bin and without gaps between the single hits have been selected. In addition, only clusters on one half of the scintillator are taken into account. The distribution of cluster sizes for this dataset is shown in Fig. 7.7. The distribution begins at a cluster size of eight, because the dataset was recorded with an eightfold occupancy trigger. Thus, the dataset only contains events with at

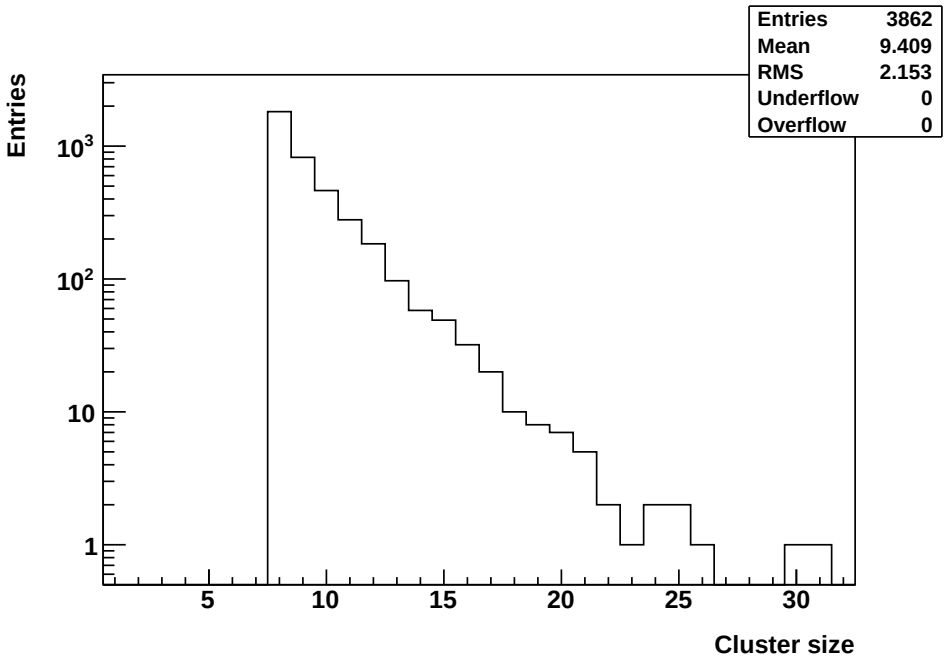

Figure 7.7: Cluster sizes (excluding events with gaps between hits) for occupancy data recorded by the 5 m^2 prototype (dataset `10-03-23-HV950V-OCC8-PRESCALE0-THR100mV`) [48].

least eight scintillator strips simultaneously showing a signal. In total, the reduced dataset contains 3 862 events, which is about 2 % of the total number of events in the whole dataset. As expected, smaller cluster sizes occur more often than larger cluster sizes, with the maximum cluster size being around 30.

Under the simplest assumption that the dataset contains only muon-induced events, this histogram can be constructed from the simulations using

$$\tilde{n}_i = \sum_{jk} \left(\Phi_{jk} \; A \; t \; \epsilon \; \frac{n_{ijk}}{N_{ij}} \right), \tag{7.7}$$

where $\tilde{n}_i$ denotes the constructed (expected) histogram bin content for the cluster size i. n_{ijk} is the respective histogram bin content for the simulations at a kinetic energy j and a zenith angle k, whereas N_{ij} denotes the total number of events simulated at the respective kinetic energy and zenith angle. Thus, the fraction $\frac{n_{ijk}}{N_{ij}}$ can be understood as the probability for a muon at a given energy j and a given zenith angle k to produce a cluster of size i. ϵ is a parameter that describes the overall normalization of the distribution. From the expected muon rates Φ_{jk} in the associated energy and zenith angle intervals, listed in Tab. 7.2, the area A of the detector ($5\,\mathrm{m}^2$) and the measurement time t (about 15 d), the expected number of muons impinging on the detector can be calculated, which in conjunction with the probabilities for each cluster size and the overall normalization yields the expected distribution of cluster sizes. However, the overall normalization is not known. Thus, the parameter ϵ in Eq. (7.7) is left as a free parameter, which will be fixed afterwards by normalizing the resulting distribution to the data.

The resulting histogram is shown in Fig. 7.8 in comparison to the prototype data. For the data, the statistical uncertainties have been included as well, whereas the uncertainties of the simulations are negligible due to the large number of simulated events and have therefore been omitted from Fig. 7.8. The normalization parameter ϵ in Eq. (7.7) has been chosen such that the integral of the histogram for the simulations is equal to the integral of the data. Another possibility would be normalizing to the bin with the highest content. However, since this bin dominates the integral as well, both normalizations lead to comparable results. Thus, only the normalization to the integral of the data has been chosen for the present analysis. The normalization parameter obtained in this way is

$$\epsilon = 0.011 \pm 0.009, \tag{7.8}$$

where the uncertainty is dominated by the statistical uncertainties of the prototype data. However, for a first comparison of the simulations to the prototype data, only the shape of the distributions is taken into account, without taking into account the normalization. A qualitative comparison from Fig. 7.8 shows that the simulations

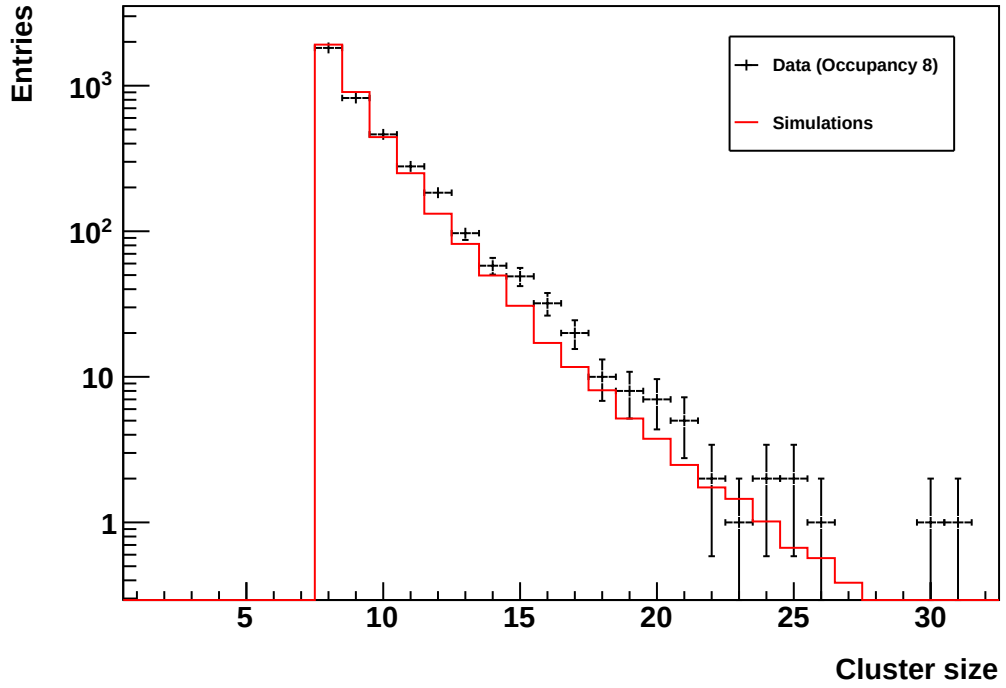

Figure 7.8: Cluster sizes (excluding events with gaps between hits); simulations weighted according to the muon energy spectrum and compared to occupancy data recorded by the $5\,\mathrm{m}^2$ prototype (see Fig. 7.7); the simulations have been normalized to the integral of the data.

are in good agreement with the data, despite the simplifying assumptions made to derive the histogram from the simulated events. To quantify the agreement between both histograms, a standard χ^2 test, as described in [63], has been performed. The results of this test are as follows:

$$\chi^2 = 35.91, \tag{7.9}$$
$$NDF = 23, \tag{7.10}$$
$$\chi^2/NDF = 1.56, \tag{7.11}$$

where NDF stands for the number of degrees of freedom. The good agreement already apparent from Fig. 7.8 manifests itself also in the χ^2/NDF value close to 1. From this, it can be concluded that single muons producing locally secondary particles in the soil above the detector are indeed a possible explanation for the clusters apparent in the data.

However, the analysis described previously uses only a very small fraction (about 2 %) of the data. In addition, this data has been recorded with an eightfold occupancy trigger. Thus, the dataset, which the simulations have been compared with, contains

mostly events that would have been suppressed in the final setup, where the muon counter electronics is externally triggered by a signal from the surface detector. This situation will be investigated in the next section.

7.3.3. T1 data

As reference dataset for the T1 data, the dataset `10-11-06-twomodules-HV950V-T1-PRESCALE0-THR100mV` has been chosen. The data has been recorded with the same settings as the reference dataset for occupancy data: the high voltage for the PMT was set to 950 V, the thresholds of the discriminators were fixed to a value of 100 mV and the prescaler was disabled. The main difference between both datasets is the trigger. For the dataset described in this section, a T1 signal from the surface detector station has been used as the trigger. This signal is sent simultaneously to both the $5\,\mathrm{m}^2$ and the $10\,\mathrm{m}^2$ prototype, which allows for a detailed comparison of the behaviour of both prototypes. In the following, only the data recorded by the $5\,\mathrm{m}^2$ prototype is used. In total, the dataset comprises 128 757 events. However, only 1 682 events (1.3 %) out of these contain any data, whereas all other events are empty. This is in agreement with the expectation from the different T1 trigger conditions at single station level (see Section 3.1.1). The TH-T1 trigger with a trigger rate of about 100 Hz is dominated by single muons, whereas the ToT-T1 trigger condition (trigger rate about 2 Hz) is only fulfilled by extensive air showers. However, single muons triggering the SD station cannot produce a signal in the AMIGA muon counter as well because of the detector geometry (see Fig. 4.5). Therefore, these events will be empty, although they are still recorded because of the trigger signal. An extensive air shower will, on the other hand, most likely produce a signal in the muon counter as well, because of its large footprint on ground level. Thus, the ratio of events with and without data is expected to be in the order of magnitude of the ratio of the ToT-T1 and the TH-T1 trigger rates [45], which is the case for this dataset.

In Fig. 7.9, the cluster sizes for this dataset, excluding all events with gaps between the single hits, are shown. In the case of T1 data, the maximum cluster size is 5, which is small compared to the maximum cluster size of 31 for the occupancy data (see Fig. 7.7). This difference is mainly due to the restrictive condition of eight channels simultaneously showing a signal in the case of the occupancy data, which prevents events with cluster sizes smaller than eight. In the case of the T1 data, this condition is omitted. Thus, the distribution of cluster sizes is dominated by small cluster sizes, as expected from the simulations (see App. B). Furthermore, the reduced dataset for the T1 data contains only 719 events, which is about 20 % of the number of events from the occupancy dataset that has been used for comparison with the simulations.

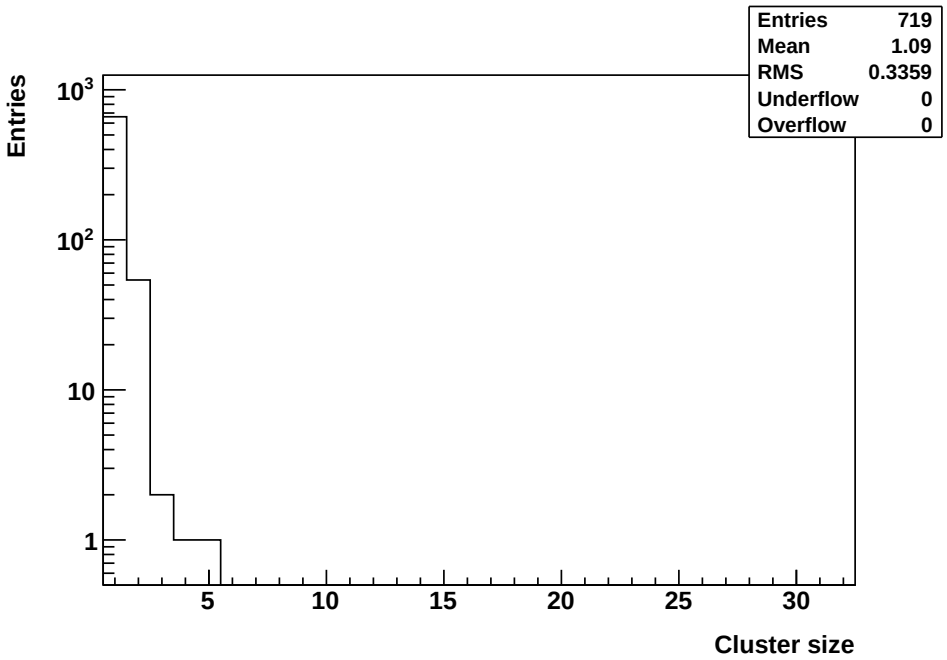

Figure 7.9: Cluster sizes (excluding events with gaps between hits) for T1 data recorded by the 5 m^2 prototype (dataset `10-11-06-twomodules-HV950V-T1-PRESCALE0-THR100mV`) [48].

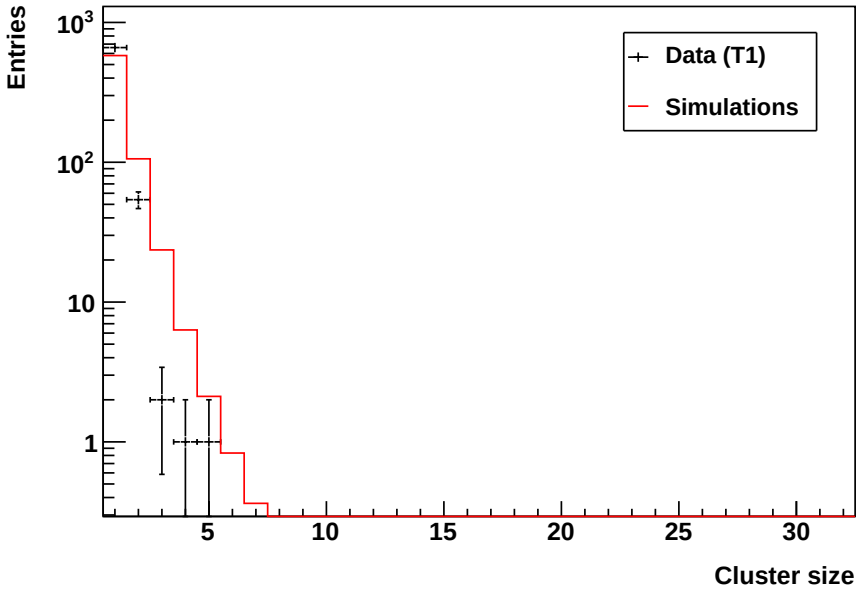

Figure 7.10: Cluster sizes (excluding events with gaps between hits); simulations weighted according to the muon energy spectrum and compared to T1 data recorded by the 5 m^2 prototype (see Fig. 7.9); the simulations have been normalized to the integral of the data.

This histogram can be compared to the simulations in the same way as described in the previous section for the occupancy data. The resulting distribution is shown in Fig. 7.10. Again, the simulations have been normalized such that the integral of the simulations histogram is equal to the data. In contrast to the occupancy data, there is an obvious discrepancy between the simulations and the T1 data: the distribution for the T1 data is steeper than the distribution calculated from the simulations, so that the expected number of events for the single cluster sizes is overestimated by the simulations. Again, a χ^2 test has been performed:

$$\chi^2 = 39.78, \tag{7.12}$$
$$NDF = 4, \tag{7.13}$$
$$\chi^2/NDF = 9.95. \tag{7.14}$$

Here, only the five bins containing entries have been included in the χ^2 test. The mismatch between the weighted simulations and the data is also apparent in the χ^2/NDF value much larger than 1.

The difference between the distributions obtained from the simulations and the data is mainly due to the muon spectrum that has been used to weight the simulations. This spectrum, as described in Section 7.3.1, describes all muons on ground level, regardless of whether the extensive air shower, from which these muons originate, reaches the ground or not. This distinction is likewise not made when employing the occupancy trigger. In this case, the spectrum can be used to weight the simulations without problems. For the T1 data, however, the situation is slightly different: here, only muons from an extensive air shower that triggers the SD station are detected by the AMIGA muon counter. The energy distribution of muons in a specific extensive air shower is different from the cumulative energy distribution of all muons on ground level (see e.g. Fig. 6.9), which affects also the factors with which the single simulations would have to be weighted. The calculation of these corrected weighting factors is, however, beyond the scope of this thesis. For this calculation, not only the energy distribution of the muons from an extensive air shower would have to be taken into account, but also the energy spectrum of the primary cosmic rays by which the extensive air shower is initiated in the atmosphere. This calculation will be, however, subject of future simulation studies that will be performed for the AMIGA enhancement on the basis of the thesis at hand.

8. Summary and Outlook

The subject of this thesis was to perform simulation studies for the muon counter prototypes of the AMIGA (Auger Muons and Infill for the Ground Array) enhancement of the Pierre Auger Observatory. In particular, these studies were aimed at gaining a basic understanding of the prototype detectors and the data as well as providing a possible explanation for certain features that are apparent in the prototype data.

After a brief introduction into the field of cosmic rays and extensive air showers (Chapter 2), the Pierre Auger Observatory (Chapter 3) and the AMIGA enhancement (Chapter 4), the simulation program, with which these studies have been performed, has been discussed in detail (Chapter 5). This program is based on the Geant4 toolkit and features a modular structure that can be easily modified and extended. For the studies presented in this thesis, a simple geometry has been employed in conjunction with a short physics list, taking into account only the electromagnetic interactions. The parametrization of the soil is based on a geological characterization of the soil in the area where the AMIGA enhancement is located.

Using this simulation program, two subjects have been dealt with: firstly, energy thresholds have been determined for different particle types (Chapter 6). These thresholds can be understood as the minimum energy a particle originating from an extensive air shower must have in order to pass the 2.25 m of soil and produce a signal in the AMIGA scintillator. The thresholds have been determined by taking into account not only the primary particle but also the secondary particles produced in the soil above the detector, albeit only those secondary particles that can produce a signal in the detector (i.e. ignoring e.g. neutrinos and low-energy particles). In the scope of this thesis, thresholds have been determined for muons, electrons, photons, protons, neutrons and pions. The results are listed in Tab. 6.2. For muons, additional thresholds have been determined using only the penetration depth of the primary muon. These values have been validated by cross checking the results with independent calculations from the Bethe-Bloch formula as well as by comparing the thresholds with those calculated for antimuons. In both cases, no deviations from the expectation have been found. Therefore, it can be concluded that the simulation program works as intended. In addition, from these thresholds in conjunction with the expected energy distributions at ground level for different particles originating from extensive air showers, the contribution of particles other than muons to the data can be calculated. The knowledge of this contribution is important to correctly assess the number of muons in an extensive air shower from the recorded data, which is one of the main aims of the AMIGA enhancement. In addition, the thresholds determined in this thesis can be employed to optimize shower simulations, for example with CORSIKA, to be more efficient in both computing time and disk space needed.

The second part was dedicated to the study of the clusters that are apparent in the data that has been recorded by the prototypes (Chapter 7). In particular, it was investigated whether these clusters could be explained by a single muon producing a local electromagnetic shower in the soil above the detector, thus producing signals in a number of strips located close to each other. For the studies presented in this thesis, 36 000 000 events have been simulated at different energies and zenith angles. The analysis of these events was based on counting the particles in a depth of 2.25 m. For this purpose, the xy-plane at this depth has been segmented according to one half of an AMIGA muon counter module, with each segment corresponding to one scintillator strip. It was assumed that each particle that has been counted in one segment would produce a signal in the corresponding scintillator strip. In the analysis presented in this thesis, only events with continuous clusters have been taken into account. The results of the analyses have been summarized in App. B. It has been found that single muons at high energies (above 100 GeV) and a zenith angle of 60° can produce clusters that cover nearly the whole detector. In order to further investigate this issue, the simulations have been compared to the data obtained with the 5 m^2 prototype by weighting the simulations for each energy and zenith angle with the expected muon rate calculated from the energy spectrum of muons on ground level. In the case of internally triggered data (occupancy trigger), the shape of the distribution calculated from the simulations matches the data very well ($\chi^2/NDF = 1.56$). For the externally triggered data (T1 trigger), there is a discrepancy between the distribution for the simulations and the data ($\chi^2/NDF = 9.95$). This mismatch can be related to the muon spectrum used to obtain the weighting factors for the simulations, since this spectrum takes into account also muons from extensive air showers that do not reach the ground and can thus not produce a T1 trigger signal in the SD station that is connected to the prototype. In total, the results of this chapter can be seen as a strong hint that the clusters apparent in the recorded data can be caused by single muons. However, so far only a very small fraction of the data (about 2 % of the occupancy data) has been compared to the simulations. In addition, events with large cluster sizes are suppressed, when replacing the eightfold occupancy trigger with an external T1 trigger signal (see Section 7.3.3). Thus, additional simulation studies are needed in order to correctly interpret the T1 data and, in future, the data triggered by a T3 trigger signal from the central data acquisition system (CDAS) of the Pierre Auger Observatory.

The simulation studies presented here are only the first step toward a more detailed analysis. As the AMIGA project grows, the simulations have to consider more and more detailed aspects of the detectors. For example, the simulation program described in Chapter 5 can be extended to a full detector simulation, modelling the responses of the scintillator, the fibres and the photomultiplier in detail. Since the construction of the unitary cell will begin in the near future, shower simulations, e.g.

with the CORSIKA program, become more important to study the response of the muon counter array to an extensive air shower. These shower simulations in conjunction with the Geant4 based simulation studies, for which the foundation has been laid in the previous chapter, will be an important part of a full simulation chain, which will be needed in future to compare and validate the data obtained by the detectors. Ultimately, this full simulation chain will be incorporated into the official Auger software framework. Even without the full simulation chain, more specialized studies are possible: for example, it is currently under discussion whether the manhole, with which the prototype muon detectors have been equipped, influences the data in any way. Particles other than muons may pass the manhole and produce a signal in the area of the scintillators that is not covered by soil. From the data, such events cannot be distinguished from muon induced events. Thus, simulation studies are needed to estimate a possible contribution of such events to the data that has been recorded with the prototypes. Since the simulation program presented in this thesis has been designed in a modular way, it can be easily modified to enable such studies.

Appendices

A. Detailed results of the fits performed in Chapter 6

A.1. Muons

Calculation from the most probable penetration depth:

- Corresponding plot: Fig. 6.2(a)
- Function that has been fitted:

$$y(x) = p_0 \; + \; p_1 \; x \tag{A.1}$$

- Fit results:

$$\begin{aligned} p_0 &= -64.3 \pm 0.5 \\ p_1 &= 2.3967 \pm 0.0006 \end{aligned} \tag{A.2}$$

- Inverse function:

$$x(y) = \frac{1}{p_1} \; (y - p_0) \tag{A.3}$$

- Function to determine uncertainty (using error propagation):

$$\delta x = \frac{1}{p_1} \sqrt{(\delta p_0)^2 + x^2 \; (\delta p_1)^2} \tag{A.4}$$

- Result for energy threshold, corresponding to $y = 2250\,(\mathrm{mm})$:

$$E_{\mathrm{thr}} = (965.6 \pm 0.3) \text{ MeV} \tag{A.5}$$

Calculation from the 0.95-quantile of the penetration depth:

- Corresponding plot: Fig. 6.2(b)
- Function that has been fitted:

$$y(x) = p_0 \; + \; p_1 \; x \tag{A.6}$$

- Fit results:

$$\begin{aligned} p_0 &= -47.6 \pm 0.9 \\ p_1 &= 2.4642 \pm 0.0011 \end{aligned} \tag{A.7}$$

- Inverse function:
$$x(y) = \frac{1}{p_1} \ (y - p_0) \tag{A.8}$$

- Function to determine uncertainty (using error propagation):
$$\delta x = \frac{1}{p_1}\sqrt{(\delta p_0)^2 + x^2 \ (\delta p_1)^2} \tag{A.9}$$

- Result for energy threshold, corresponding to $y = 2250\,(\text{mm})$:
$$E_{\text{thr}} = (932.4 \pm 0.6)\ \text{MeV} \tag{A.10}$$

Calculation from the fraction of events with no particles at all in a depth of 2.25 m:

- Corresponding plot: Fig. 6.4

- Function that has been fitted:
$$y(x) = \frac{1}{\left(1 \ + \ p_0 \ e^{p_1(x+p_2)}\right)^{1/p_3}} \tag{A.11}$$

- Fit results:
$$\begin{aligned} p_0 &= -0.033 \pm 0.002 \\ p_1 &= 0.0175 \pm 0.0002 \\ p_2 &= -786 \pm 3 \\ p_3 &= -0.92 \pm 0.05 \end{aligned} \tag{A.12}$$

- Inverse function:
$$x(y) = \frac{1}{p_1} \ \ln\left(\frac{1}{p_0} \ \left(\frac{1}{y^{p_3}}\right)\right) - p_2 \tag{A.13}$$

- Function to determine uncertainty (using error propagation):
$$\delta x = \sqrt{\left(\frac{\delta p_0}{p_0 \ p_1}\right)^2 + \left(\frac{x + p_2}{p_1}\delta p_1\right)^2 + (\delta p_2)^2 + \left(\ln(x)\,\frac{\delta p_0}{p_1\,(x^{p_3-1})}\right)^2} \tag{A.14}$$

- Result for energy threshold, corresponding to $y = 0.95$:
$$E_{\text{thr}} = (800 \pm 20)\ \text{MeV} \tag{A.15}$$

A.2. Antimuons

Calculation from the most probable penetration depth:

- Corresponding plot: Fig. 6.5(a)
- Function that has been fitted:

$$y(x) = p_0 \ + \ p_1 \ x \tag{A.16}$$

- Fit results:

$$\begin{aligned} p_0 &= -60.2 \pm 0.5 \\ p_1 &= 2.3925 \pm 0.0006 \end{aligned} \tag{A.17}$$

- Inverse function:

$$x(y) = \frac{1}{p_1} \ (y - p_0) \tag{A.18}$$

- Function to determine uncertainty (using error propagation):

$$\delta x = \frac{1}{p_1} \sqrt{(\delta p_0)^2 + x^2 \ (\delta p_1)^2} \tag{A.19}$$

- Result for energy threshold, corresponding to $y = 2250\,(\mathrm{mm})$):

$$E_{\mathrm{thr}} = (965.6 \pm 0.3) \ \mathrm{MeV} \tag{A.20}$$

Calculation from the 0.95-quantile of the penetration depth:

- Corresponding plot: Fig. 6.5(b)
- Function that has been fitted:

$$y(x) = p_0 \ + \ p_1 \ x \tag{A.21}$$

- Fit results:

$$\begin{aligned} p_0 &= -44.1 \pm 0.9 \\ p_1 &= 2.4609 \pm 0.0011 \end{aligned} \tag{A.22}$$

- Inverse function:

$$x(y) = \frac{1}{p_1} \ (y - p_0) \tag{A.23}$$

- Function to determine uncertainty (using error propagation):

$$\delta x = \frac{1}{p_1}\sqrt{(\delta p_0)^2 + x^2 \ (\delta p_1)^2} \tag{A.24}$$

- Result for energy threshold, corresponding to $y = 2250\,(\mathrm{mm})$):

$$E_{\mathrm{thr}} = (932.2 \pm 0.6)\ \mathrm{MeV} \tag{A.25}$$

Calculation from the fraction of events with no particles at all in a depth of 2.25 m:

- Corresponding plot: Fig. 6.5(c)
- Function that has been fitted:

$$y(x) = \frac{1}{\left(1 \ + \ p_0 \ e^{p_1(x+p_2)}\right)^{1/p_3}} \tag{A.26}$$

- Fit results:

$$\begin{aligned} p_0 &= -0.0161 \pm 0.0010 \\ p_1 &= 0.0193 \pm 0.0002 \\ p_2 &= -786 \pm 3 \\ p_3 &= -0.38 \pm 0.02 \end{aligned} \tag{A.27}$$

- Inverse function:

$$x(y) = \frac{1}{p_1} \ \ln\left(\frac{1}{p_0} \ \left(\frac{1}{y^{p_3}}\right)\right) - p_2 \tag{A.28}$$

- Function to determine uncertainty (using error propagation):

$$\delta x = \sqrt{\left(\frac{\delta p_0}{p_0 \ p_1}\right)^2 + \left(\frac{x + p_2}{p_1}\delta p_1\right)^2 + (\delta p_2)^2 + \left(\ln(x)\,\frac{\delta p_0}{p_1\,(x^{p_3-1})}\right)^2} \tag{A.29}$$

- Result for energy threshold, corresponding to $y = 0.95$:

$$E_{\mathrm{thr}} = (800 \pm 10)\ \mathrm{MeV} \tag{A.30}$$

A.3. Photons

- Corresponding plot: Fig. 6.7(a)
- Function that has been fitted:

$$y(x) = \frac{1}{\left(1 \ + \ p_0 \ e^{p_1(x+p_2)}\right)^{1/p_3}} \tag{A.31}$$

- Fit results:

$$\begin{aligned} p_0 &= 16 \pm 6 \\ p_1 &= 0.0013 \pm 0.0003 \\ p_2 &= -3700 \pm 500 \\ p_3 &= 13 \pm 3 \end{aligned} \tag{A.32}$$

- Inverse function:

$$x(y) = \frac{1}{p_1} \ \ln\left(\frac{1}{p_0} \ \left(\frac{1}{y^{p_3}}\right)\right) - p_2 \tag{A.33}$$

- Function to determine uncertainty (using error propagation):

$$\delta x = \sqrt{\left(\frac{\delta p_0}{p_0 \ p_1}\right)^2 + \left(\frac{x+p_2}{p_1}\delta p_1\right)^2 + (\delta p_2)^2 + \left(\ln(x) \ \frac{\delta p_0}{p_1 \ (x^{p_3-1})}\right)^2} \tag{A.34}$$

- Result for energy threshold, corresponding to $y = 0.95$:

$$E_{\text{thr}} = (1600 \pm 200) \text{ MeV} \tag{A.35}$$

A.4. Electrons

- Corresponding plot: Fig. 6.7(b)
- Function that has been fitted:

$$y(x) = \frac{1}{\left(1 \ + \ p_0 \ e^{p_1(x+p_2)}\right)^{1/p_3}} \tag{A.36}$$

- Fit results:

$$\begin{aligned} p_0 &= 5 \pm 2 \\ p_1 &= 0.0016 \pm 0.0003 \\ p_2 &= -3500 \pm 400 \\ p_3 &= 14 \pm 4 \end{aligned} \tag{A.37}$$

- Inverse function:

$$x(y) = \frac{1}{p_1}\ \ln\left(\frac{1}{p_0}\ \left(\frac{1}{y^{p_3}}\right)\right) - p_2 \tag{A.38}$$

- Function to determine uncertainty (using error propagation):

$$\delta x = \sqrt{\left(\frac{\delta p_0}{p_0\ p_1}\right)^2 + \left(\frac{x+p_2}{p_1}\delta p_1\right)^2 + (\delta p_2)^2 + \left(\ln(x)\,\frac{\delta p_0}{p_1\,(x^{p_3-1})}\right)^2} \tag{A.39}$$

- Result for energy threshold, corresponding to $y = 0.95$:

$$E_{\text{thr}} = (2100 \pm 300)\ \text{MeV} \tag{A.40}$$

A.5. Protons

- Corresponding plot: Fig. 6.8(a)
- Function that has been fitted:

$$y(x) = \frac{1}{(1\ +\ p_0\ e^{p_1(x+p_2)})^{1/p_3}} \tag{A.41}$$

- Fit results:

$$\begin{aligned} p_0 &= 12 \pm 3 \\ p_1 &= 0.007 \pm 0.002 \\ p_2 &= -1400 \pm 200 \\ p_3 &= 25 \pm 7 \end{aligned} \tag{A.42}$$

- Inverse function:

$$x(y) = \frac{1}{p_1}\ \ln\left(\frac{1}{p_0}\ \left(\frac{1}{y^{p_3}}\right)\right) - p_2 \tag{A.43}$$

- Function to determine uncertainty (using error propagation):

$$\delta x = \sqrt{\left(\frac{\delta p_0}{p_0\ p_1}\right)^2 + \left(\frac{x+p_2}{p_1}\delta p_1\right)^2 + (\delta p_2)^2 + \left(\ln(x)\,\frac{\delta p_0}{p_1\,(x^{p_3-1})}\right)^2} \tag{A.44}$$

- Result for energy threshold, corresponding to $y = 0.95$:

$$E_{\text{thr}} = (820 \pm 50)\ \text{MeV} \tag{A.45}$$

A.6. Neutrons

- Corresponding plot: Fig. 6.8(b)
- Function that has been fitted:

$$y(x) = p_0 \; e^{p_1 \; x} \tag{A.46}$$

- Fit results:

$$\begin{aligned} p_0 &= 1.010 \pm 0.006 \\ p_1 &= -0.00030 \pm 0.00002 \end{aligned} \tag{A.47}$$

- Inverse function:

$$x(y) = \frac{1}{p_1} \; \ln\left(\frac{1}{p_0} \; y\right) \tag{A.48}$$

- Function to determine uncertainty (using error propagation):

$$\delta x = \sqrt{\left(\frac{\delta p_0}{p_0 \; p_1}\right)^2 + \left(\frac{x}{p_1}\delta p_1\right)^2} \tag{A.49}$$

- Result for energy threshold, corresponding to $y = 0.95$:

$$E_{\text{thr}} = (200 \pm 20) \text{ MeV} \tag{A.50}$$

A.7. Pions

- Corresponding plot: Fig. 6.8(c)
- Function that has been fitted:

$$y(x) = \frac{1}{\left(1 \; + \; p_0 \; e^{p_1(x+p_2)}\right)^{1/p_3}} \tag{A.51}$$

- Fit results:

$$\begin{aligned} p_0 &= 12 \pm 3 \\ p_1 &= 0.007 \pm 0.002 \\ p_2 &= -1400 \pm 200 \\ p_3 &= 25 \pm 7 \end{aligned} \tag{A.52}$$

- Inverse function:

$$x(y) = \frac{1}{p_1} \ln\left(\frac{1}{p_0} \left(\frac{1}{y^{p_3}}\right)\right) - p_2 \tag{A.53}$$

- Function to determine uncertainty (using error propagation):

$$\delta x = \sqrt{\left(\frac{\delta p_0}{p_0\ p_1}\right)^2 + \left(\frac{x + p_2}{p_1}\delta p_1\right)^2 + (\delta p_2)^2 + \left(\ln(x)\,\frac{\delta p_0}{p_1\,(x^{p_3-1})}\right)^2} \tag{A.54}$$

- Result for energy threshold, corresponding to $y = 0.95$:

$$E_{\text{thr}} = (860 \pm 80)\ \text{MeV} \tag{A.55}$$

B. Additional histograms for Chapter 7

B.1. Simulations with vertical muons

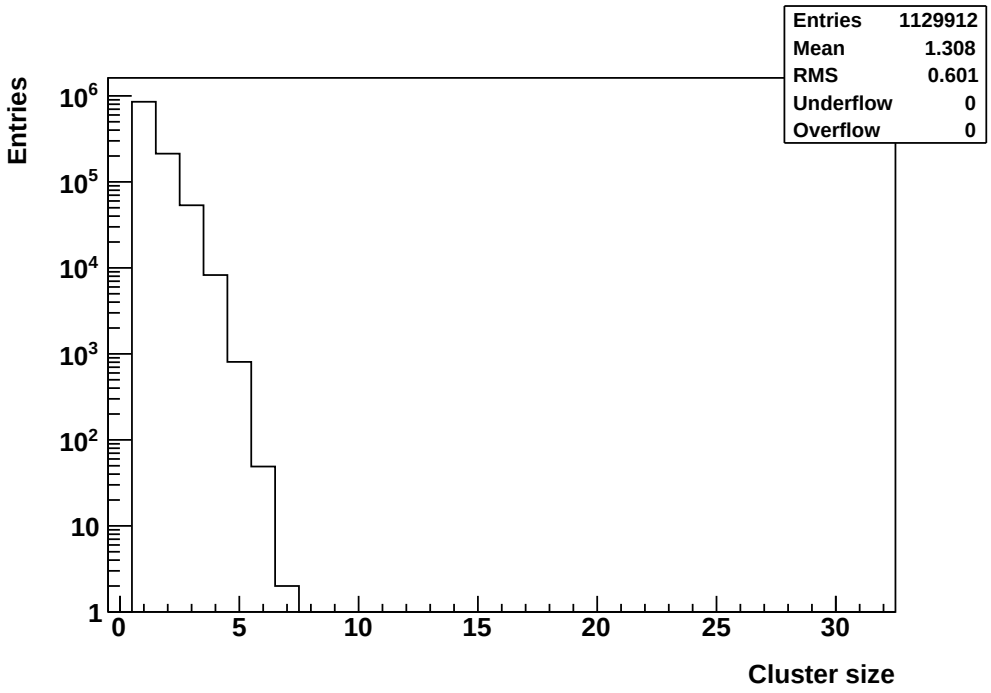

(a)

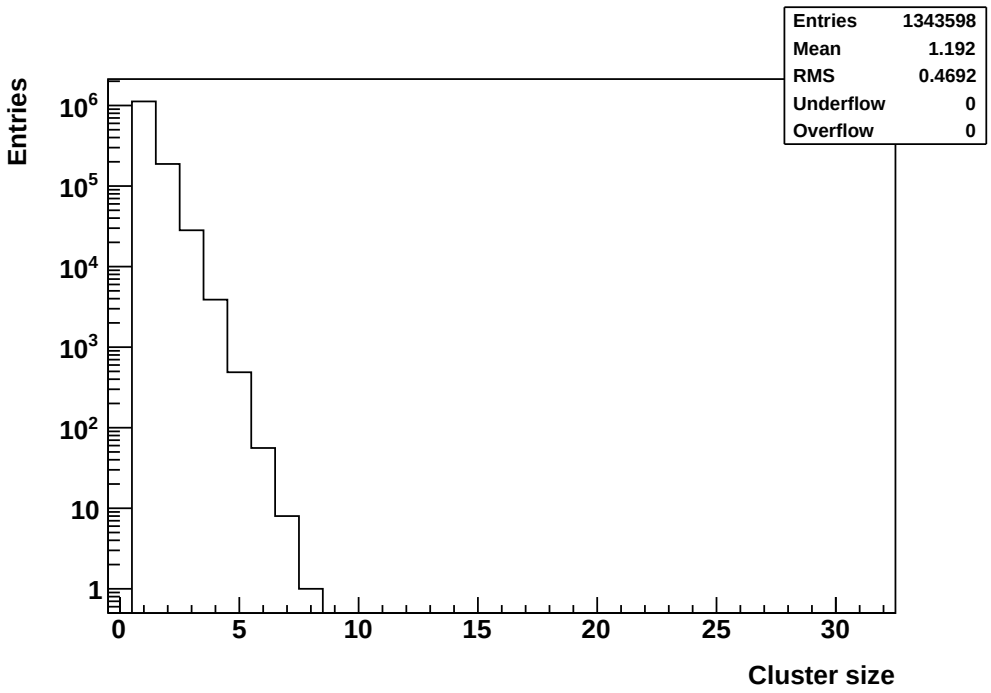

(b)

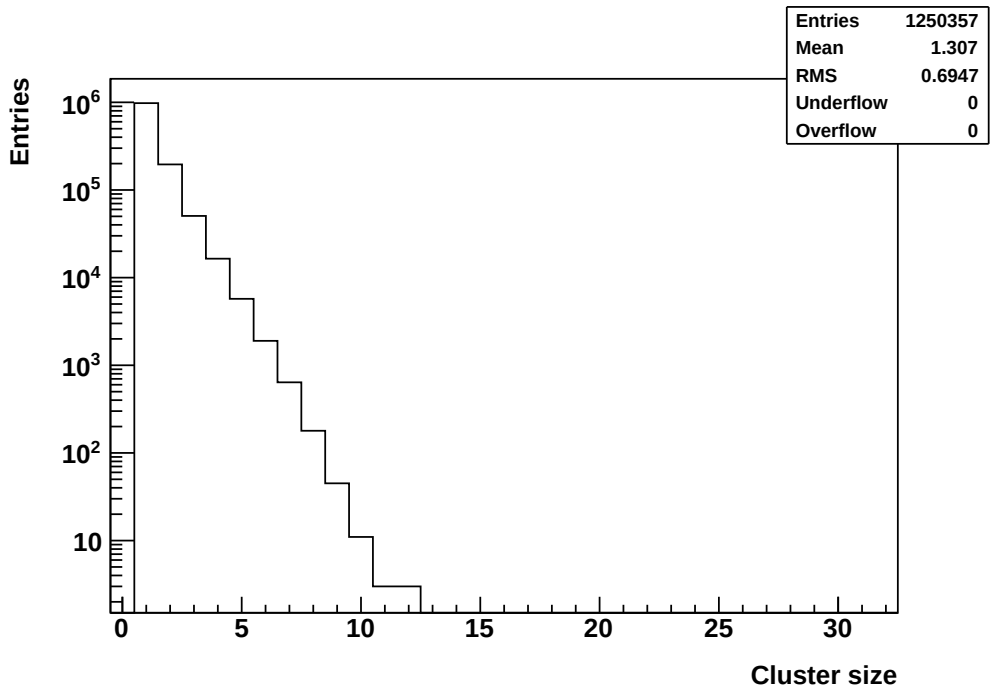
Entries 1250357
Mean 1.307
RMS 0.6947
Underflow 0
Overflow 0
Entries
Cluster size

(c)

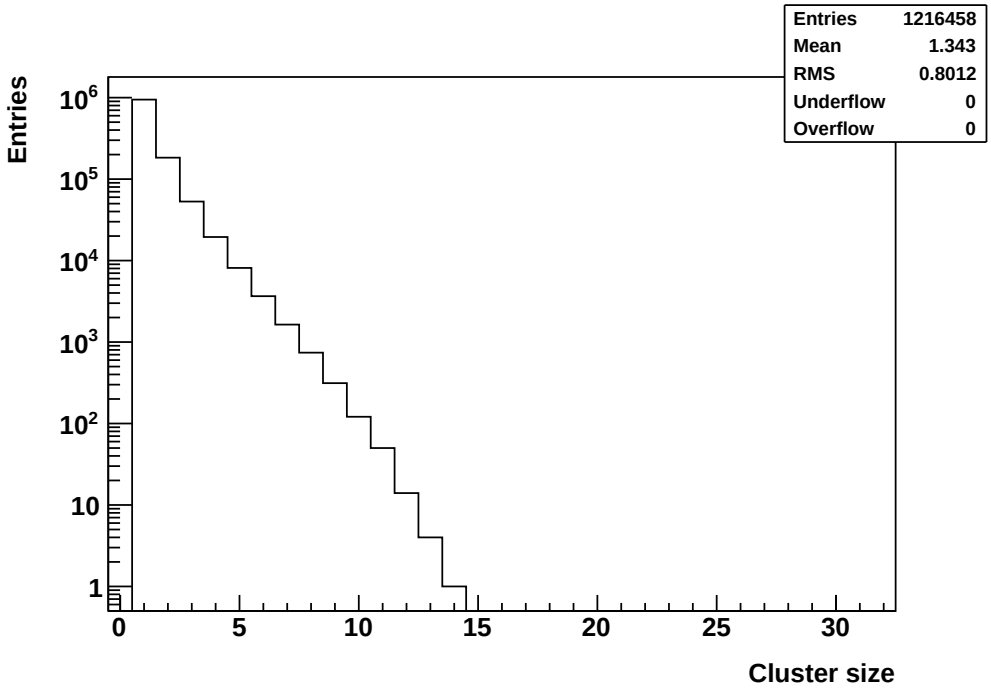
Entries 1216458
Mean 1.343
RMS 0.8012
Underflow 0
Overflow 0
Entries
Cluster size

(d)

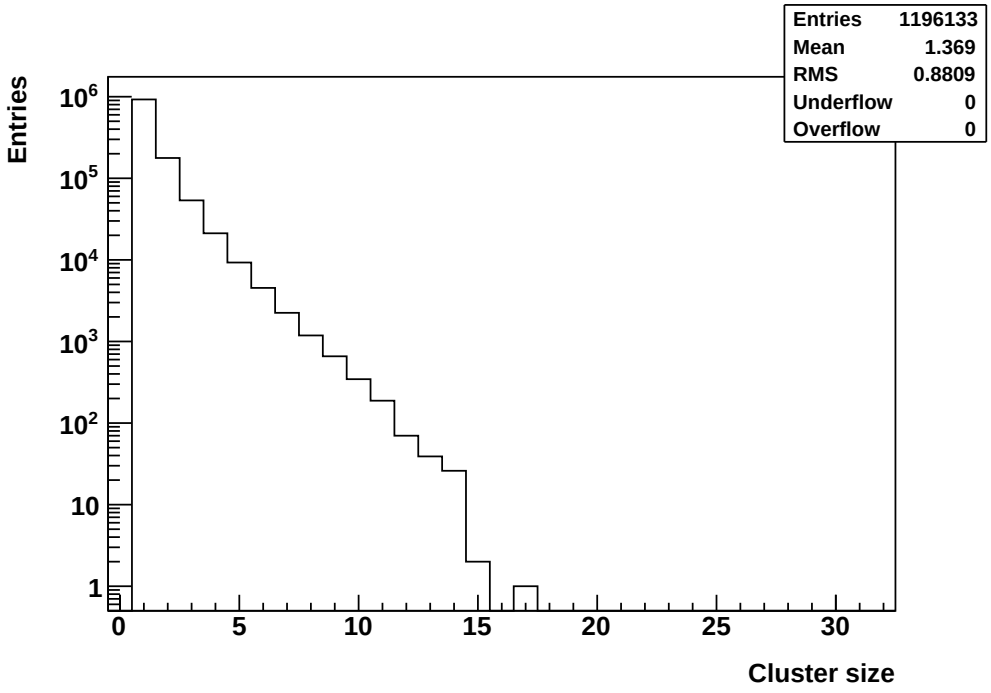
Entries 1196133
Mean 1.369
RMS 0.8809
Underflow 0
Overflow 0
Entries
10^6
10^5
10^4
10^3
10^2
10
1
0 5 10 15 20 25 30
Cluster size

(e)

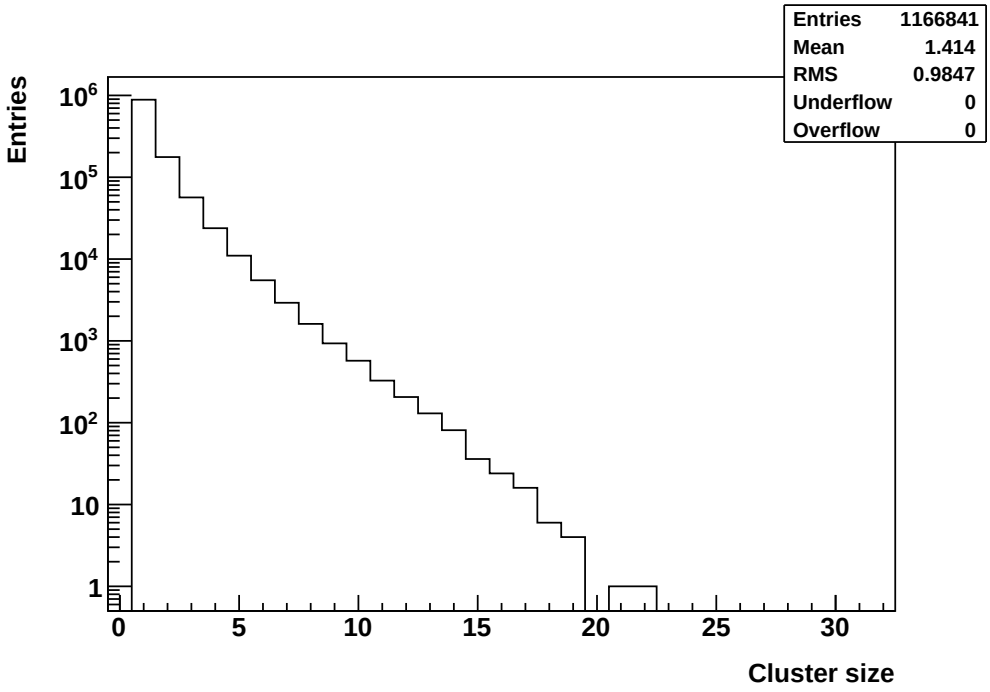
Entries 1166841
Mean 1.414
RMS 0.9847
Underflow 0
Overflow 0
Entries
10^6
10^5
10^4
10^3
10^2
10
1
0 5 10 15 20 25 30
Cluster size

(f)

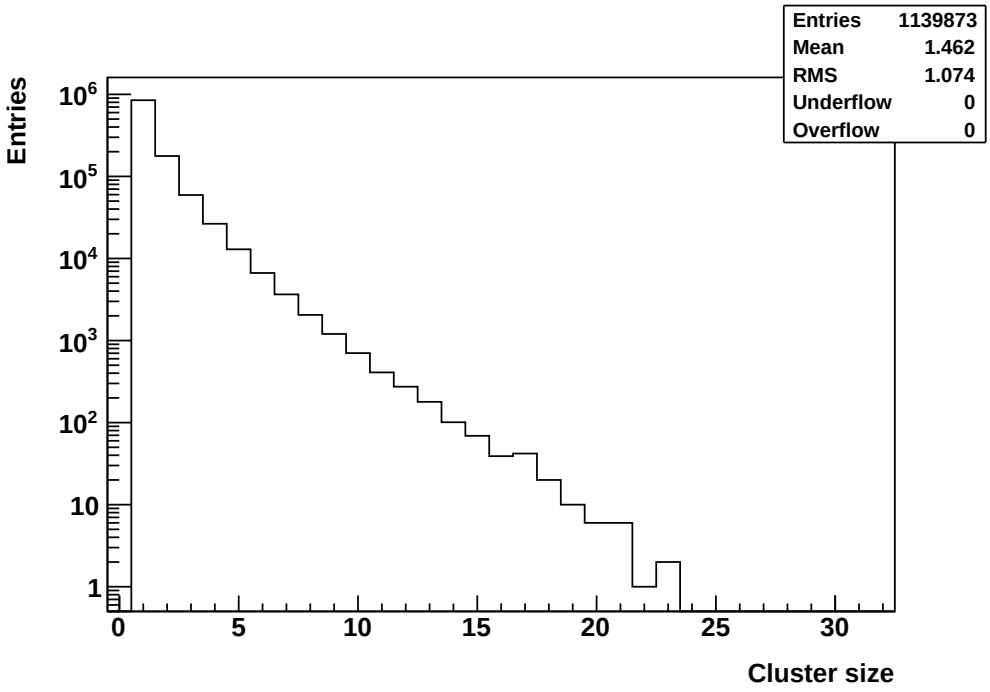

(g)

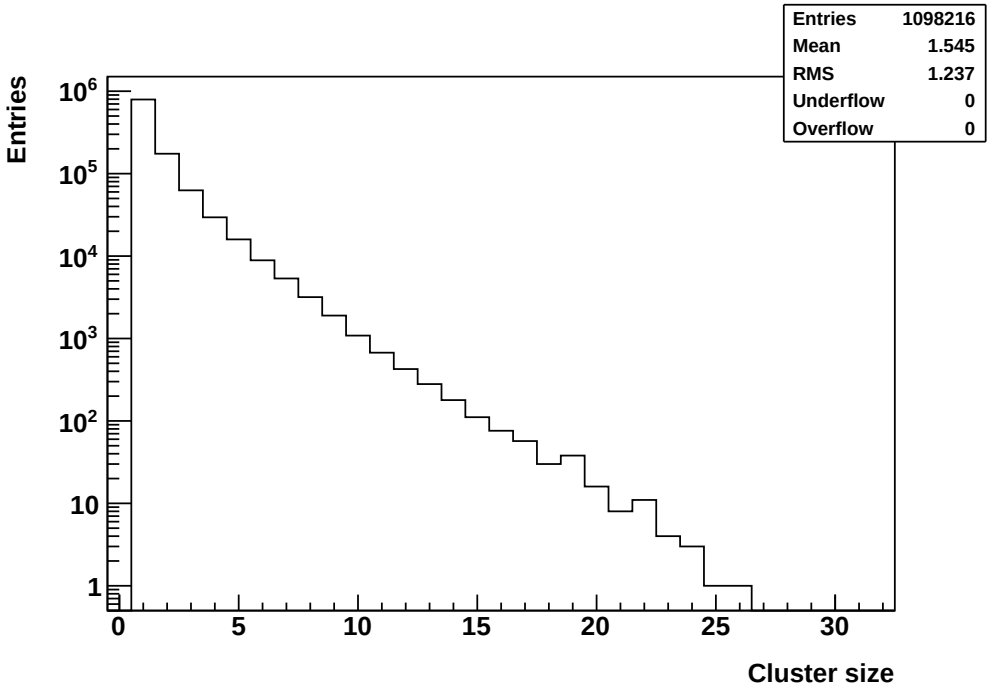

(h)

Figure B.1: Cluster sizes (excluding events with gaps between hits) for vertical muons with (a) 1 GeV, (b) 2 GeV, (c) 5 GeV, (d) 10 GeV, (e) 20 GeV, (f) 50 GeV, (g) 100 GeV and (h) 200 GeV kinetic energy; each histogram is based on the analysis of 1 500 000 events.

B.2. Simulations with inclined muons

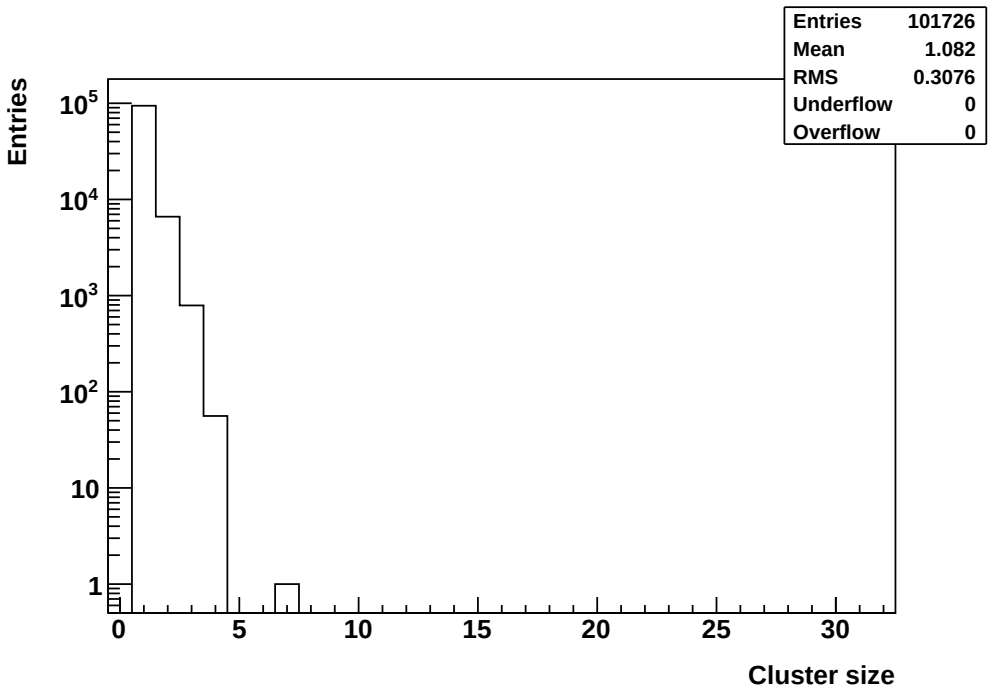

(a)

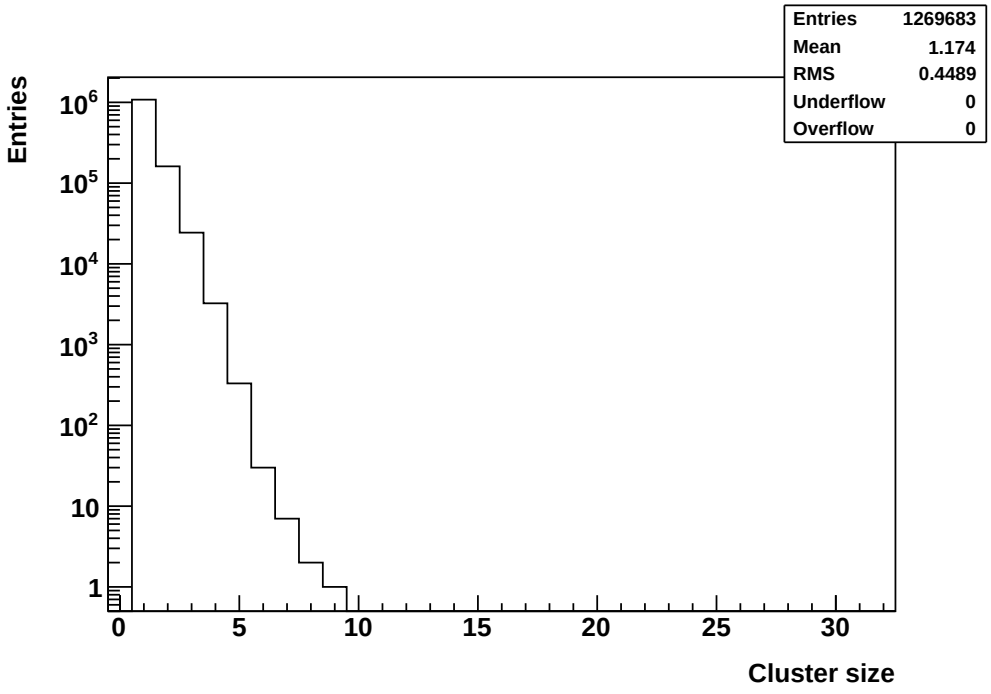

(b)

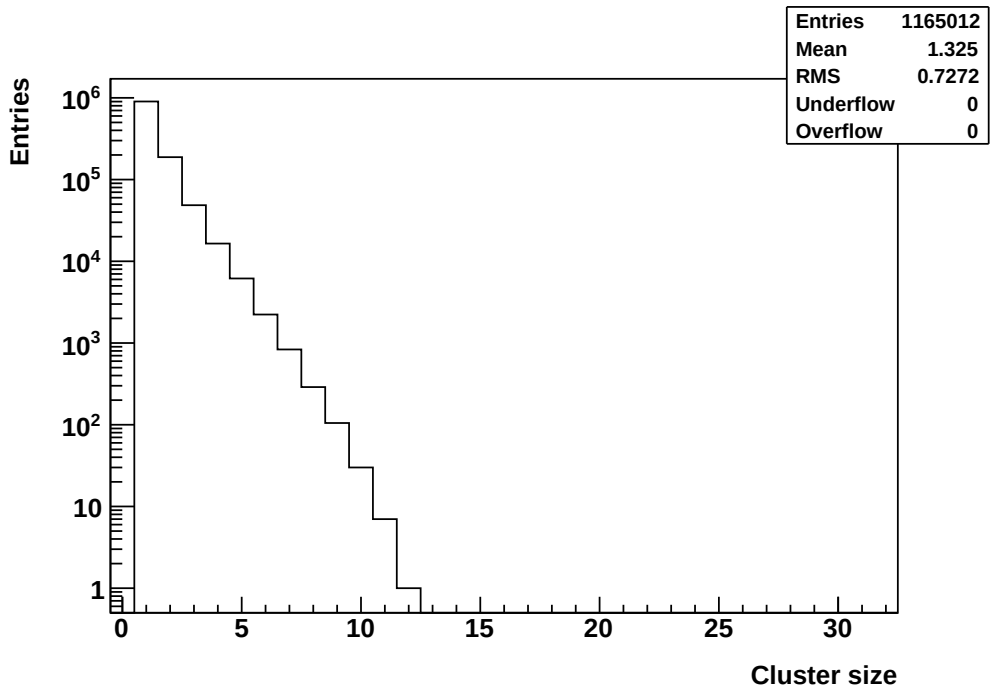
Entries 1165012
Mean 1.325
RMS 0.7272
Underflow 0
Overflow 0
Entries
Cluster size

(c)

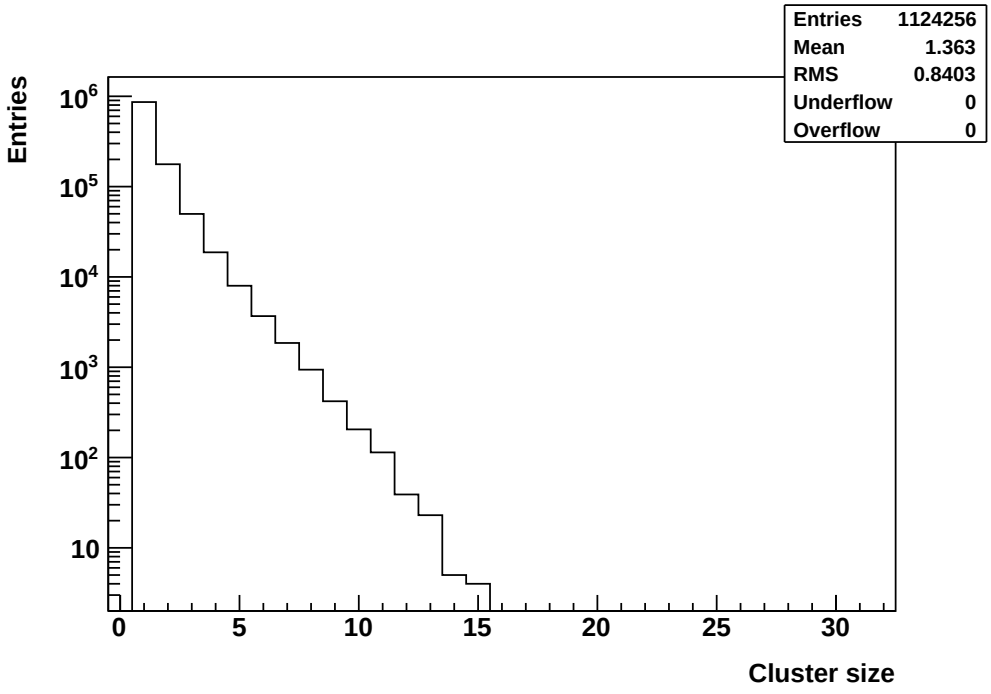
Entries 1124256
Mean 1.363
RMS 0.8403
Underflow 0
Overflow 0
Entries
Cluster size

(d)

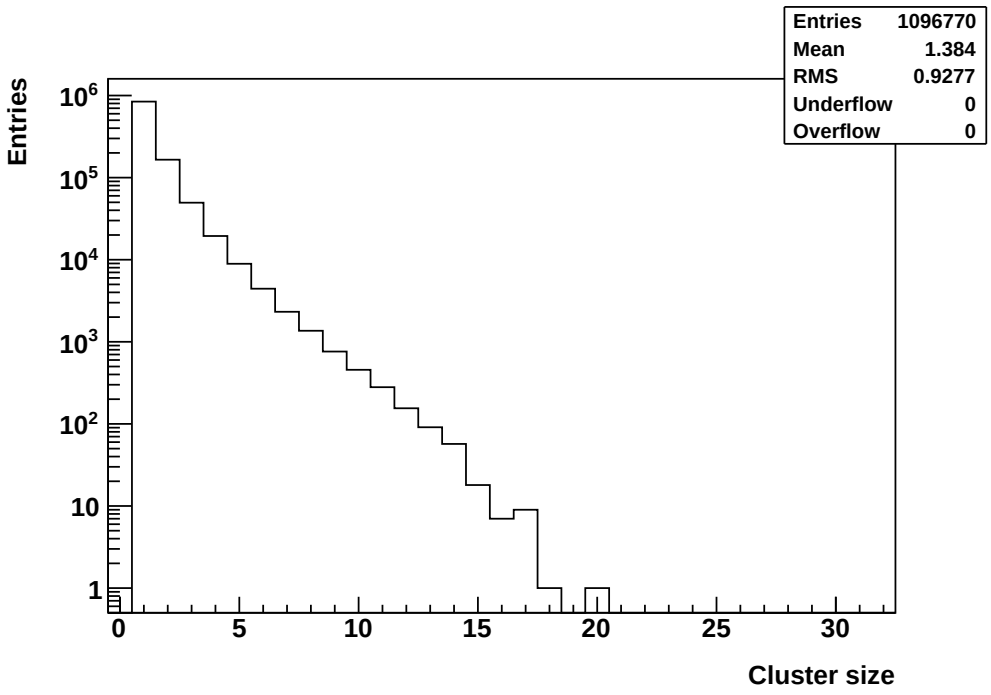
Entries 1096770
Mean 1.384
RMS 0.9277
Underflow 0
Overflow 0
Entries
Cluster size

(e)

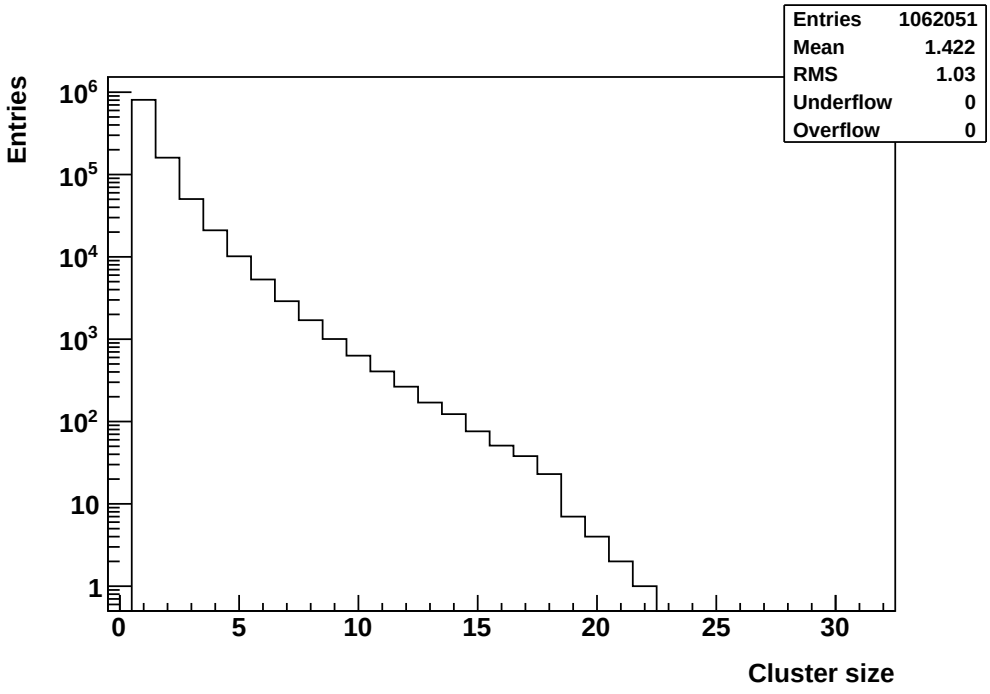
Entries 1062051
Mean 1.422
RMS 1.03
Underflow 0
Overflow 0
Entries
Cluster size

(f)

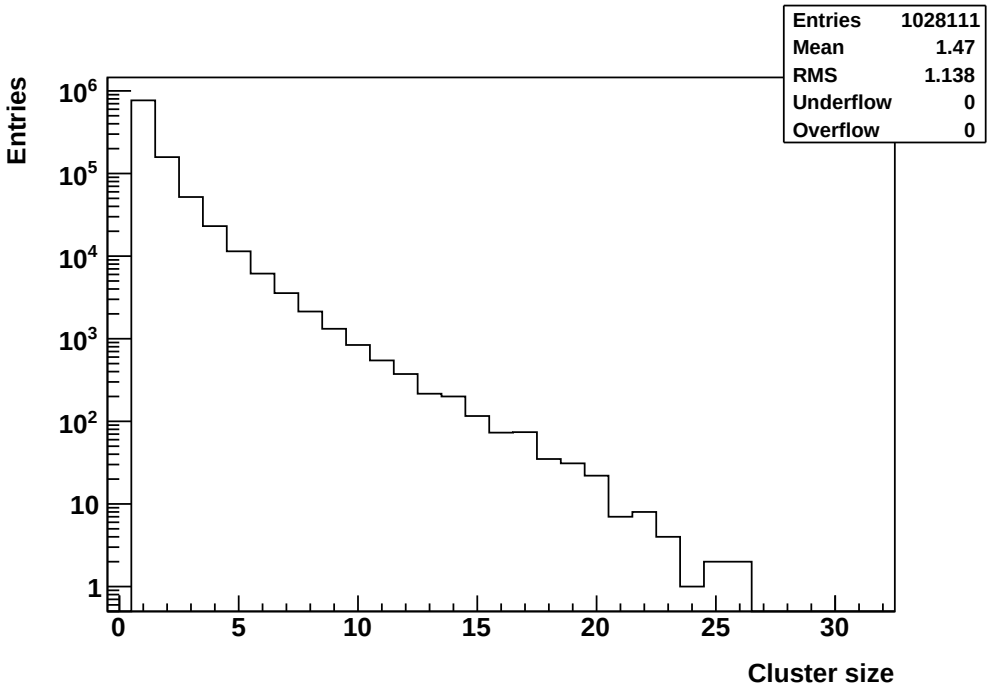

(g)

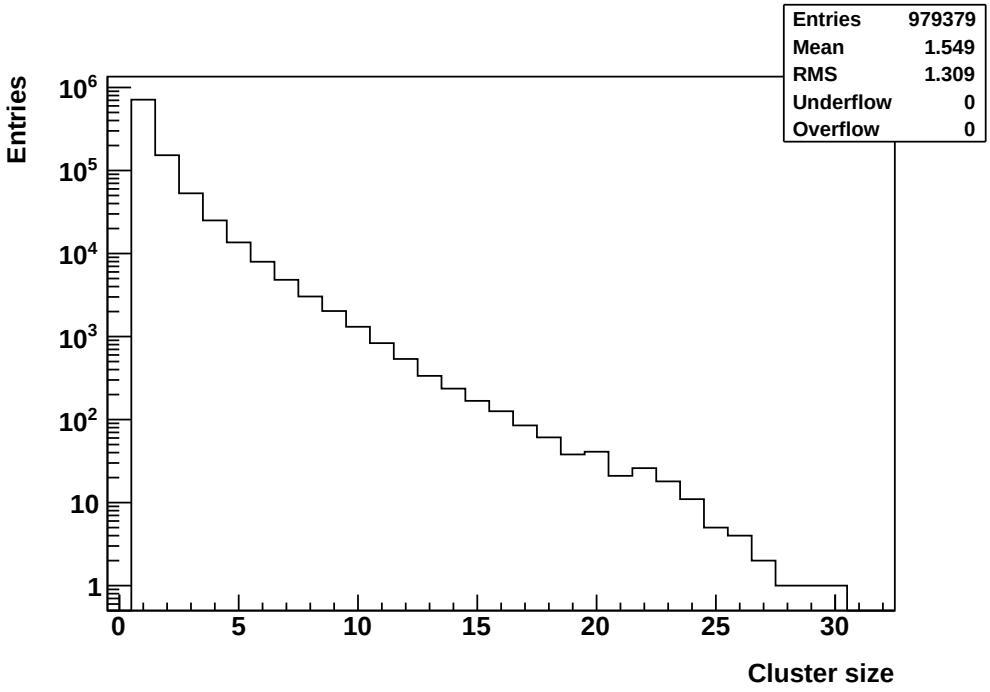

(h)

Figure B.2: Cluster sizes (excluding events with gaps between hits) for inclined (35°) muons with (a) 1 GeV, (b) 2 GeV, (c) 5 GeV, (d) 10 GeV, (e) 20 GeV, (f) 50 GeV, (g) 100 GeV and (h) 200 GeV kinetic energy; each histogram is based on the analysis of 1 500 000 events.

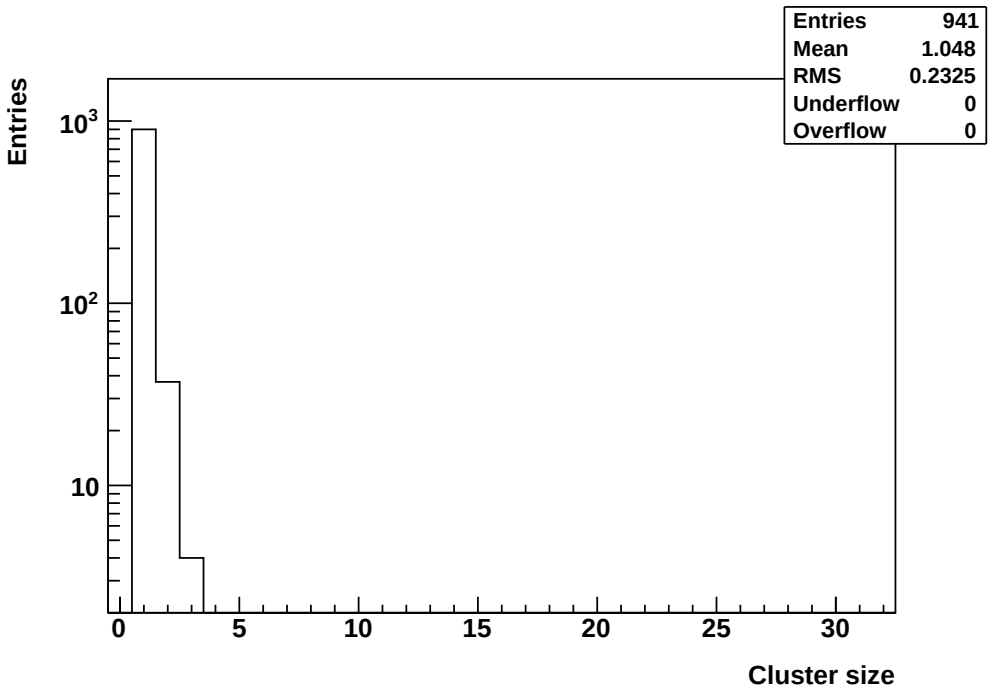
Entries 941
Mean 1.048
RMS 0.2325
Underflow 0
Overflow 0
Entries
10^3
10^2
10
0 5 10 15 20 25 30
Cluster size

(a)

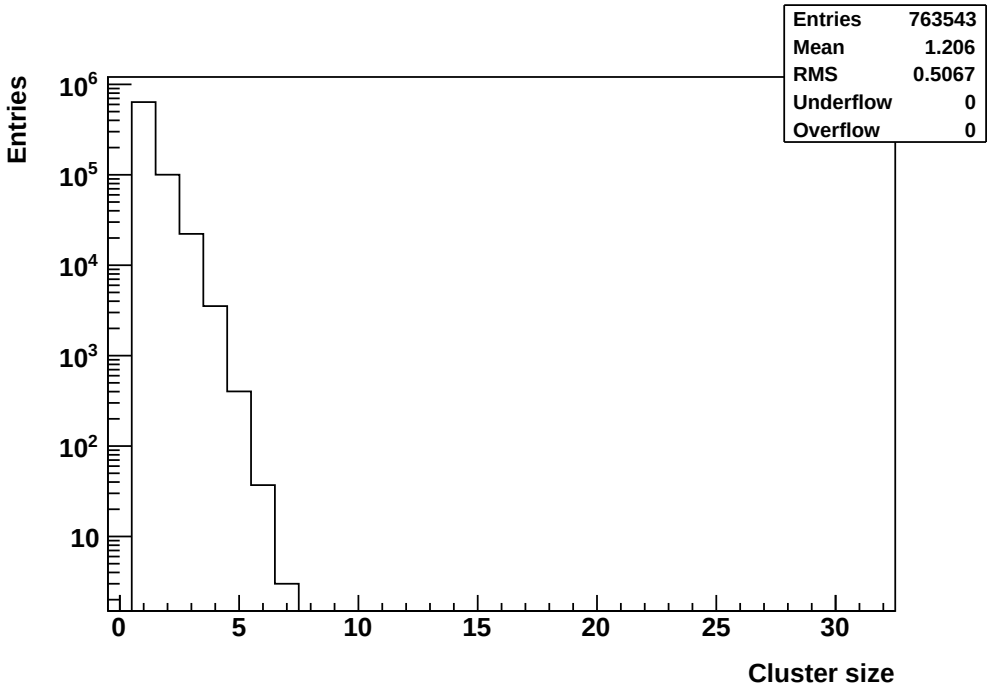
Entries 763543
Mean 1.206
RMS 0.5067
Underflow 0
Overflow 0
Entries
10^6
10^5
10^4
10^3
10^2
10
0 5 10 15 20 25 30
Cluster size

(b)

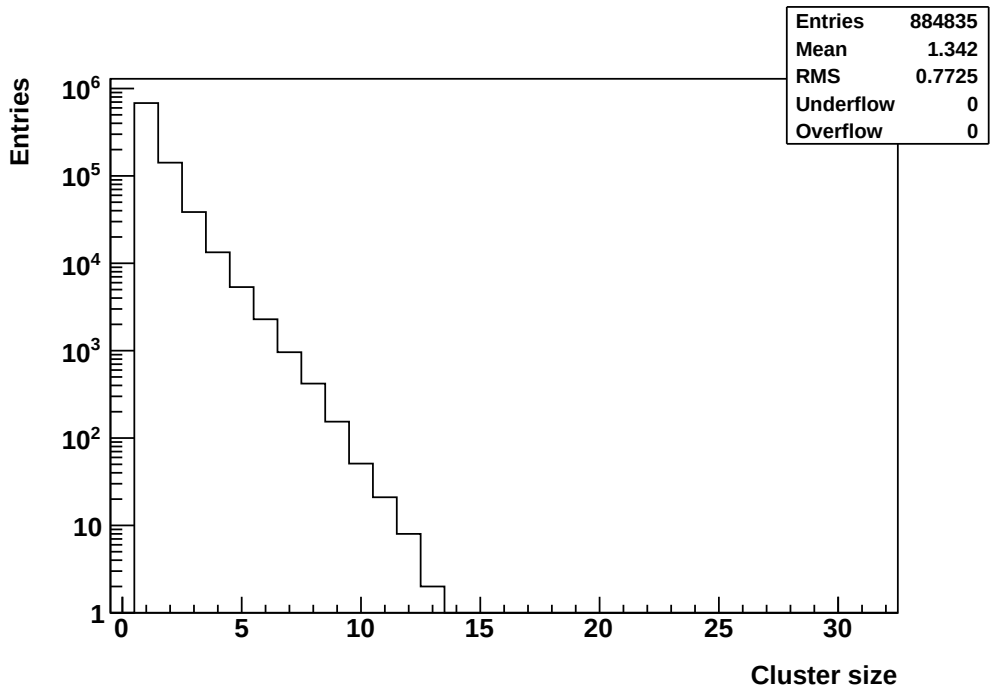
Entries 884835
Mean 1.342
RMS 0.7725
Underflow 0
Overflow 0
Entries
Cluster size

(c)

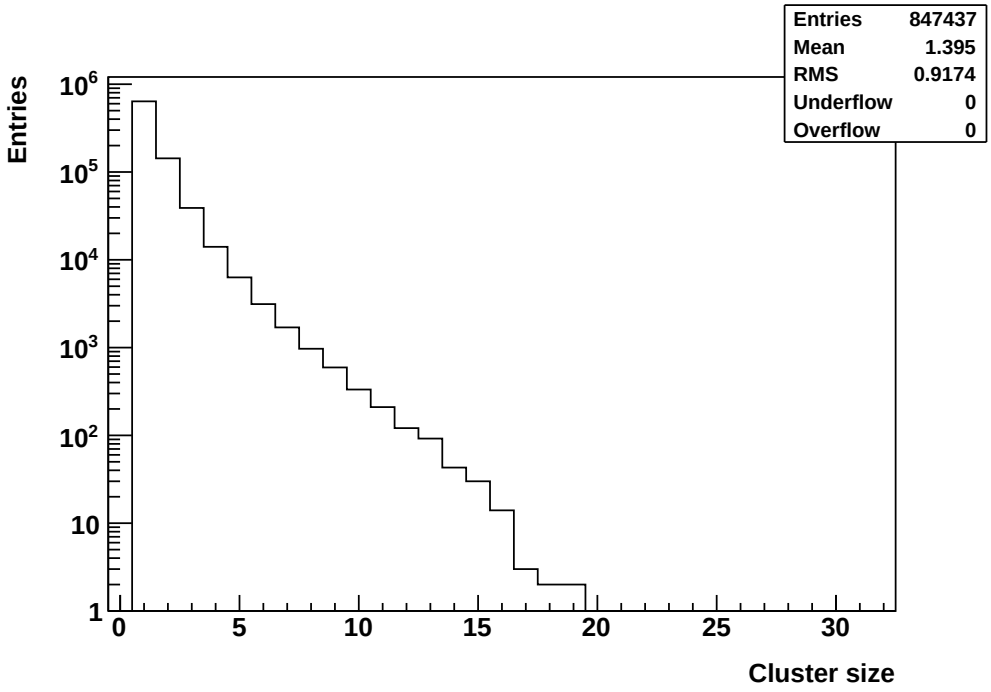
Entries 847437
Mean 1.395
RMS 0.9174
Underflow 0
Overflow 0
Entries
Cluster size

(d)

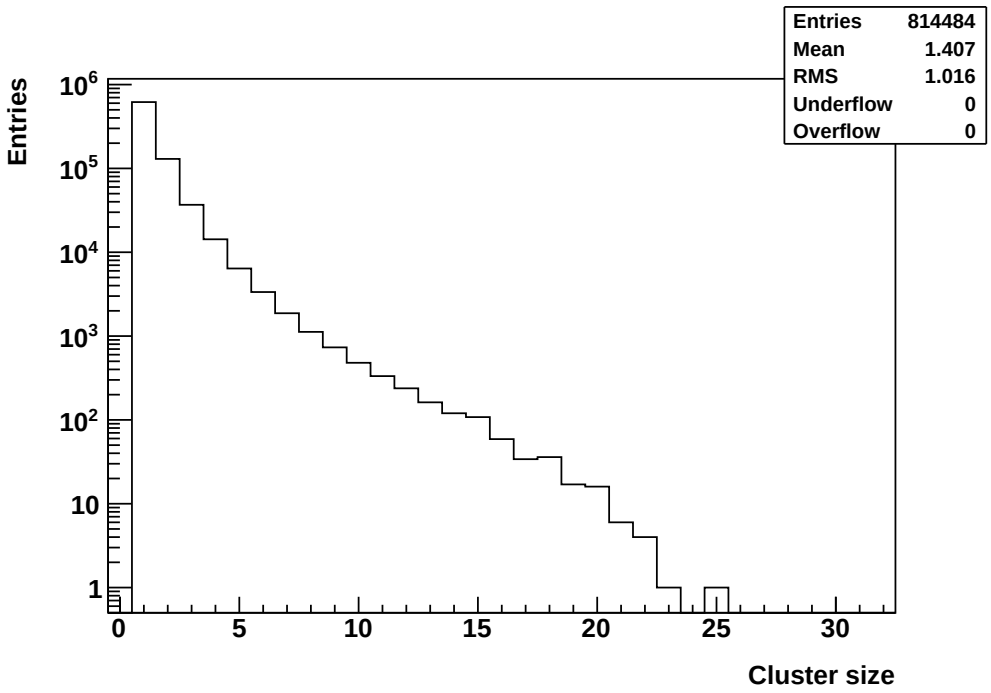
Entries 814484
Mean 1.407
RMS 1.016
Underflow 0
Overflow 0
Entries
Cluster size

(e)

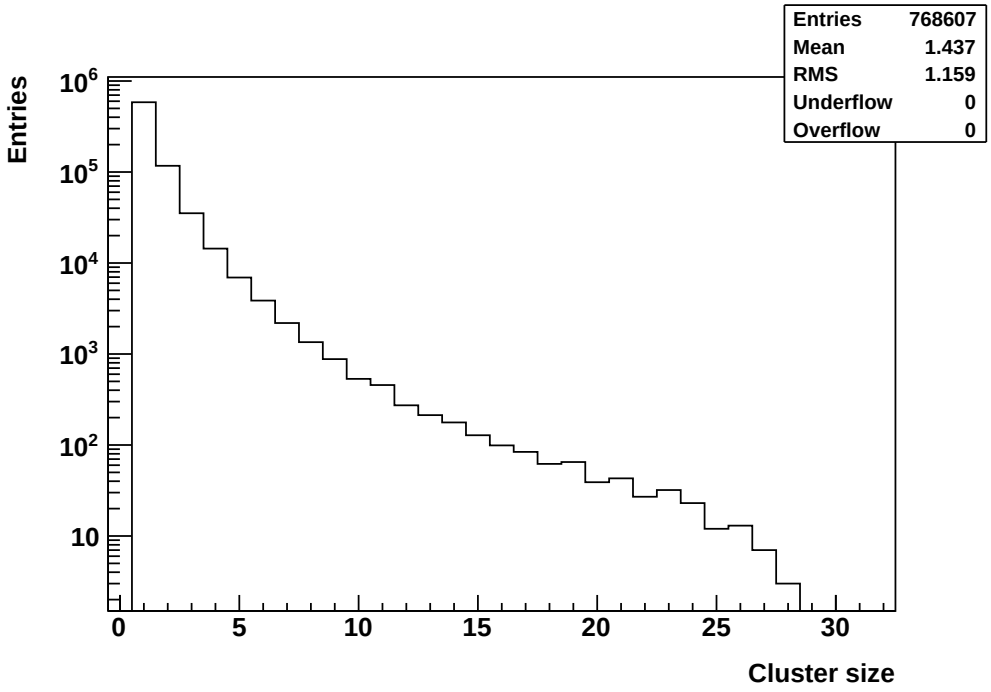
Entries 768607
Mean 1.437
RMS 1.159
Underflow 0
Overflow 0
Entries
Cluster size

(f)

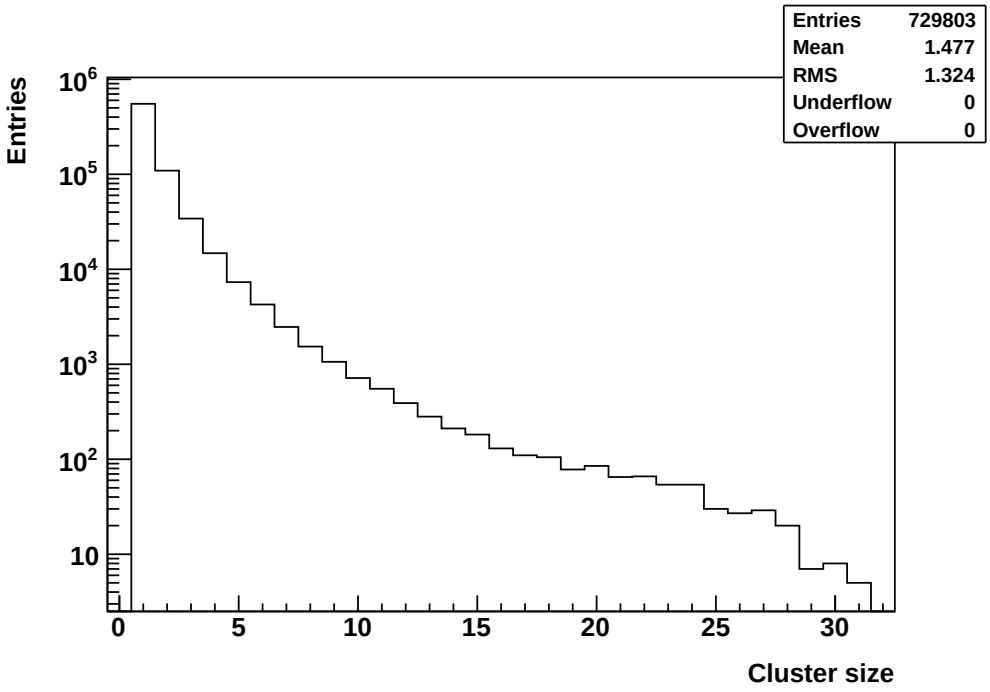

(g)

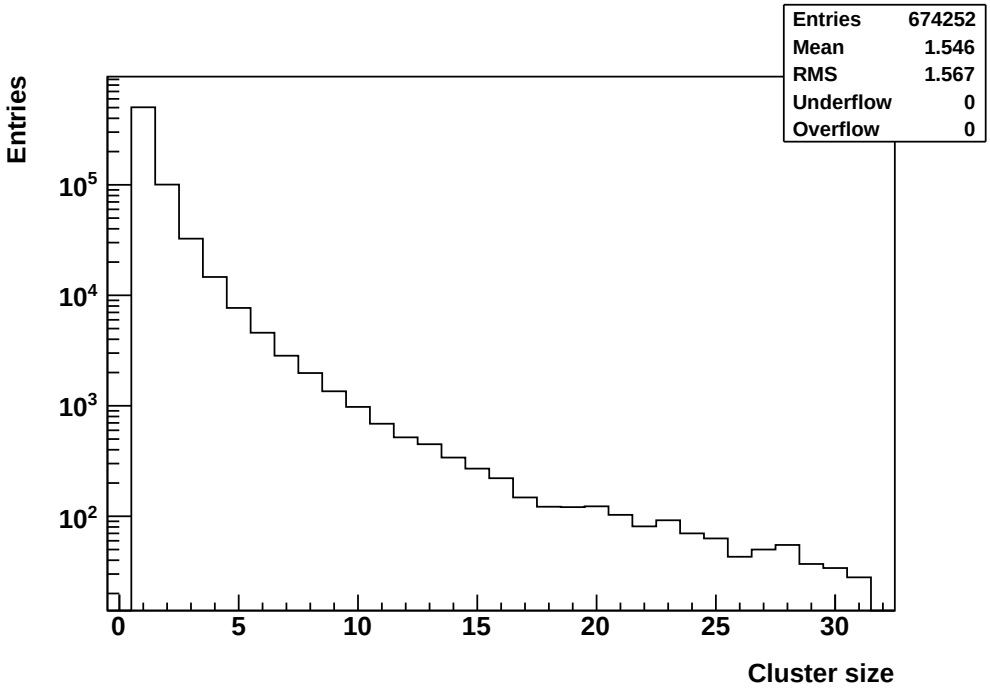

(h)

Figure B.3: Cluster sizes (excluding events with gaps between hits) for inclined (60°) muons with (a) 1 GeV, (b) 2 GeV, (c) 5 GeV, (d) 10 GeV, (e) 20 GeV, (f) 50 GeV, (g) 100 GeV and (h) 200 GeV kinetic energy; each histogram is based on the analysis of 1 500 000 events.

C. Bibliography

[1] The Pierre Auger Collaboration:
Pierre Auger Observatory website, `http://www.auger.org` (31.12.2010).

[2] J. P. Wefel:
The composition of the cosmic rays: an update, NATO ASIC Series 337 **337C** (1991), p. 29.

[3] D. Kickelbick:
The energy spectrum of primary cosmic rays measured with the KASCADE-Grande experiment, PhD thesis, University of Siegen, Germany, 2008.

[4] see e.g.: M. S. Longair:
High Energy Astrophysics, Volume 1: Particles, photons and their detection, Second Edition, Cambridge University Press, Cambridge, 1992.

[5] K. Nakamura et al. (Particle Data Group):
Review of Particle Physics, J. Phys. G **37** (2010), 075021.

[6] J. Blümer, R. Engel, J. R. Hörandel:
Cosmic rays from the knee to the highest energies, Progress in Particle and Nuclear Physics **63** (2009) p. 293-338.

[7] T. Antoni et al. (The KASCADE collaboration):
KASCADE measurements of energy spectra for elemental groups of cosmic rays: Results and open problems, Astropart. Phys. **24** (2005) p. 1-25.

[8] D. Kazanas, A. Nicolaidis:
Cosmic Ray "Knee": A Herald of New Physics?, International Cosmic Ray Conference, International Cosmic Ray Conference, vol. 5, 2001, pp. 1760-+.

[9] T. Abu-Zayyad et al. (The HiRes-MIA collaboration):
Measurement of the cosmic ray energy spectrum and composition from 10^{17} eV - $10^{18.3}$ eV *using a hybrid fluorescence technique*, Astrophys. J. **557** (2001) p. 686-699.

[10] M. Takeda et al. (The AGASA collaboration):
Energy determination in the Akeno Giant Air Shower Array experiment, Astropart. Phys. **19** (2003) p. 447-462.

[11] S. Swordy:
The energy spectra and anisotropies of cosmic rays, Space Science Reviews **99** (2001) p. 85-94.

[12] F. W. Stecker, M. H. Salamon:
Photodisintegration of Ultra-High-Energy Cosmic Rays: A New Determination, The Astrophysical Journal **512** (1999) p. 521-526.

[13] K. Greisen:
End to the cosmic ray spectrum?, Phys. Rev. Lett. **16** (1966) p. 748-750.

[14] G. T. Zatsepin, V. A. Kuzmin:
Upper limit of the spectrum of cosmic rays, JETP Lett. **4** (1966) p. 78-80.

[15] The HiRes collaboration:
Observation of the GZK cutoff by the HiRes experiment, Phys. Rev. Lett. **100** (2008), 101101.

[16] The Pierre Auger collaboration:
Measurement of the energy spectrum of cosmic rays above 10^{18} eV *using the Pierre Auger Observatory*, Phys. Lett. B **685** (2010), p. 239-246.

[17] R. M. Ulrich:
Measurement of the Proton-air Cross Section using Hybrid Data of the Pierre Auger Observatory, PhD thesis, University of Karlsruhe, Germany, 2008.

[18] see e.g.: C. Grupen:
Astroparticle Physics, Springer, Berlin, 2005.

[19] B. Keilhauer:
Investigation of Atmospheric Effects on the Development of Extensive Air Showers and their Detection with the Pierre Auger Observatory, PhD thesis, University of Karlsruhe, Germany, 2003.

[20] see e.g.: M. V. S. Rao, B. V. Sreekantan:
Extensive Air Showers, World Scientific Publishing, Singapore, 2005.

[21] K. Greisen:
The extensive air showers, Progess in Elementary Particle and Cosmic Ray Physics **3** (1956), p. 1-141.

[22] K. Kamata, J. Nishimura:
The lateral and the angular structure functions of electron showers, Prog. Theoret. Phys. Suppl. **6** (1958), p. 93-155.

[23] The Pierre Auger Collaboration:
Pierre Auger Observatory german website, `http://www.auger.de` (09.01.2011).

[24] The Pierre Auger Collaboration:
The Pierre Auger Observatory Design Report, Second Edition, `http://www.auger.org` (1997).

[25] The Pierre Auger Collaboration:
Correlation of the highest energy cosmic rays with nearby extragalactic objects, Science **318** (2007), p. 938-943.

[26] J. Blümer (The Pierre Auger Collaboration):
The northern site of the Pierre Auger Observatory, New J. Phys. **12** (2010), 035001.

[27] J. Abraham et al. (The Pierre Auger collaboration):
Trigger and aperture of the surface detector array of the Pierre AugerObservatory, Nucl. Instrum. Meth. A **613** (2010) p. 29-39.

[28] R. C. Shellard (The Pierre Auger Collaboration):
First results from the Pierre Auger Observatory, Braz. J. Phys. **36** (2006), p. 1184-1193.

[29] I. Allekotte et al. (The Pierre Auger Collaboration):
The Surface Detector System of the Pierre Auger Observatory, Nucl. Instrum. Meth. A **586** (2008), p. 409-420.

[30] P. A. Cherenkov:
Visible emission of clean liquids by action of γ radiation, Doklady Akademii Nauk SSSR **2** (1934), p. 451.

[31] The Pierre Auger collaboration:
The Fluorescence Detector of the Pierre Auger Observatory, Nucl. Instrum. Meth. A **620** (2010) p. 227-251.

[32] R. Mussa et al. (The Pierre Auger collaboration):
The LIDAR systems for atmospheric monitoring in Auger, Nucl. Instrum. Meth. A **518** (2004) p. 183-185.

[33] M. Kleifges (The Pierre Auger collaboration):
Extension of the Pierre Auger Observatory using high-elevation fluorescence telescopes (HEAT), Proceedings of the 31st International Cosmic Ray Conference, Łódź, Poland (2009).

[34] S. Fliescher (The Pierre Auger collaboration):
Radio detection of cosmic ray induced air showers at the Pierre Auger Observatory, Nucl. Instr. Meth. A (2010), doi:10.1016/j.nima.2010.11.045.

[35] The AMIGA collaboration:
AMIGA Design Report, Proposal for Evaluation by the Auger Assessment Committee (31.05.2006).

[36] G. Medina-Tanco (The Pierre Auger collaboration):
Astrophysics Motivation behind the Pierre Auger Southern Observatory Enhancements, Proceedings of the 30th International Cosmic Ray Conference, Merida, Mexico (2007).

[37] The KASCADE-Grande Collaboration, The LOPES Collaboration:
The KASCADE-Grande Experiment and the LOPES Project, Nucl. Phys. B **136** (2004) p. 384-389.

[38] A. D. Supanitsky et al.:
Underground Muon Counters as a Tool for Composition Analyses, Astropart. Phys. **29** (2008) p. 461-470.

[39] A. D. Supanitsky, G. Medina-Tanco, A. Etchegoyen:
On the possibility of primary identification of individual cosmic ray showers, Astropart. Phys. **31** (2009) p. 116-127.

[40] U. Fröhlich:
Charakterisierung der Szintillatoren und der Ausleseelektronik des AMIGA-Myonsystems, Masters thesis, University of Siegen, Germany, 2009.

[41] M. Platino (The Pierre Auger collaboration):
AMIGA - Auger Muons and Infill for the Ground Array of the Pierre Auger Observatory, Proceedings of the 31st International Cosmic Ray Conference, Łódź, Poland (2009).

[42] The MINOS collaboration:
The MINOS detectors technical design report, Fermilab Rep. NuMI-L-**337**, October 1998.

[43] M. Platino et al. (The Pierre Auger collaboration):
AMIGA at the Auger Observatory: The scintillator module testing system, preprint submitted to Nucl. Instr. and Meth. (2011).

[44] P. Buchholz (The Pierre Auger collaboration):
Hardware Developments for the AMIGA enhancement at the Pierre Auger Observatory, Proceedings of the 31st International Cosmic Ray Conference, Łódź, Poland (2009).

[45] U. Fröhlich:
Private communication, University of Siegen, Germany, February 2011.

[46] S. Agostinelli et al. (The Geant4 collaboration):
Geant4 - A Simulation Toolkit, Nucl. Instr. and Meth. A **506** (2003) p. 250-303.

[47] J. Allison et al. (The Geant4 collaboration):
Geant4 Developments and Applications, IEEE Trans. Nucl. Sci. **53** No. 1 (2006) p. 270-278.

[48] R. Tcaciuc:
Private communication, University of Siegen, Germany, February 2011.

[49] Hamamatsu Photonics K.K.:
Photomultiplier Tubes - Basics and Applications, third edition, 2006.

[50] D. Heck et al.:
CORSIKA: A Monte Carlo Code to Simulate Extensive Air Showers, Forschungszentrum Karlsruhe Report FZKA **6019** (1998).

[51] C. Canet et al.:
The site of the BATATA detector in Malargüe, Argentina: geological characterization, GAP note 2008-159, internal document of the Pierre Auger collaboration, not for public release.

[52] The Geant4 collaboration:
User's Guide: For Application Developers, Version 9.3, `http://geant4.cern.ch` (10.02.2011).

[53] The Geant4 collaboration:
Software Reference Manual, Version 9.3, `http://geant4.cern.ch` (10.02.2011).

[54] The Geant4 collaboration:
Physics Reference Manual, Version 9.3, `http://geant4.cern.ch` (10.02.2011).

[55] R. Brun, F. Rademakers:
ROOT - An Object Oriented Data Analysis Framework, Nucl. Instr. Meth. A **389** (1997) p. 81-86.

[56] F. James, M. Roos:
Minuit: A System for Function Minimization and Analysis of the Parameter Errors and Correlations, Comput. Phys. Commun. **10** (1975) p. 343-367.

[57] F. Sánchez:
Private communication, Instituto de Tecnologías en Detección y Astropartículas (ITeDA), Buenos Aires, Argentina, February 2011.

[58] H. A. Bethe:
Zur Theorie des Durchgangs schneller Korpuskularstrahlen durch Materie, Ann. d. Phys. **5** (1930) p. 325-400.

[59] see e.g.: C. Grupen, B. Shwartz:
Particle Detectors (Second Edition), Cambridge University Press, Cambridge, 2008.

[60] M. Settimo:
Private communication, University of Siegen, Germany, March 2011.

[61] T. Hebbeker, C. Timmermans:
A compilation of high energy atmospheric muon data at sea level, Astropart. Phys. **18** (2002) p. 107-127.

[62] M. Boezio et al. (The CAPRICE Collaboration):
Measurement of the flux of atmospheric muons with the CAPRICE94 apparatus, Phys. Rev. D **62** (2000) 032007.

[63] N.D. Gagunashvili:
Comparison of weighted and unweighted histograms, PoS (ACAT) **54** (2007).

D. List of Figures

E. List of Tables

F. List of Acronyms

AERA	Auger Engineering Radio Array
AGASA	Akeno Giant Air Shower Array
AGN	Active Galactic Nucleus
AMIGA	Auger Muons and Infill for the Ground Array
CAPRICE94	Cosmic Antiparticle Ring Imaging Cherenkov Experiment 1994
CDAS	Central Data Acquisition System
CMB	Cosmic Microwave Background
CNO	Carbon, Nitrogen, Oxygen
CORSIKA	Cosmic Ray Simulations for KASCADE
FADC	Flash Analog-to-Digital Converter
FD	Fluorescence detector
FPGA	Field-Programmable Gate Array
Geant4	Geometry and Tracking 4
GPS	Global Positioning System
GZK	Greisen, Zatsepin, Kusmin
HEAT	High Elevation Auger Telescopes
HiRes	High Resolution Fly's Eye
KASCADE-Grande	Karlsruhe Shower Core and Array Detector Grande
LIDAR	Light Detection and Ranging
MINOS	Main Injector Neutrino Oscillation Search
NDF	Number of Degrees of Freedom
NKG	Nishimura, Kamata, Greisen
PCB	Printed Circuit Board
PDG	Particle Data Group
PMT	Photomultiplier Tube
RAM	Random-Access Memory
SD	Surface Detector
ToT	Time-over-Threshold

UHECR	Ultra-High-Energy Cosmic Ray
UV	Ultraviolet
VEM	Vertical Equivalent Muon

Danksagung

Abschließend möchte ich die Gelegenheit nutzen und all denjenigen danken, die zum Gelingen dieser Masterarbeit, die den Schlusspunkt von fünf Jahren Studium darstellt, beigetragen haben.

Mein besonderer Dank gilt dabei:

- Prof. Dr. Peter Buchholz für die Betreuung dieser Arbeit, durch die ich in das faszinierende Gebiet der Astroteilchenphysik einsteigen konnte.

- Prof. Dr. Markus Risse nicht nur für die Bereitschaft, diese Arbeit als Zweitgutachter zu bewerten, sondern auch dafür, dass er mir die Gelegenheit gibt, weiter ein Teil der Pierre-Auger-Kollaboration zu bleiben.

- Dr. Thomas Bäcker, Uwe Fröhlich und Rebecca Klein für die viele Zeit, die sie beim Korrekturlesen dieser Arbeit dafür geopfert haben, meine Gedanken in eine lesbare Form zu bringen.

- Der gesamten Arbeitsgruppe Experimentelle Teilchenphysik an der Universität Siegen für die angenehme Arbeitsatmosphäre und dafür, dass jeder einzelne bei Fragen und Problemen immer mit Rat und Tat bereitstand. Insbesondere danke ich Dr. Thomas Bäcker, Uwe Fröhlich, Michael Pontz, Dr. Mariangela Settimo, Dr. Rodica Tcaciuc und Martin Tigges für die fruchtbaren, oftmals auch nicht ganz ernsthaften, Diskussionen.

- Meinem Büronachbarn Bakul Gaur, von dessen schier unendlichen Programmierkenntnissen ich mehr als einmal profitieren konnte und von dem ich so manches über die indische Kultur erfahren durfte.

- Meinen Kommilitonen Stefan Gadatsch und Martin Tigges, mit denen ich vor nunmehr fünf Jahren mein Studium in Siegen begann und die mir eine unvergessliche Zeit bescherten.

Der größte Dank gebührt jedoch meinen Eltern und meiner gesamten Familie, die mich, nicht nur während meines Studiums, in jeder Hinsicht unterstützt haben und mir so den Rückhalt gaben, ohne den das alles gar nicht möglich gewesen wäre.

Danke!

Eidesstattliche Erklärung

Hiermit erkläre ich, dass ich die vorliegende Masterarbeit selbständig verfasst und keine anderen als die angegebenen Quellen und Hilfsmittel benutzt, sowie Zitate und Ergebnisse Anderer kenntlich gemacht habe.

....

(Ort) (Datum) (Unterschrift)